A Modified FDTD Method for the Analysis of Wide and Dual Band Antennas

Michael Wong

A Thesis

in

The Department

of

Electrical and Computer Engineering

Presented in Partial Fulfillment of the Requirements
for the Degree of Master of Applied Science (Electrical Engineering) at
Concordia University
Montreal, Quebec, Canada

March 2006

Your file Votre référence
ISBN: 0-494-14285-5
Our file Notre référence
ISBN: 0-494-14285-5

ABSTRACT

A Modified FDTD Method for the Analysis of Wide and Dual Band Antennas

Michael Wong

This thesis uses a modified Finite-Difference Time-Domain (FDTD) method to examine several wide and dual band antenna structures. The FDTD method is a finite difference approximation to Maxwell's equation that is solved in the time domain. Frequency domain results are obtained by taking the Fourier transform of the time-domain result. Recent advances in the FDTD method such as the Convolutional Perfectly Matched Layer (CPML) were necessary for such analysis of certain structures and have been used for simulation in this thesis. Some improvements in the implementation of the boundary conditions and in the CPML implementation have been documented and the new Floating Perfectly Matched Layer (Floating PML) has been introduced. The historical and mathematical development of the FDTD method is also discussed.

The code itself is written in object-oriented C++ and has been partially optimized for speed. It has been written so that microstrip and stripline structures are particularly easy to implement. Because the code fully implements Maxwell's equations, the radiation characteristics of antennas are correctly modeled when designing microstrip structures. The code has been verified with simple to more complicated antenna structures such as microstrip-fed dielectric resonator antennas (DRA).

DRA structures have been simulated with varying dielectric constant, such as the hybrid resonator antenna using a dielectric disc with a permittivity of 35.5. In this example, the results from the software match commercial software very closely.

In addition, a stripline structure with dual slots is introduced with the goal of creating a dual band, symmetrical omni-directional antenna. The investigation is done via numerical simulation using the FDTD method as described above. The results compared well with those based on commercial software. One dual-band configuration provided a reasonable 10 dB bandwidth of 25% at 5.8 GHz and 10% at 2.45 GHz. The effect of different design parameters on the resonant frequencies and bandwidth is then discussed. This parametric study is presented in the form of graphs showing the effects of varying slot length and slot width.

Other designs are studied within this thesis and then suggestions for future work are presented in the conclusions.

Table of Contents

List of Symbols

Δx	grid spacing in the x-direction
Δy	grid spacing in the y-direction
Δz	grid spacing in the z-direction
Ω_A	Solid Angle
$\psi_{E\,w,v}$	Variable needed for E field storage in CPML boundary. w, v are x, y, or z
$\psi_{H\,w,v}$	Variable needed for H field storage in CPML boundary. w, v are x, y, or z
ψ	Angle between two vectors used in far field derivation
κ	constant in CPML definition
ζ	Variable used for derivation of CPML
σ	Electric conductivity
σ^*	Magnetic conductivity
μ	permeability of medium
ε	permittivity of medium
λ	Wavelength
Γ	Reflection Coefficient
β	propagation constant
ω	Radian Frequency
b_w, c_w	Constants for CPML, where w is x, y, or z
c	speed of light in a vacuum
C_a, C_b	Constants for FDTD for electric field component
Da, Db	Constants for FDTD for magnetic field component

D_o	Maximum Directivity
E	Electric field
Ex, Ey, Ez	Components of the electric field, **E**
H	Magnetic field
Hx, Hy, Hz	Components of the magnetic field, **M**
J	Electric field current
k	propagation constant
M	Magnetic field current
$\hat{\mathbf{n}}$	Unit vector normal to a surface
N, L	vector potentials used in derivation of far field
s	CFS coefficient
S	numerical stability factor, or Courant number

List of Abbreviations

ABC	Absorbing Boundary Condition
ADI	Alternating Direction Implicit
CFS	Complex Frequency-Shifted
CPML	Convolutional Perfectly Matched Layer
DRA	Dielectric Resonator Antenna
EMP	Electromagnetic Pulse
FEM	Finite Element Method
FM	Frequency Modulation
FDTD	Finite Difference Time Domain
FDTD-FE	Finite Difference Time Domain Finite Element
FDTD-FV	Finite Difference Time Domain Finite Volume
GPU	Graphics Processing Unit
ISM	Industrial, Scientific, Medical
LAN	Local Area Network
MoM	Method of Moments
NA	Neighborhood Averaging
PEC	Perfect Electric Conductor
PML	Perfectly Matched Layer
UPML	Uniaxial Perfectly Matched Layer

Chapter 1: Introduction

Electromagnetics exists all around us. The general principles applied to electromagnetic theories can be applied from light to microwaves [1]. Some applications include very low frequency around-the-world propagation down to 3 Hz, or photonic devices such as the cross-waveguide switch [1]. The unification of these electromagnetic principles that allow for their description is known as Maxwell's Equations [2], named after James Clerk Maxwell, a Scottish physicist and mathematician.

In many everyday electromagnetic problems, exact analytical solutions are often difficult to find. One such problem is to find the radiation pattern from a complete cellular telephone when placed close to a human head, for example. Even simpler problems such as the radiation from a microstrip antenna are most easily analyzed with numerical methods once shaped slots or other abnormalities are introduced into the patch.

One of the more recent and common uses for such methods of analyzing radiation is the Finite-Difference Time-Domain (FDTD) Method. The FDTD Method has become very popular because of its very simple formulation and the resulting simplicity in its implementation. In this thesis, the FDTD Method is used to analyze wide and dual band antennas and other related structures.

1.1 Applications and Motivations

Every wireless electronic device in modern life today makes use of basic electrical principles that can be analyzed with Maxwell's equations. A cellular telephone,

for example, must have an antenna which radiates into free space. Wireless internet, FM radio, even satellite TV, all use some component that can be analyzed numerically with the FDTD method.

The modern day thirst for new gadgets often results in a need for faster data transfer rates, which, in turn, results in a need for wider bandwidth. Because bandwidth is a very scare resource, many newer designs require new frequency bands, as well as wider bandwidth. These requirements for wider bandwidths and new frequency bands require the development of wide and dual band antennas.

FDTD has been used for many different applications, such as antenna analysis, microstrip structures, or more recently, biological simulations. In the biological simulation, the reaction of human tissue to electromagnetic radiation is analyzed with the FDTD method.

1.2 Objectives

The main objective of this thesis is to analyze dual and wideband antenna structures using the FDTD method, and to advance the knowledge in this area. The FDTD method used for this purpose uses the CPML absorbing boundary condition (ABC), where the implementation of this ABC has been optimized for the solution of microstrip and stripline antenna problems.

1.3 Overview of Thesis

In Chapter 2, a review of the history of the FDTD method is given, followed by some key topics that must be considered when using the FDTD method. Several dual and broadband antenna designs relevant to this thesis are then discussed.

Chapter 3 discusses the methods unique to this thesis that have been used to implement the FDTD software, and discusses the software validation process.

Chapter 4 discusses numerical results for dual and broadband antenna structures and introduces a new dual band dual slot stripline omni-directional antenna.

Chapter 5 concludes with a summary and suggestions for future work.

Chapter 2: Literature Review

2.1 Introduction

This chapter gives an overview of the state of the art on FDTD. The FDTD method is in continual evolution and so only a few topics in this area have been chosen, including dispersion / anisotropy, stability, the PML, conformal FDTD, and hardware acceleration.

This chapter then discusses a few designs to reveal some background about the current state of wideband antenna design.

2.2 The Development of the FDTD Method

World War II, and the Cold War prompted the development of radar for missile detection. This post-war development included the design of microwave sources, waveguides, antennas, circulators, and any other equipment that required the transportation or generation of microwaves [1]. The development of such systems are not strictly used for military purposes, however, as satellite technology would make use of this equipment during the same time frame and would require its own research. Microwave communications links, as well, for communications across great distances, would require much of the same technology as used for radar.

The study of the electromagnetic pulse (EMP) also prompted military study during the 60's. A nuclear bomb detonated above Earth's atmosphere would not only be an environmental disaster, but would cause an electromagnetic pulse strong enough to

disable electronic equipment on Earth's surface [1]. Substantial military effort has since been developed to counteract these possible effects.

Before the 1960's, closed form and infinite series solutions were the methods of choice for solving electromagnetic problems [1]. Since then, numerical solutions for electromagnetics have gained a rise in popularity because of the rise of availability of computers [1]. At first, these numerical solutions used frequency domain methods such as the Method of Moments (MoM) or the Finite Element Method (FEM). These methods, however, had limitations in the size of the problem that could be studied, since the methods produce a large matrix that must be solved. In addition, they had limitations in the type of materials that could be studied, where non-linear materials became problematic.

The FDTD method was originally proposed by Yee in 1966 [3], but it was not until the 70s and 80s that defense agencies began the use of this method [1]. The general electromagnetic community began to take interest in this method in the 90's, when an explosion of papers began to be published [1]. Since then, hundreds of papers are published each year in this area and innovations continue to improve the FDTD method. The Yee Cell is shown in Figure 2.1 and is described in more detail in Appendix A2.

2.2.1 Stability Considerations

As discussed in the previous sections and in Appendix A2, K.S. Yee first published the numerical FDTD method that is still popular today [3]. This method, however, relies on a time stepping method using approximations for first order derivatives as discussed in Appendix A1.

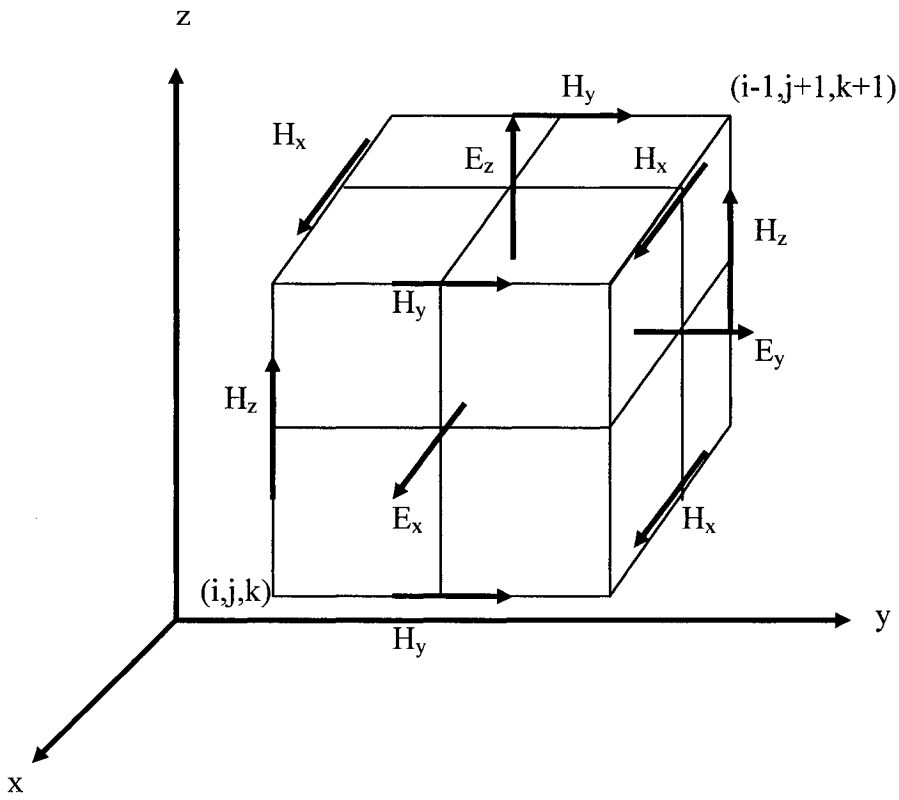

Figure 2.1: The Yee Cell [14]. The lower left corner is marked as coordinate (i,j,k), while the upper right is marked as (i-1, j+1, k+1). The center faces of the cell are at half steps.

The size of the time step, however, is limited in the original implementation of the FDTD method as first reported by Yee. Using a time step larger than this limit causes the solution space to become unstable and approach infinity. Allen Taflove was the first to report the correct numerical stability condition for the FDTD method in 1975, and coined the term FDTD in 1980 [1]. The stability condition is shown in equation (2.1), where the time step must be smaller than the time calculated by this equation to guarantee stability.

$$\Delta t < \frac{1}{c\sqrt{\frac{1}{(\Delta x)^2 + (\Delta y)^2 + (\Delta z)^2}}} \tag{2.1}$$

where
c is the speed of light
Δx is the grid spacing in the x-direction
Δy is the grid spacing in the y-direction
Δz is the grid spacing in the z-direction

Recently, different methods of combating instability have emerged. Although published as early as 1965 [4], the ADI method was not applied to FDTD until 1999 by Namiki [5] and independently in the same year by Zheng, Chen, Zhang [6]. In this method, the stability limit no longer exists, meaning any time step that can resolve the frequency band of interest can be used without the solution space becoming unstable.

The ADI method can be considered a second-order-in-time perturbation of the Crank-Nicolson scheme [1] that implements simplifications to this scheme to allow for easy step by step computation. Other methods use the Crank-Nicolson scheme directly, such as that implemented by Sun and Trueman [7] in 2004.

2.2.2 Anisotropy and Dispersion Considerations

The FDTD method uses difference equations along the x, y, and z axes to approximate derivatives as discussed in Appendix A1. This approximation causes the phase velocity of a wave to vary from the speed of light, depending on frequency, direction, or grid size, causing dispersion [1]. Because the difference equations are defined along the axes, a different phase velocity exists along the axes as compared to

diagonally within the FDTD lattice. This causes anisotropy. The anisotropy and dispersion phenomenon can lead to non-physical results [1] in a simulation.

The dispersion relation for a full-vector-field Yee mesh is given in Equation (2.2) below,

$$\left[\frac{1}{c\Delta t}\sin\left(\frac{\omega\Delta t}{2}\right)\right]^2 = \left[\frac{1}{\Delta x}\sin\left(\frac{\tilde{k}_x\Delta x}{2}\right)\right]^2 + \left[\frac{1}{\Delta y}\sin\left(\frac{\tilde{k}_y\Delta y}{2}\right)\right]^2 + \left[\frac{1}{\Delta z}\sin\left(\frac{\tilde{k}_z\Delta z}{2}\right)\right]^2 \tag{2.2}$$

The ideal dispersion case is

$$\left[\frac{\omega}{c}\right]^2 = [k_x]^2 + [k_y]^2 + [k_z]^2 \tag{2.3}$$

It can be shown that in the limit as Δt, Δx, Δy, and Δz approach 0, equation (2.2) approaches equation (2.3) [1]. Additionally, some special cases exist that allow for ideal dispersion along a diagonal, for example, if equation (2.4) is met. S is the Courant number.

$$\begin{aligned} &S = \frac{c\Delta t}{\Delta} = \frac{1}{\sqrt{3}} \\ &\tilde{k}_x = \tilde{k}_y = \tilde{k}_z = \frac{\tilde{k}}{\sqrt{3}} \\ &\textit{where} \\ &\Delta = \Delta x = \Delta y = \Delta z \end{aligned} \tag{2.4}$$

Several difference schemes have been devised to reduce numerical dispersion. Sun and Trueman, for example, have devised some methods of reducing numerical dispersion by using additional nodes around the point of differencing [8]. Additionally, they have identified three different categories of combating dispersion; coefficient optimization, higher order schemes / larger computational stencils, and hybrid methods that employ both coefficient optimization and larger computational schemes. By

optimizing the weighting of coefficients and using Neighborhood Averaging (NA) [9], they have eliminated anisotropy at one frequency.

A completely different method called the pseudospectral time-domain (PSTD) Method uses trigonometric functions or Chebyshev Polynomials to approximate derivatives, which greatly reduces dispersion error [1] and allows for coarse gridding of the solution space. The normal requirement in an FDTD environment is 10 to 20 cells per wavelength, however, recent advances in this area have shown good results with a low as π cells per wavelength [10]. Additionally, this new PSTD method has been improved so that it is unconditionally stable [11] using the ADI method [5] [6].

This new PSTD method, however, is not perfect. Since the derivatives are approximated along the whole lattice, any discontinuity such as a metallic plate, causes Gibb's Phenomenon, or ringing [1].

2.2.3 The Perfectly Matched Layer

The perfectly matched layer (PML) is a method of terminating the solution space for FDTD by adding a layer of perfectly absorbing material. The physical analogy of the PML is the wall of an anechoic chamber, where the wall absorbs all sounds in a room. If a PML was not used, an infinitely sized FDTD solution space would be required! With the PML, a typical maximum of a quarter wavelength of air in free space is required between the structure of interest and the PML wall, with some solutions requiring a minimum of only five to ten cells.

The first perfectly matched layer was published by Holland and Williams in 1983 [12], but could absorb waves of normal incidence only. Berenger's PML [13], on the

other hand, could absorb waves of normal and oblique incidence. The invention of the Uniaxial PML (UPML) [14] improved the performance of the PML significantly. The UPML has since become the most general method of termination of the FDTD lattice and has been implemented in several commercial software packages [1].

The PML, however, had its difficulties. Some waves of long duration were not sufficiently attenuated [15], and caused certain problems to be solved incorrectly. The implementation of the CPML in 2000 by Roden and Gedney [16] has proven efficient in avoiding this problem, and at the same time, improves performance of the PML significantly.

2.2.4 Conformal FDTD

One limitation of the FDTD method is that the lattice is built up of "building blocks", meaning a smooth surface must be approximated with many small blocks, leading to staircasing. This problem can be circumvented by the use of curvilinear coordinates [17], where a new coordinate system is used. Another possibility is the use of very fine subgrids based on the Helmholtz equation [18], or Ampere's Law in integral form [19].

Perhaps the most general solution to modeling a curved surface is the hybrid use of Finite Volume (FV) or Finite Element (FE) methods with FDTD. The hybrid FDTD-FV and FDTD-FE use a conformal sub-grid surrounded by a rectangular mesh. The FDTD-FE method solves the region of FE implicitly, while the FDTD mesh is solved explicitly [1] (See Figure 2.2).

The adoption of FE method in the time domain has been slow because using the nodal approach may suffer from spurious modes, just like the Finite Element Method (FEM) [20] [1], however this problem has since been solved by using vector-based edge vectors [21]. The adoption of the FV method has also been slow because of time-instability problems [1], but has still found its way into use [22].

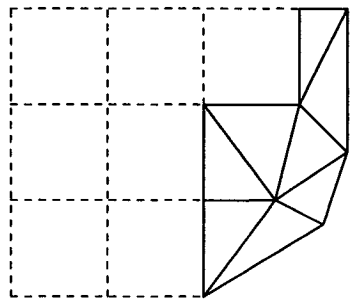

Figure 2.2: Squares that have complete Dotted Lines on their four sides are updated explicitly in the normal FDTD fashion. The triangular cells that do not border a square cell are updated with the normal FEM method. Square cells that border a triangular cell, or triangular cells that border a square cell must be updated in a fashion specific to FDTD-FE. [1]

2.2.5 Specialized Hardware

The FDTD method has become accepted enough such that commercial software is now readily available. The availability of cheap, and fast computers helps to achieve fast simulation times, allowing for optimized development of certain microwave components. The software itself may be modified to make use of certain hardware acceleration built into today's computers, such as the graphics accelerator [1]. Other methods of accelerating the running speed may even involve adding a dedicated hardware accelerator card to the computer [23].

2.3 Advancements in Broad and Dual Band Antenna Designs

The recent advancements in wireless communications devices have spawned a rapid need for antenna development. The need for faster communications requires larger bandwidths, which requires higher frequencies. This, in turn, requires the design of new antennas. Many new antennas are designed on a continual basis. The antennas discussed here are limited to antennas of small size and at frequencies below 10 GHz, which can be used for most wireless devices today.

2.3.1 Designs Related to this Thesis

In studying different designs, this thesis investigates slot antennas, microstrip antennas, and dielectric resonator designs. The FDTD method used in this thesis has mostly been used with microstrip and stripline designs, however, the potential bandwidth gains realized by using the coplanar waveguide design has led to a large portion of wideband antenna designs being published that use this feed mechanism. These papers, therefore cannot be ignored when studying broadband designs.

The first design that will be considered here is the co-planar-fed wideband rectangular microstrip slot antenna. This design can achieve extremely wide bandwidths [24], where the design by Chair, Kishk, and Lee achieved a bandwidth of greater than 110%, or a 10 dB bandwidth extending from 2.8 to 9.5 GHz. The layout of this antenna is shown in Figure 2.3. The substrate has a dielectric constant of 3.38 and the height of the dielectric is 0.813 mm.

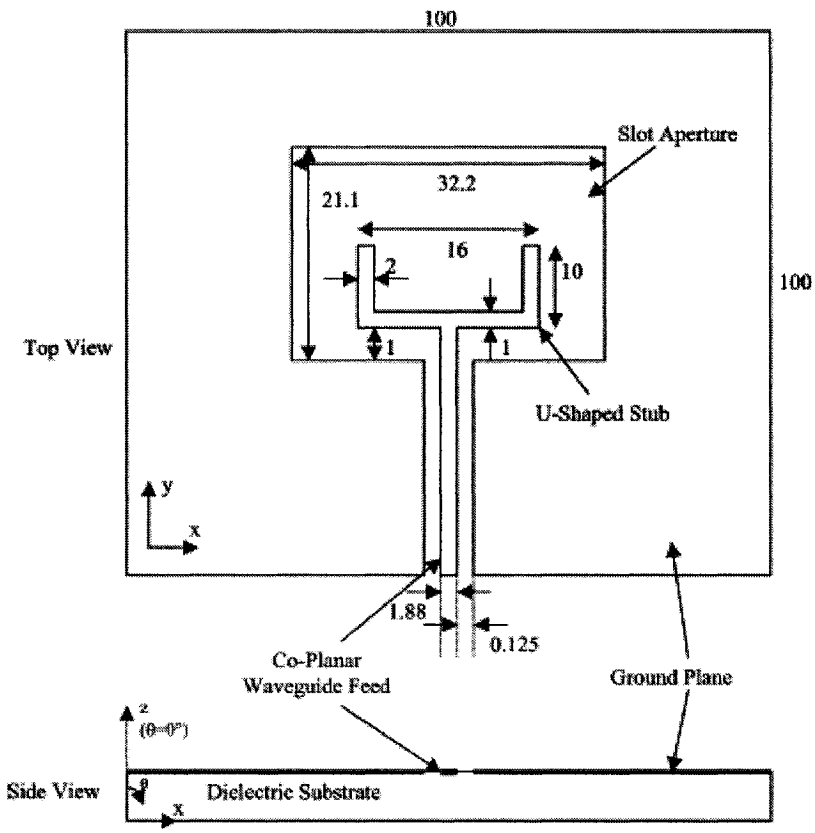

Figure 2.3: Wideband Co-planar fed rectangular slot antenna. Impedance Bandwidth extends from 2.8 to 9.5 GHz. [24]

Other techniques have been used to achieve a broadband impedance match, such as using a resonating structure (dielectric resonator antenna (DRA)), combined with a slot antenna [25], where the slot's resonance frequency and the dielectric resonator's frequencies consist of slightly different frequencies. Buerkle, Sarabandi, and Mosallaei have simulated and constructed the structure shown in Figure 2.4, where a 25% bandwidth was achieved from roughly 2 to 2.7 GHz. In their analysis, the FDTD method was used for simulation of return loss (S11) and for antenna patterns.

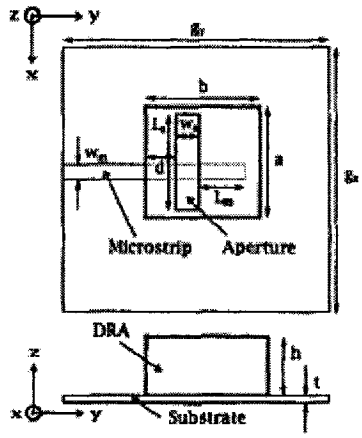

Figure 2.4: Dual Band structure using a DRA and a slot for dual resonance to achieve a 25% bandwidth. [25] The dielectric block is 2.67 cm x 2.67 cm x 1.67 cm and has a permittivity of 12. The substrate is 1.575 mm thick and has a dielectric constant of 2.2. The slot is 2 cm long by 0.5 cm wide.

In more recent years, slot antennas have appeared that have more radical shapes. The co-planar waveguide-fed Radial Slot antenna can also achieve broadband characteristics, as shown in Figure 2.5 below. This dual band design achieved 9.7% and 23.3% percent bandwidths at the lower and upper frequencies, respectively [26] at roughly 2 and 4 GHz.

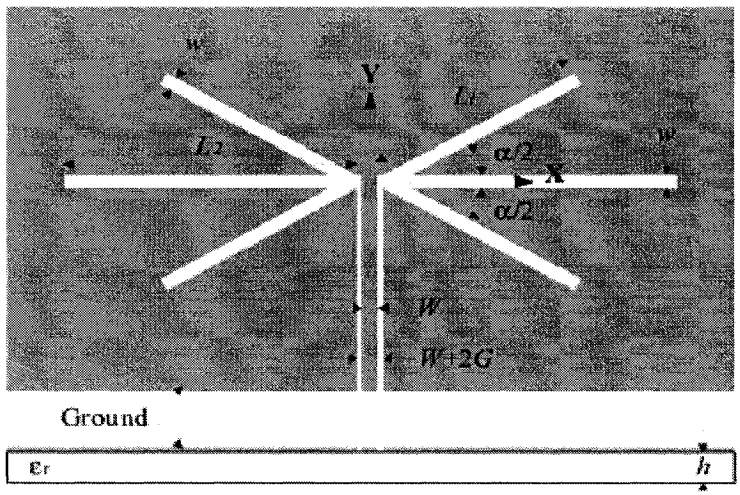

Figure 2.5: Radial Slot Design for broadband operation. [26]

The Volcano-shaped co-planar fed antenna shown in Figure 2.6 can also achieve wideband characteristics, where the 10 dB impedance bandwidth extends from 2 to 7 GHz [27].

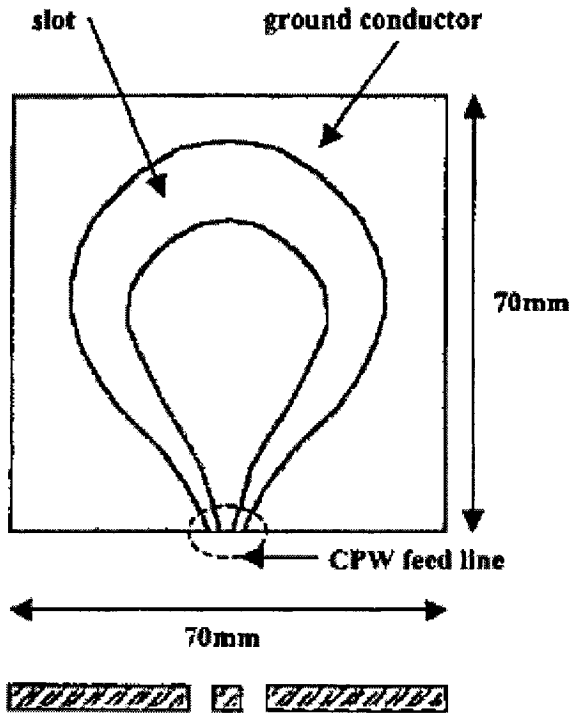

Figure 2.6: Co-planar waveguide-fed Volcano-Smoke-Shaped antenna with 10 dB Impedance Bandwidth extending from 2 to 7 GHz [27].

In Figure 2.7, the Hybrid Resonator antenna is shown [28]. This antenna achieves dual band operations using the disc for radiation at one frequency, and the slot for radiation at the second. Because the dielectric constant of the disc is high, there is a late-time interaction with the PML, which required the use of the Convolutional PML (CPML) for simulation in FDTD, as discussed in the next sections.

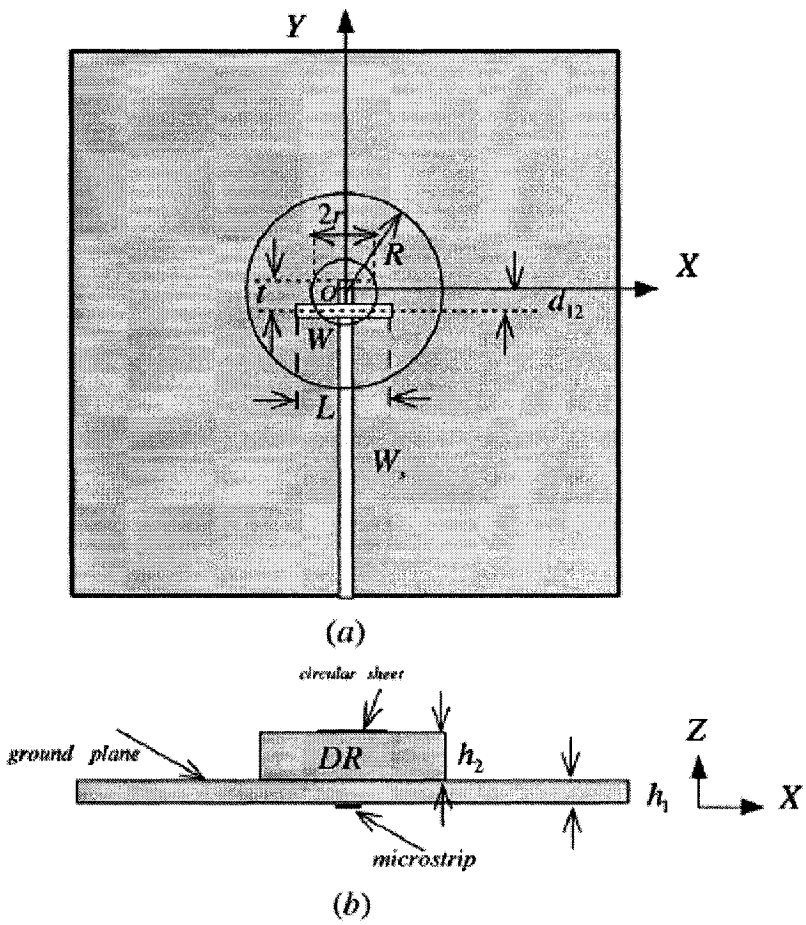

Figure 2.7: Hybrid Resonator antenna [28]. The dielectric constant of the disc is 35.5. The dielectric constant of the substrate is 3.38 and its thickness is 0.813 mm. The dimensions are L = 28 mm, Ws = W = 1.7 mm, R = 15 mm, r = 2 mm, h2 = 10.5 mm, d12 = 4 mm, t = 7 mm. The ground plane is 120 mm by 120 mm.

The U-slot has also gained interest, [29], where initial designs generated 10 dB bandwidths in the order of 27% at roughly 4 GHz. The design is shown in Figure 2.8 below. The designs found in publications are normally probe-fed. This design has been improved in [30], where the bandwidth has been increased to 53% using the addition of a metallic wall. This design, however, typically has a relatively tall height, where the substrate is 5 mm thick and has a dielectric constant of 2.33 in [29].

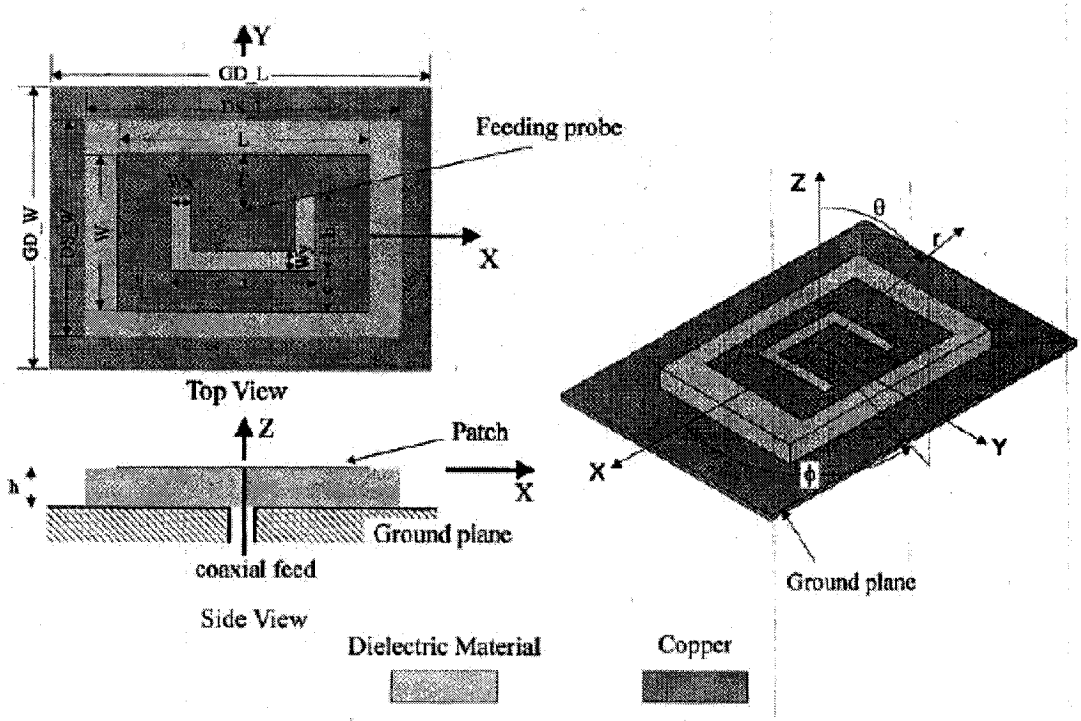

Figure 2.8: The U-Slot Antenna [29].

2.4 Summary

The FDTD method is still in a state of rapid evolution. The new techniques described in Section 2.2 just touch the surface of what is being explored, since there are hundreds of papers that are published in this area each year [1]. In this section we have discussed stability, dispersion, the PML, conformal FDTD, and specialized hardware.

Different methods of achieving wideband antennas relevant to this thesis have been discussed in Section 2.3. We have shown several antennas that used coplanar waveguide feeds, such as the radial slot [26], the rectangular slot [26], or the Volcano-shaped antenna [27]. Another method of achieving wideband characteristics is the dipole configuration in fractal [31] [32] or sectoral [33] forms. The U-slot [29] has been

discussed as well, however, is limited in that the height of the structure must be relatively large.

Chapter 3: FDTD Method: Optimization & Validation

3.1 Introduction

In this chapter we discuss techniques unique to this thesis and the validation steps taken to ensure the accuracy and reliability of the software. The mathematical development of the FDTD method and the Yee cell beginning with Maxwell's equations are presented in Appendix A2. The development of the PML beginning with Berenger's PML up to and including the CPML is discussed in Appendix A3. The Discrete Fourier Transform is used to transform the final results from time domain to frequency domain and is discussed in Appendix A4.

In this thesis, the CPML absorbing boundary condition was chosen for its many advantages over the currently available FDTD lattice terminations. As presented in Appendix A3, the advantages are

1. The classic tensor coefficient used in the UPML or classic Berenger PML can cause late-time / low-frequency reflections, where the CPML uses CFS tensors to overcome this problem. [16]
2. The FDTD update equations are not modified by the PML implementation in this thesis, thus maintaining the simplicity of the Yee algorithm. In fact, the PML is implemented by simply adding values to the E and H fields after they have been computed as per the Yee algorithm. In addition, unlike the UPML, there is no E/D or H/B dependence, which simplifies the modeling of different materials [1].
3. The CPML requires only two variables for the E field in the PML, and two for the H field, requiring a total of only four variables per cell in each PML wall. Other

PML implementations such as the UPML require three or more variables per E or H field and require storage within the *entire* computational domain. The CPML is thus very memory efficient, allowing for very fine grid sizes. [16]

4. The CPML is faster than the UPML, since the PML calculations take place only within the PML [1].

3.2 Edge Vector Prioritization for Boundary Conditions

The FDTD Method in its classic form has limitations in that each cell is the same size (for a non-graded mesh). The definition of certain structures therefore becomes memory-limited if enough cells are used. Various methods of overcoming these problems that have been used are averaging of coefficients [34] to describe round structures, or averaging dielectric constants between air and the material to describe a boundary for magnetic field conditions [35].

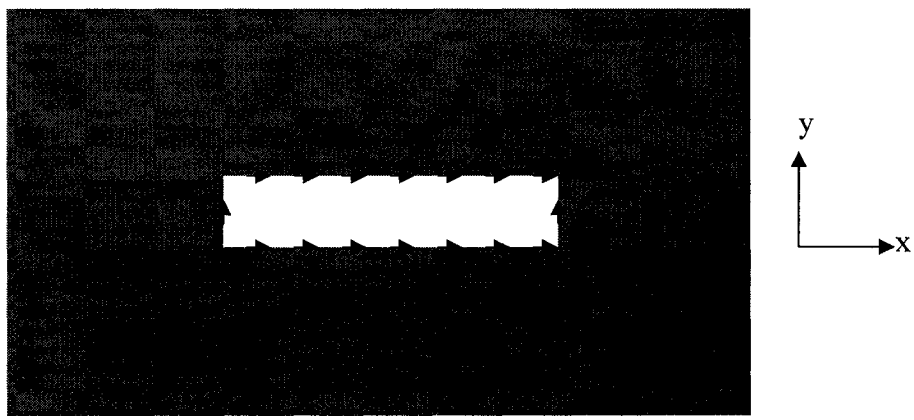

Figure 3.1: Slot in ground plane. White areas are the slot. The vectors shown would be designated as PEC, or E vectors that are enforced to be 0.

Consider the slot in a PEC ground plane as shown in Figure 3.1 above. The vectors shown in the diagram would be designated as PEC, where the distance between

the two Ey vectors would be the width of the slot, and the Ex vectors would be the height of the slot. Each vector may represent only one vector in a full Yee cell.

This may seem very intuitive at first, however, is not straightforward when dealing with the Yee cell because of the slight offset of the Ex and Ey vectors and the inherent limitations in FDTD. This is explained in the discussion that follows.

Consider a metallic plate that is 4 dx cells wide and 2 dy cells tall as drawn in Figure 3.2 below. All the vectors in the diagram must be set to the material of the plate. Notice that on the right edge, the x coordinate of the cell reached 5, and at the top, the coordinate reaches 3. These edge vectors must be added when defining a metallic plate [35]. Also referring to Figure 3.2, the Ex and Ey vectors are placed at (i+1/2, j, k) and (i, j+1/2, k), respectively, and must be represented this way in the structure.

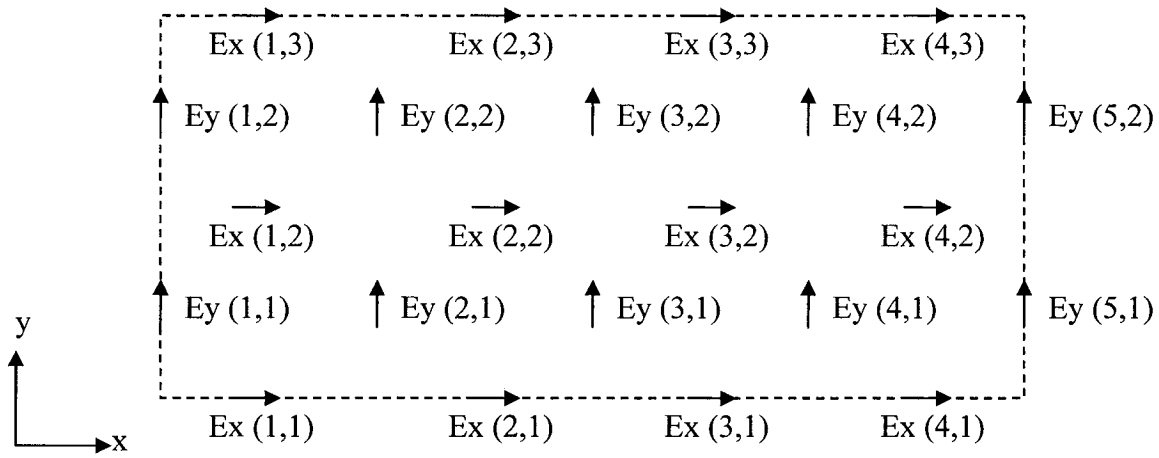

Figure 3.2: E vectors for a metallic plate that is 4 dx cells wide and 2 dx cells tall. The plate is outlined by the dotted line.

In the text by Kunz and Luebbers, for example, the above 4 x 2 plate would be defined to material "2" by the following Fortran code [35], where "NE" means "Not Equal", and IDONE and IDTWO are Ex and Ey vectors, respectively.

```
DO 10 I=1,5
DO 10 J=1,3
 IF (I.NE.5) IDONE(I,J,K)=2
 IF (J.NE.3) IDTWO(I,J,K)=2                    (3.1)
10 CONTINUE
```

For a slot in a PEC metallic plate, the inverse must be implemented, meaning edge vectors are not set to air, but left as PEC. Consider Figure 3.2, except consider that the dotted line represents an air slot in a metallic PEC plate that is 4 dx cells wide by 2 dz cells tall. In this case, all vectors in the diagram are set to air except the vectors along the dotted line, which are left as PEC. Using the same Fortran format as above, where material 1 is air, a 4 x 2 slot can be "cut" in a metallic plate as follows,

```
DO 10 I=1,4
DO 10 J=1,2
 IF (J.NE.1) IDONE(I,J,K)=1                    (3.2)
 IF (I.NE.1) IDTWO(I,J,K)=1
10 CONTINUE
```

Notice that the limits in the loop have changed, and the condition statement has changed as well. This example of prioritization of PEC over air forms the basis of the boundary conditions in this software.

In general, when dealing with dielectric and metallic plates such as in microstrip or stripline, priority of assignment of vectors must be implemented. In this software, the boundary conditions are set as per priority basis, with *tangential edge vectors infinitesimally thin structures then of the highest permittivity take priority*. Perfect conductors, for example, take priority over dielectrics, and dielectric take priority over air. Normal vectors take on the properties of the medium in question.

If slots must be cut into the ground plane, the convention in (3.2) must be used, where air replaces the PEC for Ex and Ey components. Note that for within the slot, air has taken priority over the dielectric. This is because we are modeling a thin ground plane that is below the dielectric, where any slots in the ground plane are physically air, not dielectric.

To illustrate this concept of priority, consider the microstrip structure shown above in Figure 3.3. First, Ex, Ey, and Ez vectors are set to dielectric as per the edge vectors in Figure 3.2. The ground plane is then set by replacing the Ex and Ey dielectric material vectors with PEC vectors at z = 1. The trace is then set by replacing the dielectric Ex and Ey vectors with PEC vectors at z = 3, where Ey vectors are set from x = 2 to z = 4 inclusive, and Ex vectors are set from x = 2 to x = 3 inclusive. The distance, then between the ground plane and the trace is 2 dz cells. The microstrip is excited as per the vectors in red in Figure 3.3, where Ez is excited from z =1 to z = 2 inclusive and from x = 2 to x = 4 inclusive.

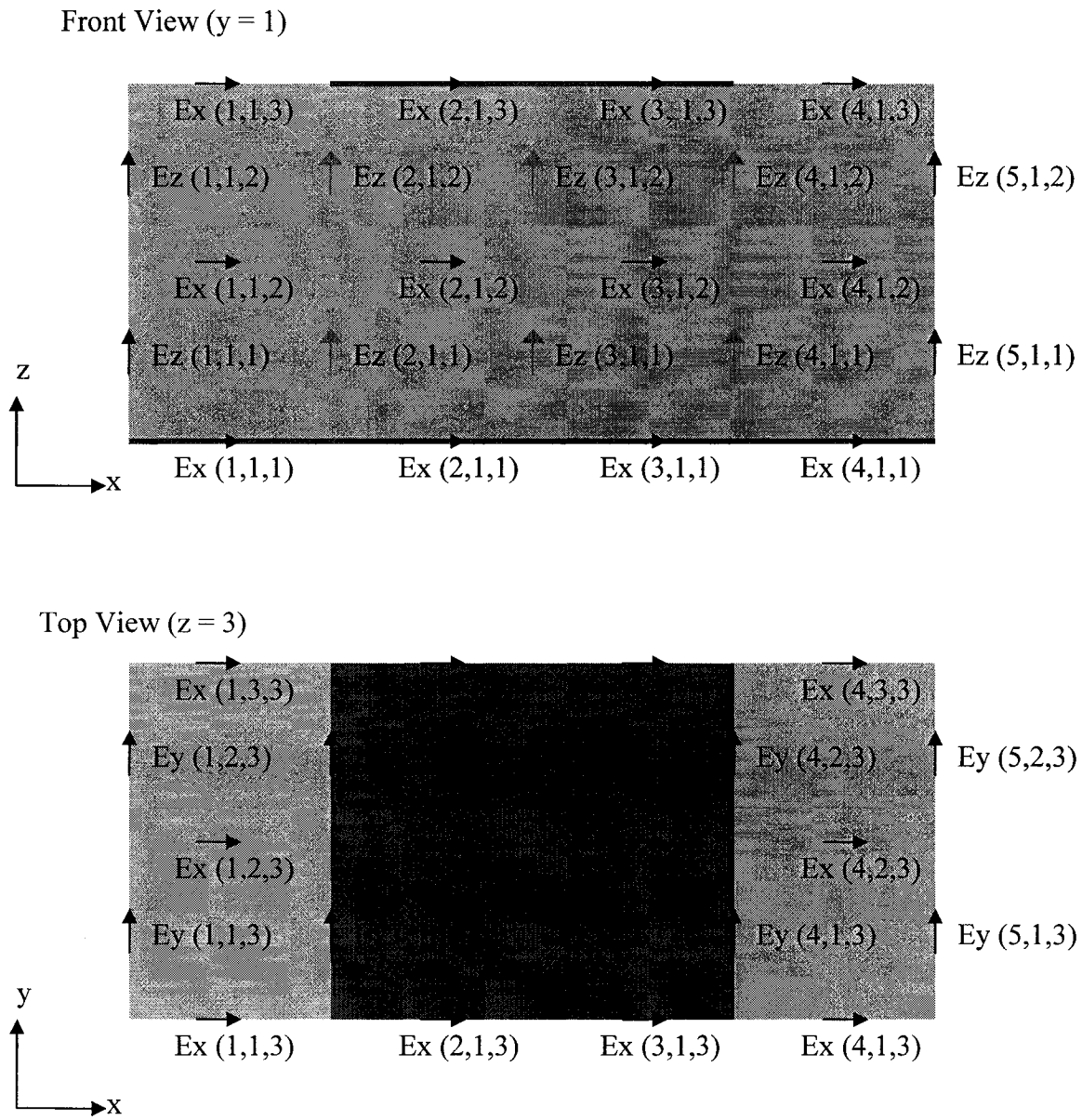

Figure 3.3: Assignment of metallic plates in a microstrip structure. In this case, the substrate is 2 cells tall, and the microstrip trace is 2 cells wide.

3.3 An Improved CPML Formulation: Isolation of CPML coefficients

The CPML formulation is very efficient in its implementation due to the fact that the ψ components need only be calculated and added to the individual vector components within the PML [14]. The κ components, however, have a value of 1.0 throughout the main solution space, however, still appear within the formulation in Equations (A3.34) through (A3.39). If left in this format, the software needs to either store values of $\kappa = 1.0$ throughout the solution space, or check to see if the computation lies within the PML to compute a set of FDTD equations without the κ component.

It is possible to remove the κ component from the core of the FDTD equations to reduce storage requirements or simplify the programming, depending on the implementation. The equations within the FDTD computation region then reduce to the standard Yee equations (A2.16) to (A2.21). This yields optimal simplicity / accuracy within the computational region and increases running speed / reduces storage at the same time.

Consider the standard CPML equation, repeated from (A3.34) for convenience,

$$E_x\Big|_{i+1/2,j,k}^{n+1/2} = C_{ax}\Big|_{i+1/2,j,k} Ex\Big|_{i+1/2,j,k}^{n-1/2} + C_{bx}\Big|_{i+1/2,j,k} \left(\begin{array}{l} \dfrac{H_z\Big|_{i+1/2,j+1/2,k}^{n} - H_z\Big|_{i+1/2,j-1/2,k}^{n}}{\kappa_{yj}\Delta y} - \dfrac{H_y\Big|_{i+1/2,j,k+1/2}^{n} - H_y\Big|_{i+1/2,j,k-1/2}^{n}}{\kappa_{zk}\Delta z} \\ + \psi_{Ex,y}\Big|_{i+1/2,j,k}^{n} - \psi_{Ex,z}\Big|_{i+1/2,j,k}^{n} \end{array} \right) \quad (3.3)$$

Without loss of generality, this may be written as

$$E_x\Big|_{i+1/2,j,k}^{n+1/2} = C_{ax}\Big|_{i+1/2,j,k} Ex\Big|_{i+1/2,j,k}^{n-1/2}$$
$$+ C_{bx}\Big|_{i+1/2,j,k} \left(\begin{array}{l} \left[\dfrac{H_z\Big|_{i+1/2,j+1/2,k}^{n} - H_z\Big|_{i+1/2,j-1/2,k}^{n}}{\Delta y} - \dfrac{H_z\Big|_{i+1/2,j+1/2,k}^{n} - H_z\Big|_{i+1/2,j-1/2,k}^{n}}{\Delta y} \right] \\ + \dfrac{H_z\Big|_{i+1/2,j+1/2,k}^{n} - H_z\Big|_{i+1/2,j-1/2,k}^{n}}{\kappa_{yj}\Delta y} \\ - \left[\dfrac{H_y\Big|_{i+1/2,j,k+1/2}^{n} - H_y\Big|_{i+1/2,j,k-1/2}^{n}}{\Delta z} - \dfrac{H_y\Big|_{i+1/2,j,k+1/2}^{n} - H_y\Big|_{i+1/2,j,k-1/2}^{n}}{\Delta z} \right] \\ - \dfrac{H_y\Big|_{i+1/2,j,k+1/2}^{n} - H_y\Big|_{i+1/2,j,k-1/2}^{n}}{\kappa_{zk}\Delta z} \\ + \psi_{Ex,y}\Big|_{i+1/2,j,k}^{n} - \psi_{Ex,z}\Big|_{i+1/2,j,k}^{n} \end{array} \right) \quad (3.4)$$

Notice that the two difference terms in (3.4) have been added and subtracted.

Consider now, grouping the second two components and factoring out the difference term,

$$E_x\Big|_{i+1/2,j,k}^{n+1/2} = C_{ax}\Big|_{i+1/2,j,k} Ex\Big|_{i+1/2,j,k}^{n-1/2}$$
$$+ C_{bx}\Big|_{i+1/2,j,k} \left(\begin{array}{l} \dfrac{H_z\Big|_{i+1/2,j+1/2,k}^{n} - H_z\Big|_{i+1/2,j-1/2,k}^{n}}{\Delta y} + \\ \left[\dfrac{1}{\kappa_{yj}} - 1 \right] \dfrac{H_z\Big|_{i+1/2,j+1/2,k}^{n} - H_z\Big|_{i+1/2,j-1/2,k}^{n}}{\Delta y} \\ - \dfrac{H_y\Big|_{i+1/2,j,k+1/2}^{n} - H_y\Big|_{i+1/2,j,k-1/2}^{n}}{\Delta z} \\ - \left[\dfrac{1}{\kappa_{zk}} - 1 \right] \dfrac{H_y\Big|_{i+1/2,j,k+1/2}^{n} - H_y\Big|_{i+1/2,j,k-1/2}^{n}}{\Delta z} \\ + \psi_{Ex,y}\Big|_{i+1/2,j,k}^{n} - \psi_{Ex,z}\Big|_{i+1/2,j,k}^{n} \end{array} \right) \quad (3.5)$$

If the κ components are 1.0 within the main solution space, the new terms disappear, yielding (A2.16). The new terms, then, can be added within the PML only. The finite difference equation is then, repeating from (A2.16),

$$E_x\Big|_{i+1/2,j,k}^{n+1/2} = C_{ax}\Big|_{i+1/2,j,k} Ex\Big|_{i+1/2,j,k}^{n-1/2} + C_{bx}\Big|_{i+1/2,j,k}\left(\frac{H_z\Big|_{i+1/2,j+1/2,k}^{n} - H_z\Big|_{i+1/2,j-1/2,k}^{n}}{\Delta y} - \frac{H_y\Big|_{i+1/2,j,k+1/2}^{n} - H_y\Big|_{i+1/2,j,k-1/2}^{n}}{\Delta z}\right) \tag{3.6}$$

This difference equation may now be calculated within the *entire* solution space, including the PML, in one loop.

Within the PML, the ψ components are then added after computation in (3.6), along with the new difference terms, as follows,

$$E_{x\,PML}\Big|_{i+1/2,j,k}^{n+1/2} = E_x\Big|_{i+1/2,j,k}^{n+1/2} + C_{bx}\Big|_{i+1/2,j,k}\left(\begin{array}{l}\left[\frac{1-\kappa_{yj}}{\kappa_{yj}}\right]\frac{H_z\Big|_{i+1/2,j+1/2,k}^{n} - H_z\Big|_{i+1/2,j-1/2,k}^{n}}{\Delta y} \\ -\left[\frac{1-\kappa_{zk}}{\kappa_{zk}}\right]\frac{H_y\Big|_{i+1/2,j,k+1/2}^{n} - H_y\Big|_{i+1/2,j,k-1/2}^{n}}{\Delta z} \\ +\psi_{Ex,y}\Big|_{i+1/2,j,k}^{n} - \psi_{Ex,z}\Big|_{i+1/2,j,k}^{n}\end{array}\right) \tag{3.7}$$

3.4 Memory and Speed Optimization of the Main FDTD Computation: An Object Oriented Approach

FDTD is a computationally intensive simulation approach. Any increase in computation speed is always welcome, and speed benchmarks between several different

software packages are common. Different strategies for increasing computing speed have been used, such as using the GPU (Graphical processing Unit) [1], or using a lower level programming language such as assembly language.

A more straightforward approach increasing running speed is to simply optimize the code itself. In general, public domain code that is written for FDTD has not been optimized for speed. This is most likely because code that is optimized for speed is often harder to read and harder to debug. Common commercial software practices usually include a step to optimize code for speed near the final steps of software completion. This includes reducing unnecessary loops, decreasing the amount of referencing for memory and amount of total memory used, pre-computing appropriate constants, and other strategies.

3.4.1 Loop Optimization

Consider the following loop in pseudo code:

```
for x = 1 to 10
  for y = 1 to 10
    for z = 1 to 10
      [do computation for x]                    (3.8)
    next z
  next y
next x
```

This loop goes through the entire solution space and does some computation for an x component. The next loop in a typical FDTD code would do the following

```
for x = 1 to 10
 for y = 1 to 10
  for z = 1 to 10
    [do computation for y]                    (3.9)
  next z
 next y
next x
```

and then the next loop would be

```
for x = 1 to 10
 for y = 1 to 10
  for z = 1 to 10
    [do computation for z]                    (3.10)
  next z
 next y
next x
```

In general, this is inefficient programming. If the x, y, then z components are computed this way, a total of 9 loops would have to be processed! The software must process the same triply nested loop three times. Consider instead the following loop:

```
for x = 1 to 10
 for y = 1 to 10
  for z = 1 to 10
```

```
        [do computation for x]
        [do computation for y]                                    (3.11)
        [do computation for z]
      next z
    next y
  next x
```

This is faster because the there is only 1 triply nested loop, instead of three triply nested loops. This concept may be used with FDTD because the Ex, Ey, and Ez components are computed separately.

3.4.2 Object Oriented Approach: A Yee Cell Object

Consider now, an object defined as a Yee cell which holds parameters for Ex, Ey, Ez, Hx, Hy and Hz. There may be millions of such cells in the computer memory. Each time the software requests a value of such a cell, or requests to change such a cell, the operating system must find the location of that particular cell within the computer's memory. It is possible to reduce such searching by creating a reference to that cell and then operating on it throughout one loop cycle. The loop in (3.11) can then find a single memory location for that cell at each loop iteration as follows:

```
for x = 1 to 10
  for y = 1 to 10
```

```
for z = 1 to 10
  [find memory location for cell (x,y,z)]
  [do computation for x in cell (x,y,z)]
  [do computation for y in cell (x,y,z)]                    (3.12)
  [do computation for z in cell (x,y,z)]
 next z
next y
next x
```

This encapsulated approach allows for rapid referencing of this single cell for each loop iteration.

3.5 Far Field Antenna Patterns

The Far Field Antenna Patterns are computed using the near to far field transformations as described in Balanis [2]. The following steps are performed:

1. Compute the frequency domain E and H from the time domain E and H fields in FDTD.
2. Compute electric field currents $\mathbf{J}_s$ and Magnetic field currents $\mathbf{M}_s$ on the surface of a box within the computational area from the E and H fields, respectively.
3. Compute functions $\mathbf{N}_\theta$, $\mathbf{N}_\Phi$, $\mathbf{L}_\theta$, $\mathbf{L}_\Phi$ (derived from Vector Potentials) over the surface of the box from currents $\mathbf{J}_s$ and $\mathbf{M}_s$.
4. Compute **E** in the far field from the functions $\mathbf{N}_\theta$, $\mathbf{N}_\Phi$, $\mathbf{L}_\theta$, $\mathbf{L}_\Phi$.
5. Compute the maximum Directivity, Dmax, as in [37], by integrating the E field over the complete sphere.

6. Output final Directivity Results

3.5.1 Far Field Step 1: Compute E and H fields in the Frequency Domain

The E and H fields are computed using the Fourier transform of the time domain field, as in [34].

$$E(f) = \int_0^T E(t) e^{-j2\pi ft} dt \tag{3.13}$$

Using the rectangular rule for numerical integration, we obtain

$$E(f) = \sum_{n=0}^{T} E(n\Delta t) e^{-j2\pi f(n\Delta t)} \Delta t \tag{3.14}$$

Where Δt is the time step and T is the number of steps (integer value).

Note that for a single run, the E and H fields may be computed for several frequencies, where only the complex value of the field in the frequency domain must be stored for each location on the surface of the surface current box. (See Step 2 below for a description of the surface current box).

3.5.2 Far Field Step 2: Surface Currents

The surface currents must be computed on the surface of the box. The surface of the box is in the near field but surrounds the computational area. See Figure 3.4 below.

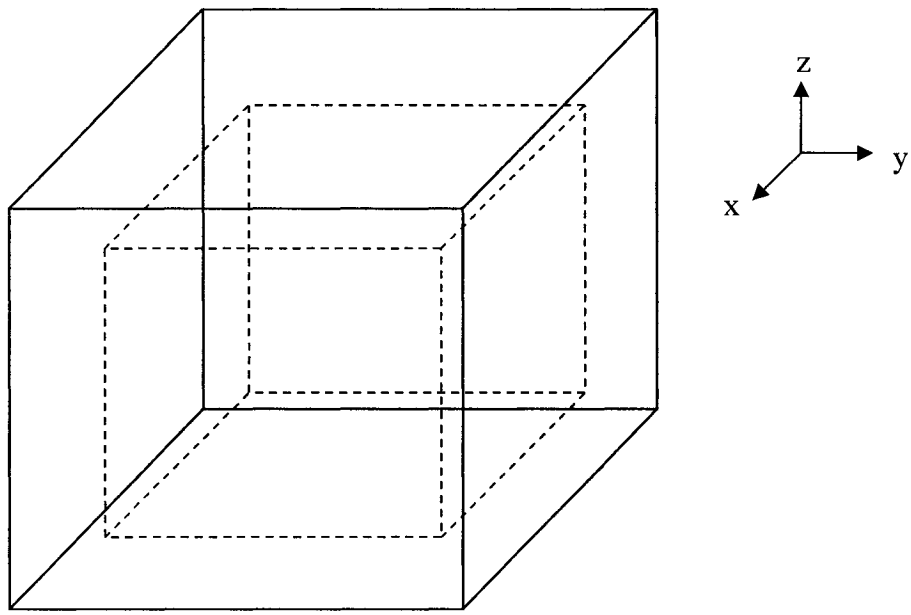

Figure 3.4: Dotted line shows the equivalent surface current box. The solid line is the FDTD computational area. The PML lies outside the solid line.

The equivalent surface currents can be computed with the computation of the cross products [2] over the surface of the equivalent surface current box:

$$\mathbf{J}_s = \hat{\mathbf{n}} \times \mathbf{H}_a \tag{3.15}$$

$$\mathbf{M}_s = -\hat{\mathbf{n}} \times \mathbf{E}_a \tag{3.16}$$

Where $\hat{\mathbf{n}}$ is a unit vector normal to the surface S of the box, and $\mathbf{E}_a$ and $\mathbf{H}_a$ are total Electric and Magnetic fields over the surface S of the box.

For the bottom of the box, or the x-y plane at z_{min}, the cross product can be calculated as follows, [2]

$$\mathbf{J}_s = \hat{\mathbf{n}} \times \mathbf{H} = \begin{vmatrix} \hat{\mathbf{i}} & \hat{\mathbf{j}} & \hat{\mathbf{k}} \\ 0 & 0 & -1 \\ H_x & H_y & H_z \end{vmatrix} = \hat{\mathbf{i}} H_y - \hat{\mathbf{j}} H_x \tag{3.17}$$

Similarly, at the top of the box, or the x-y plane at z_{max}, the cross product is

$$\mathbf{J}_s = \hat{\mathbf{n}} \times \mathbf{H} = \begin{vmatrix} \hat{\mathbf{i}} & \hat{\mathbf{j}} & \hat{\mathbf{k}} \\ 0 & 0 & 1 \\ H_x & H_y & H_z \end{vmatrix} = -\hat{\mathbf{i}} H_y + \hat{\mathbf{j}} H_x \tag{3.18}$$

For the yz plane at x_{min},

$$\mathbf{J}_s = \hat{\mathbf{n}} \times \mathbf{H} = \begin{vmatrix} \hat{\mathbf{i}} & \hat{\mathbf{j}} & \hat{\mathbf{k}} \\ -1 & 0 & 0 \\ H_x & H_y & H_z \end{vmatrix} = \hat{\mathbf{j}} H_z - \hat{\mathbf{k}} H_y \tag{3.19}$$

For the yz plane at x_{max},

$$\mathbf{J}_s = \hat{\mathbf{n}} \times \mathbf{H} = \begin{vmatrix} \hat{\mathbf{i}} & \hat{\mathbf{j}} & \hat{\mathbf{k}} \\ 1 & 0 & 0 \\ H_x & H_y & H_z \end{vmatrix} = -\hat{\mathbf{j}} H_z + \hat{\mathbf{k}} H_y \tag{3.20}$$

For the zx plane at y_{min},

$$\mathbf{J}_s = \hat{\mathbf{n}} \times \mathbf{H} = \begin{vmatrix} \hat{\mathbf{i}} & \hat{\mathbf{j}} & \hat{\mathbf{k}} \\ 0 & -1 & 0 \\ H_x & H_y & H_z \end{vmatrix} = -\hat{\mathbf{i}} H_z + \hat{\mathbf{k}} H_x \tag{3.21}$$

For the zx plane at y_{max},

$$\mathbf{J}_s = \hat{\mathbf{n}} \times \mathbf{H} = \begin{vmatrix} \hat{\mathbf{i}} & \hat{\mathbf{j}} & \hat{\mathbf{k}} \\ 0 & 1 & 0 \\ H_x & H_y & H_z \end{vmatrix} = \hat{\mathbf{i}} H_z - \hat{\mathbf{k}} H_x \tag{3.22}$$

The Magnetic field currents, **M**, may be found using the same process.

3.5.3 Far Field Step 3: Compute Functions N and L

The functions N and L, derived from Vector potentials A and F can be found by evaluating the following integrals [2] for spherical coordinates,

$$
\begin{aligned}
N_\theta &= \iint_S \left(J_x \cos\theta\cos\phi + J_y \cos\theta\sin\phi - J_z \sin\theta\right) e^{+j\beta r'\cos(\psi)} ds' \\
N_\phi &= \iint_S \left(-J_x \sin\phi + J_y \cos\phi\right) e^{+j\beta r'\cos(\psi)} ds' \\
L_\theta &= \iint_S \left(M_x \cos\theta\cos\phi + M_y \cos\theta\sin\phi - M_z \sin\theta\right) e^{+j\beta r'\cos(\psi)} ds' \\
L_\phi &= \iint_S \left(-M_x \sin\phi + M_y \cos\phi\right) e^{+j\beta r'\cos(\psi)} ds'
\end{aligned}
\tag{3.23}
$$

For rectangular coordinates, the exponential term reduces to

$$
\begin{aligned}
& e^{+j\beta r'\cos(\psi)} = \cos(\beta r'\cos\psi) + j\sin(\beta r'\cos\psi) \\
& \textit{where} \\
& r'\cos\psi = x'\sin\theta\cos\phi + y'\sin\theta\sin\phi + z'\cos\theta
\end{aligned}
\tag{3.24}
$$

The variables x', y', and z' represent the distance of the surface of one side of the box from the origin [1]. If the surface of the box is on the origin, some terms may disappear, as in [2].

3.5.4 Far Field Step 4: Compute E from N and L

The electric field in the far field can be computed using equations in [2],

$$
\begin{aligned}
E_r &= 0 \\
E_\theta &= -\frac{j\beta e^{-j\beta r}}{4\pi r}\left(L_\phi + \eta N_\theta\right) \\
E_\phi &= +\frac{j\beta e^{-j\beta r}}{4\pi r}\left(L_\theta - \eta N_\phi\right)
\end{aligned}
\tag{3.25}
$$

3.5.5 Far Field Step 5: Maximum Directivity

The maximum directivity (D_o) can be found using the beam solid angle (Ω_A) [37] as follows,

$$D_o = \frac{4\pi}{\Omega_A}$$

where

$$\Omega_A = \int_0^{2\pi}\int_0^{\pi} F_n(\theta,\phi)\sin(\theta)d\theta d\phi$$

and (3.26)

$$F_n(\theta,\phi) = \frac{F(\theta,\phi)}{F(\theta,\phi)\big|_{\max}}$$

where

$$F(\theta,\phi) = \frac{1}{B_o}\frac{1}{2\eta}\left[\left|E_\theta\right|^2 + \left|E_\phi\right|^2\right]$$

B_o is a constant that does not need to be computed.

The solid angle Ω_A is computed using the rectangular rule for integration. For a perfectly isotropic antenna, D_0 is equal to 1, so Ω_A is equal to 4π.

3.5.6 Far Field Step 6: Output Results

Finally, the Directivity can be output as [37]

$$D(\theta,\phi) = D_o \times F_n(\theta,\phi) = D_o \times \frac{F(\theta,\phi)}{F(\theta,\phi)\big|_{\max}} \quad (3.27)$$

3.6 Far Field: Special Considerations for FDTD

When computing the far field pattern for an FDTD problem, it is important to take special consideration for the locations of the vectors in the problem space.

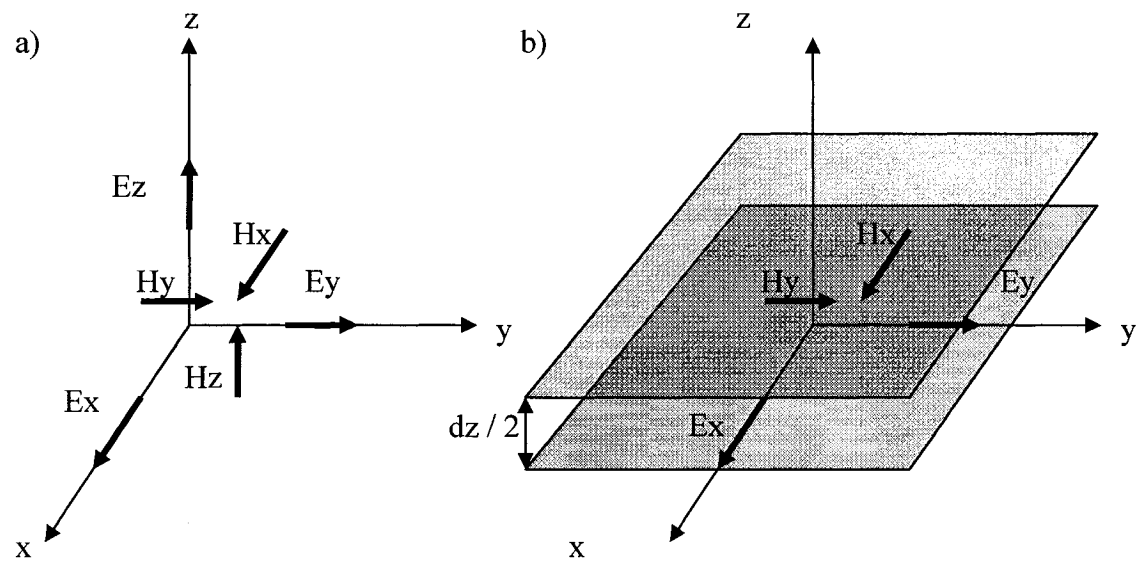

Figure 3.5: In a) the location of E and H field Vectors, for 1 cell, is shown, where the beginning of each arrow marks the vector location. [34] Ez is located at (0,0, dz / 2), for example. In b), notice that the Hx and Hy vectors are placed dz / 2 away from the Ey and Ex vectors.

When computing surface currents, as described in section 3.5, only the tangential E and H fields contribute to the desired results. These tangential E and H fields, however, are at different distances to the origin as shown in Figure 3.5a.

For the x-y plane, for example, the Ex and Ey vectors are in the x-y plane at z = 0, however, the Hx and Hy vectors are in the x-y plane at z = + dz / 2. This discrepancy must be taken into account when computing the N and L functions, as shown in Figure 3.5b and Figure 3.6.

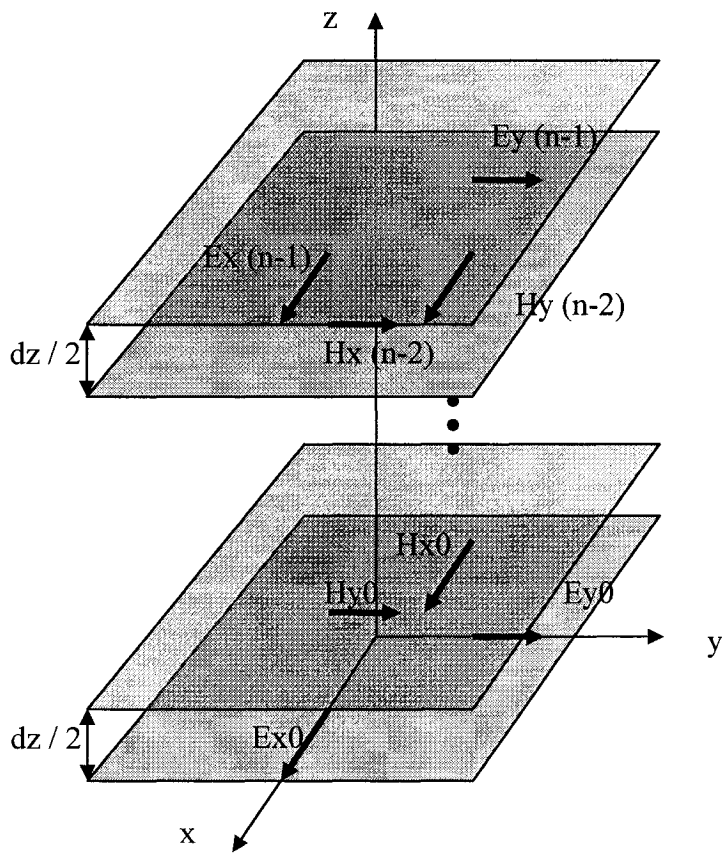

Figure 3.6: Half-Cell Separation of E and H planes. Notice that the H plane belongs to the n-2 cell at the zmax plane, where n cells are used in the z direction. The first and last cells are 0 and n-1, respectively.

This cell was drawn assuming the z_{min} position. At the z_{max} position, the Hx and Hy vectors are also offset by + dz / 2. To maintain symmetry of the problem, it is preferable to use the Hx and Hy vectors that are offset by – dz / 2 for the z_{max} position. The E field surface current box is then dz larger than the H field box in the z direction, dx larger in the x direction, and dy larger in the y direction.

3.6.1 Far Field Computation Validation

To verify the integrity of the software, several checks were performed, as follows:

1) verify the far field pattern of a rectangular slot where the E-fields are known within the slot
2) verify the antenna pattern of a half wavelength dipole at 10 GHz
3) verify the antenna pattern of a simple slot antenna, discussed in Section 3.10.3.

3.6.2 Far Field Validation Step 1) far field pattern of a rectangular slot

In this problem, the antenna pattern of a rectangular slot surrounded by an infinite ground plane is considered as shown in Figure 3.7. This problem is chosen because the solution to this problem is known analytically [2].

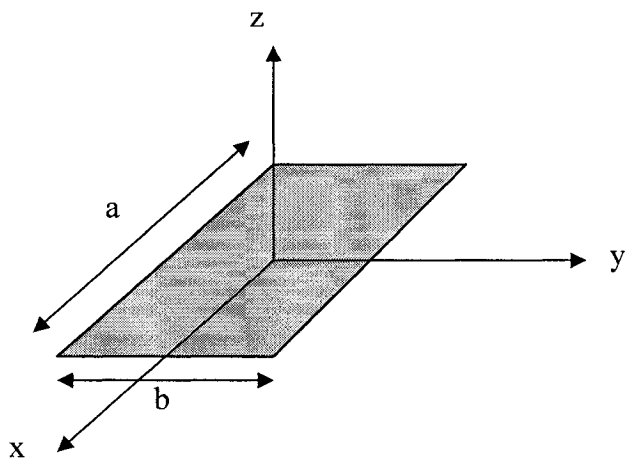

Figure 3.7: Rectangular Aperture with dimensions a and b in the x-y plane. The grey area marks the rectangular aperture where the electric field exists. Outside this box, the field on the xy plane, the tangential fields are zero because a PEC exists.

Since the electric field is known precisely, the currents J and M are known precisely, and so the software may be verified for its N, L, and E computation before the

currents J or M are even computed. Also, since the aperture lies in the x-y plane, there is no surface current box, only a surface current plane.

If the Electric field is constant over the aperture, the equivalent surface currents may be written as [37]

$$\begin{aligned} \mathbf{M}_s &= -2\hat{n} \times E_a = -2\hat{a}_z \times \hat{a}_y = \hat{a}_x 2E_o \\ \mathbf{J}_s &= 0 \end{aligned} \tag{3.28}$$

The far field antenna patterns may then be described as

$$\begin{aligned} E_r &= 0 \\ E_\theta &= \frac{jabE_o e^{-jkr}}{2\pi r}\left[\sin\phi\left(\frac{\sin X}{X}\right)\left(\frac{\sin Y}{Y}\right)\right] \\ E_\phi &= \frac{jabkE_o e^{-jkr}}{2\pi r}\left[\cos\theta\cos\phi\left(\frac{\sin X}{X}\right)\left(\frac{\sin Y}{Y}\right)\right] \\ H_r &= 0 \\ H_\theta &= \frac{-E_\phi}{\eta} \\ H_\phi &= \frac{E_\theta}{\eta} \\ &\textit{where} \\ X &= \frac{ka}{2}\sin\theta\cos\phi \\ Y &= \frac{kb}{2}\sin\theta\sin\phi \end{aligned} \tag{3.29}$$

The results matched almost perfectly (See Figure 3.8). One reason for this is that a rectangular rule for integration was used, and the distribution of the current over the slot can be perfectly modeled as a rectangular block.

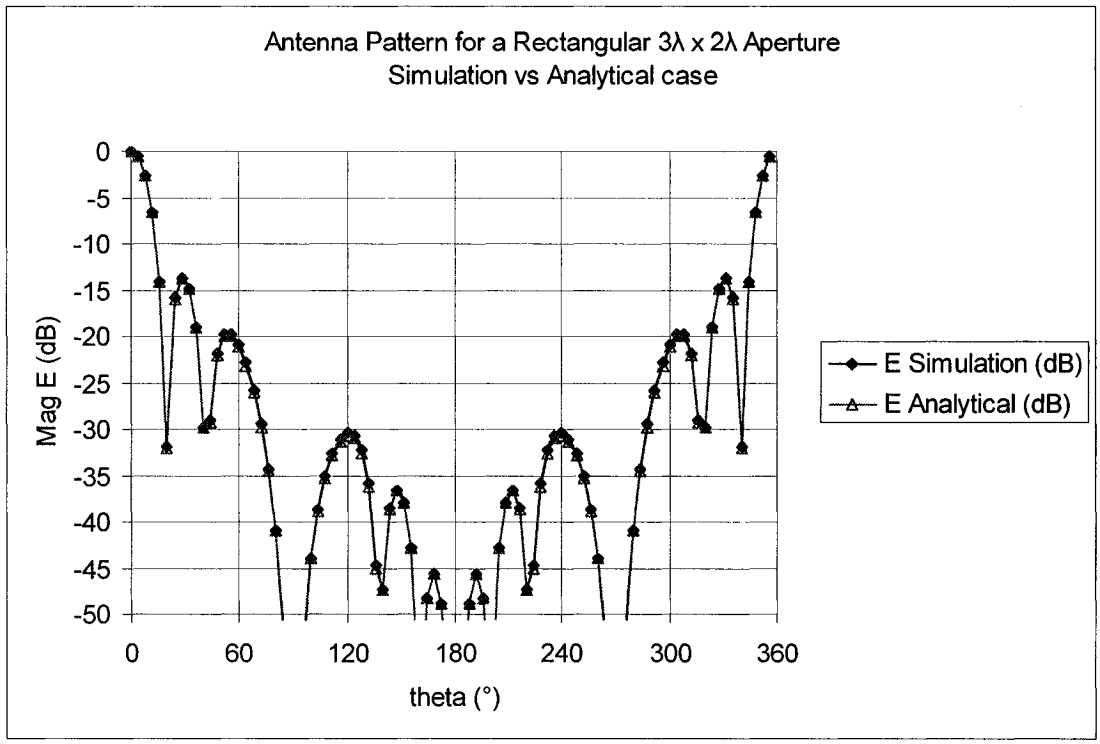

Figure 3.8: Comparison of Simulated Antenna Pattern vs Analytical solution for a Rectangular 3λ x 2λ Aperture, where a constant E-field is present within the slot.

3.6.3 Far Field Validation Step 2: ½ Wavelength Dipole at 10 GHz.

For the second validation check, the ½ Wavelength dipole (see Figure 3.9) was simulated in FDTD, where the full surface current box was used. The dipole was chosen because again, the analytical solution is well known. This problem, however, must make use of the full surface current box. All the steps as described in the sections above must therefore be performed to obtain the far field radiation pattern.

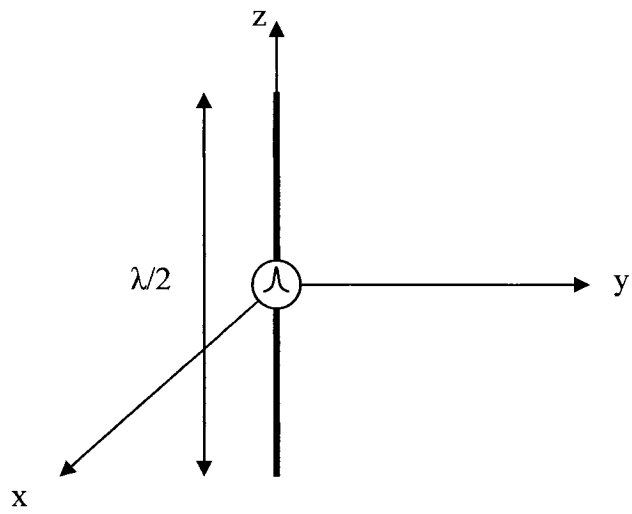

Figure 3.9: λ/2 Dipole excited by a Gaussian Pulse

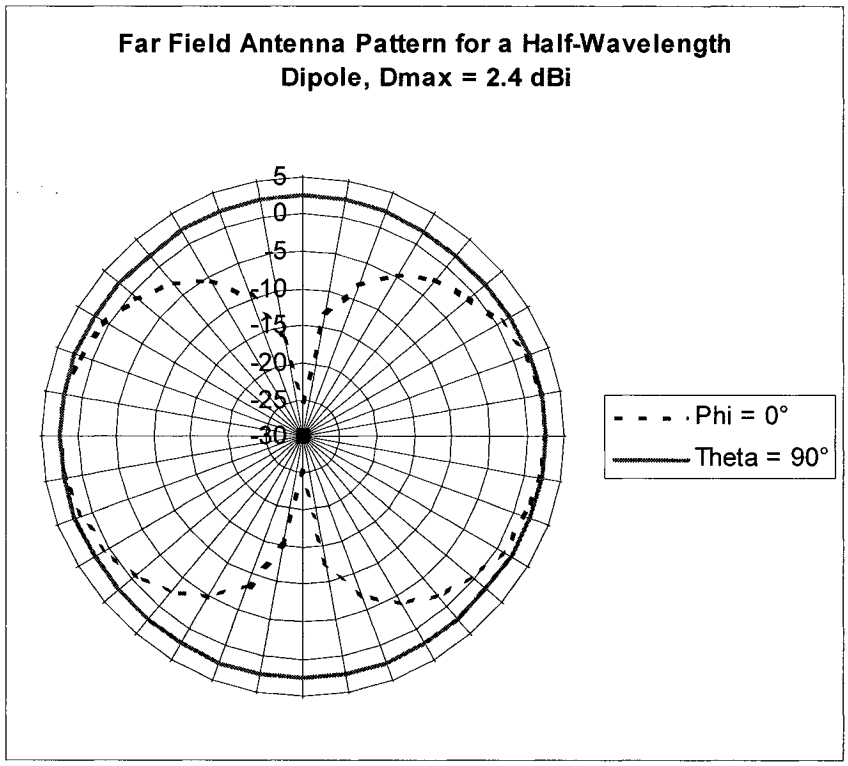

Figure 3.10: Simulation of a Far Field Antenna pattern for a z-axis oriented Half-Wavelength Dipole.

As can be seen in Figure 3.10, the results for the Dipole are acceptable.

3.7 PML Validation: Simple Dipole Antenna

The Dipole Antenna was simulated to verify the integrity of the FDTD codes and to view the performance of the PML in the time domain. The dipole is identical to that used in Figure 3.8.

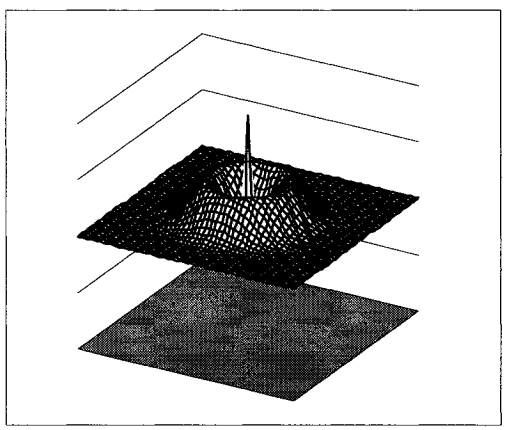

a) T = 35

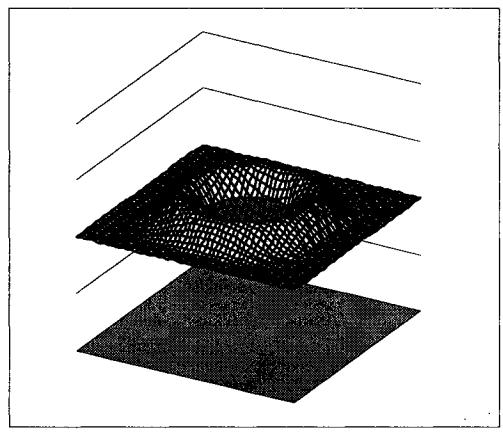

b) T = 43

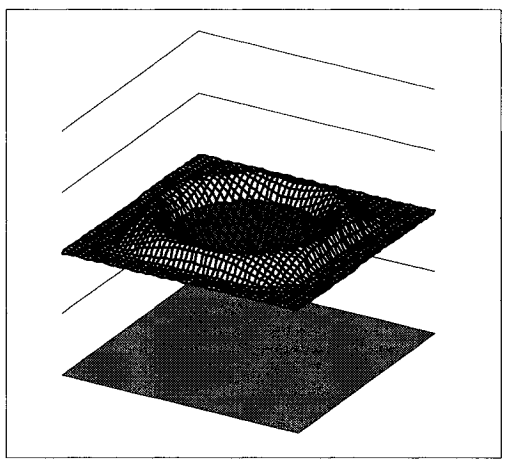

c) T = 50

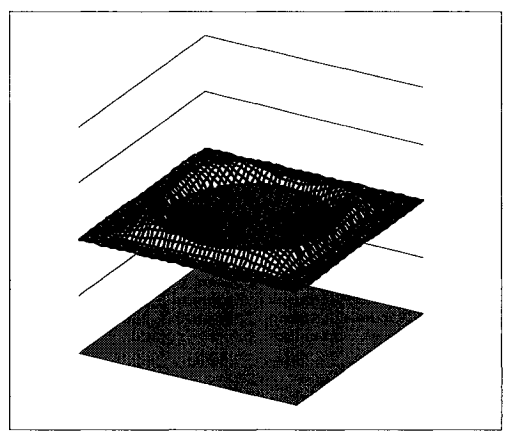

d) T = 55

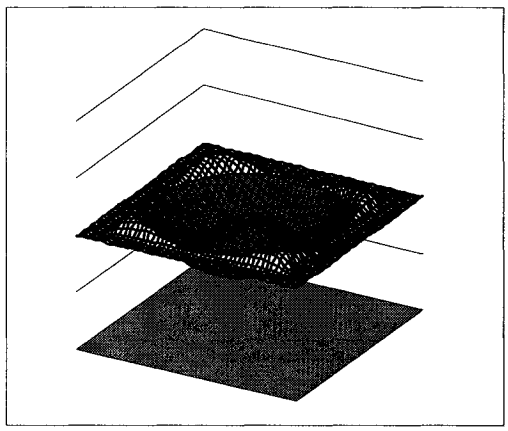

e) T = 60

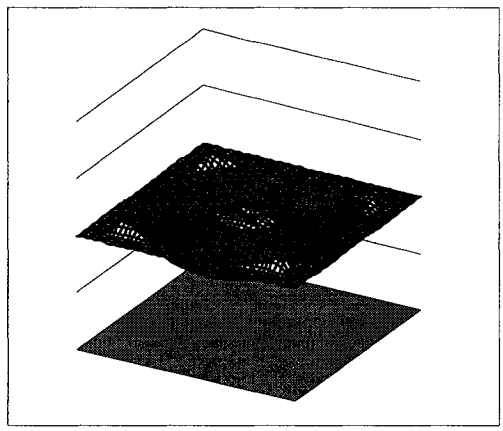

f) T = 65

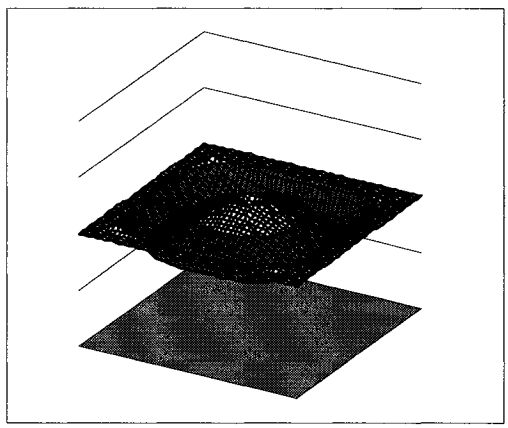

g) T = 70

Figure 3.11: 3D Plots of Ez in the Z plane for a Z-directed half wavelength Dipole at time a) T = 35, b) T = 43, c) T = 50, d) T = 55, e) T = 60, f) T = 65, g) T = 70. Time step: $1.829541541469147 \times 10^{-12}$ s.

In the Figure 3.11 above, the 3D and 2D plots of Ez in the Z-plane shows the Ez field in the time domain. Notice that the center of the plot (outside the PML) remains

circular, and there are no reflections that are introduced into the solution space. Reflections would appear as oppositely curved waves as to the incident waves.

3.8 Return Loss Validation: Microstrip Patch Antenna

The microstrip circuit was modeled as a layer of dielectric with permittivity 2.2 and no loss. The dielectric was placed on top of a ground plane and surrounded on the five other sides by a 10 layer PML. The microstrip patch or filter was then placed on the surface of the substrate by enforcing tangential electric fields to zero. The dimensions of the patch are shown in Figure 3.12.

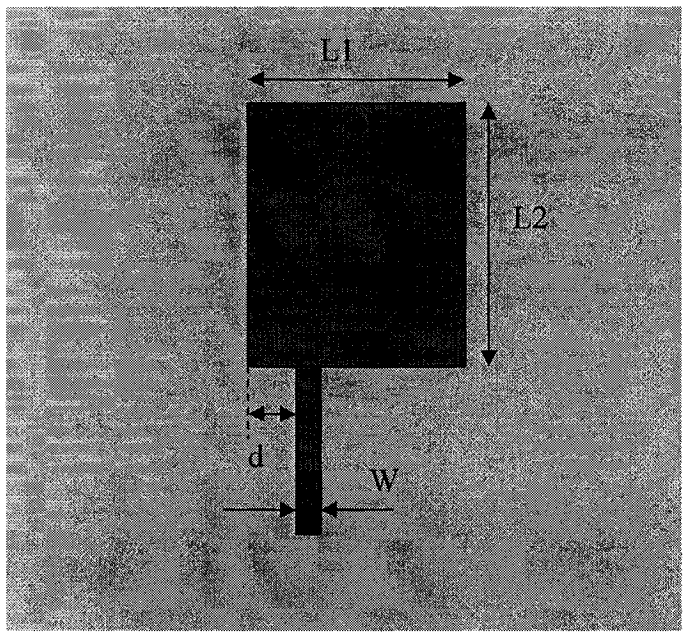

Figure 3.12: Sheen's Patch. L1 = 12.45 mm, L2 = 16.00 mm, d = 2.09 mm, W = 2.46 mm, e_r = 2.2, h = 0.794 mm.

The source was generated by exciting an electric field under the microstrip line adjacent to the PML as shown in Figure 3.13. One side of the propagating wave was dissipated in the PML, while the other traveled along the transmission line. The S11

parameter was obtained by monitoring the z-directed electric field one cell under the microstrip line, five cells from the source. The input was taken as the first 400 points, and the output was taken as the rest of the time domain data.

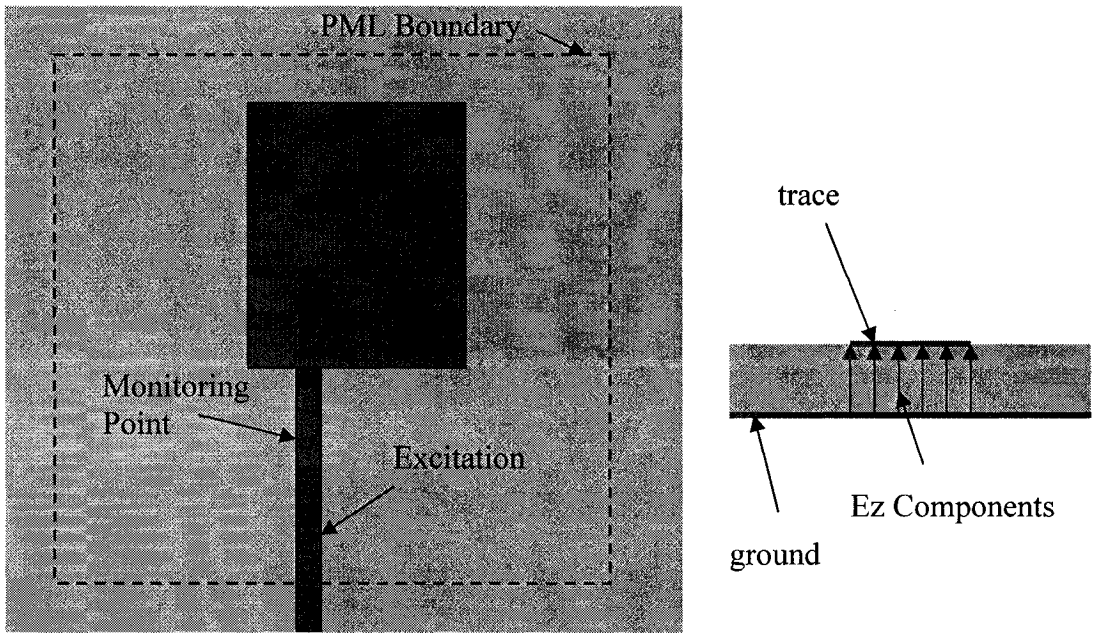

Figure 3.13: Excitation of Microstrip. The microstrip is excited in the substrate underneath the trace, and is monitored further down the microstrip after evanescent modes have attenuated. The Ez components are excited and monitored.

The simulation was run for 10000 time steps in both cases, where the magic time step was used. For the minimum grid size (see Table 4.1), the time step was calculated to be 0.442 ps.

Direction	per cell
X	0.389 mm
Y	0.400 mm
Z	0.265 mm

Table 4.1: Grid sizes

The DFT was performed by taking the DFT of the input and the DFT of the output, then dividing the output by the input. The results are presented in logarithmic form. The DFT was computed with custom software using 20000 points with zero padding to increase the resolution of the plots. (See Appendix A4 for more details about the DFT)

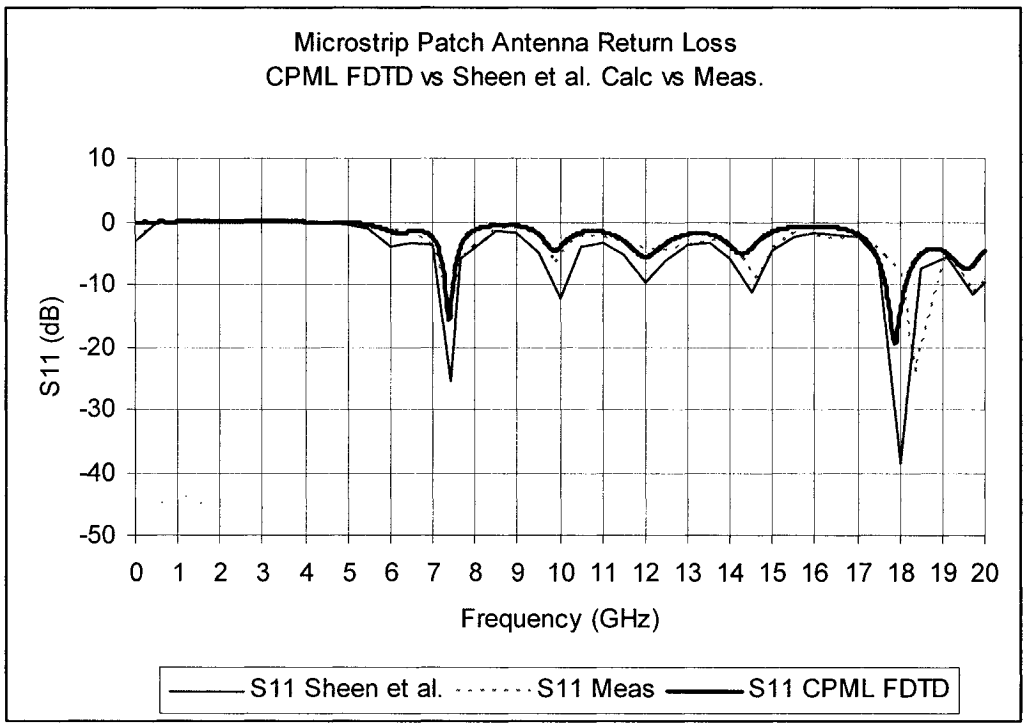

Figure 3.14: Return loss shown for Sheen's Patch. Results were similar to experimental data and Sheen et al.'s simulation.

3.9 Return Loss Validation: Lowpass Filter

To further verify the integrity of the FDTD codes, a microstrip low pass filter was simulated as in Sheen et al. [37] as shown in Figure 3.15. The results were again very close, however, the resonant frequencies were again displaced slightly lower than the work by Sheen et al. The highest resonant frequency in Sheen et al.'s paper was about

15.0 GHz, where the simulation showed 14.8 GHz. The simulation results are shown in Figure 3.16.

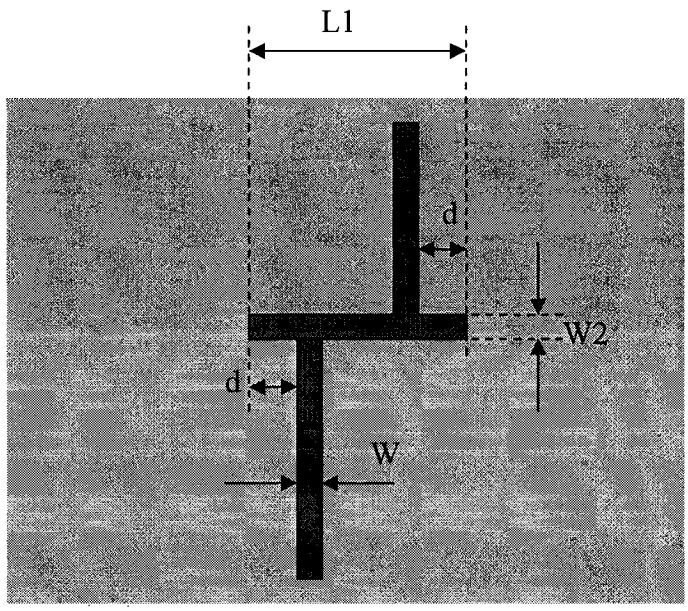

Figure 3.15: L1 = 20.32 mm, d = 5.65 mm, W = 2.413 mm, W2 = 2.54 mm, h = 0.794 mm, e_r = 2.2. [37]

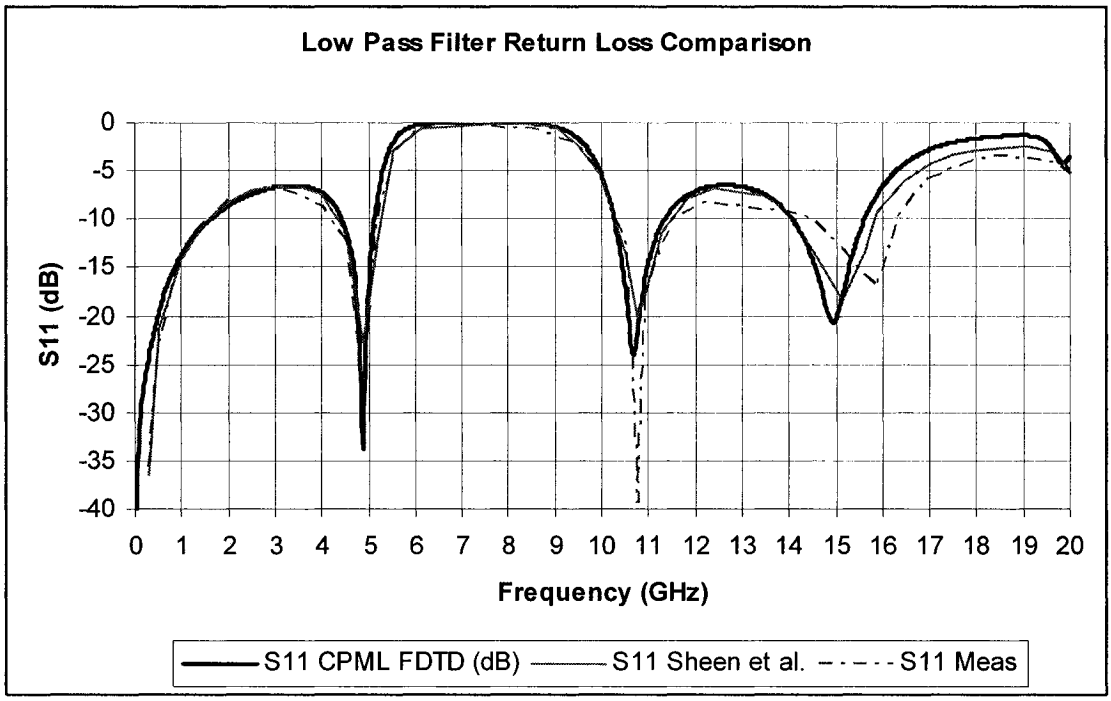

Figure 3.16: Lowpass filter as simulated in the paper by Sheen et al. [37] Results for the measured data are from [37].

3.10 The Floating PML

3.10.1 Introduction

In the previous section we have discussed a modified version of the CPML where the standard Yee equations are applied throughout the entire cell lattice, and the CPML factors are added later. The method of "painting" [35] the solution space with different materials can be applied to this improved CPML formulation, where the PML exists not only on the edges of the solution space, but can be applied within the solution space itself.

Consider the CPML as defined by equations (3.6) and (3.7). Here, additional ψ components can be added to additional cells, if needed, to create the required PML

outside of the edges of the solution space. Since the CPML requires storage of its coefficients only within the PML itself, this additional "Floating PML" does not require a significant increase in resources.

But why do we need this Floating PML? In previous sections we have simulated the microstrip patch antenna by exciting the microstrip line and allowing one side to penetrate into the PML and the other side to reach the radiating patch. The floating PML is useful in freeing the microstrip problem in FDTD from the edges of the solution space, so that

1. A real radiation box can surround the problem space, and
2. A finite-sized ground plane can be constructed and simulated properly

Instead of the Floating PML, Luebbers and Langdon [39] have implemented a resistive source, and Schuster and Luebbers have terminated transmission lines with lumped loads [40] using a recursive convolution technique. Piket-May and Taflove [41] have implemented similar loads, however, their results show that the resistor generates parasitic capacitance at frequencies above 1 GHz. Cryan et al. [38] have implemented lumped elements to terminate transmission lines, where the simulation results are discussed in Section 3.10.3 below.

The advantages of the Floating PML over the Lumped Load or Resistive Source can be summarized as

1. The Floating PML is very wideband because it is based on a very wideband formulation (CPML),
2. The source impedance does not need to be specified for the simulation to run, and
3. No additional parasitic capacitance is added to the circuit.

Some disadvantages of the Floating PML compared to the resistive source are

1. The Floating PML requires more memory, but is not significant compared to the overall CPML,
2. The Floating PML requires more computational time to compute the CPML variables at each time step, but is not significant compared to the total CPML computational time, and
3. The addition of a PEC box may affect some simulations.

3.10.2 Implementation

The Floating PML is formulated as if it were a corner of the CPML box, meaning all three x, y, and z coefficients are calculated and present. The inclusion of all three dimensions for the PML helps to attenuate propagating waves, and maintains stability of the solution space.

Just like a regular CPML box that surrounds the solution space, the Floating PML is surrounded by a PEC box, except has one side open to accept the input signal from the microstrip line, as shown in Figure 3.17. The PEC box helps to attenuate waves that pass through the PML and are reflected back from the PEC walls.

In this implementation of the Floating PML, the grading of the constants must be carefully chosen to maximize the attenuation of propagating waves. The grading chosen for the simulation is the same taper as for the edge PML, except in this PML, the taper is linear, not exponential. In addition, because all three dimensions are included, the Floating CPML coefficients are much smaller than the regular CPML.

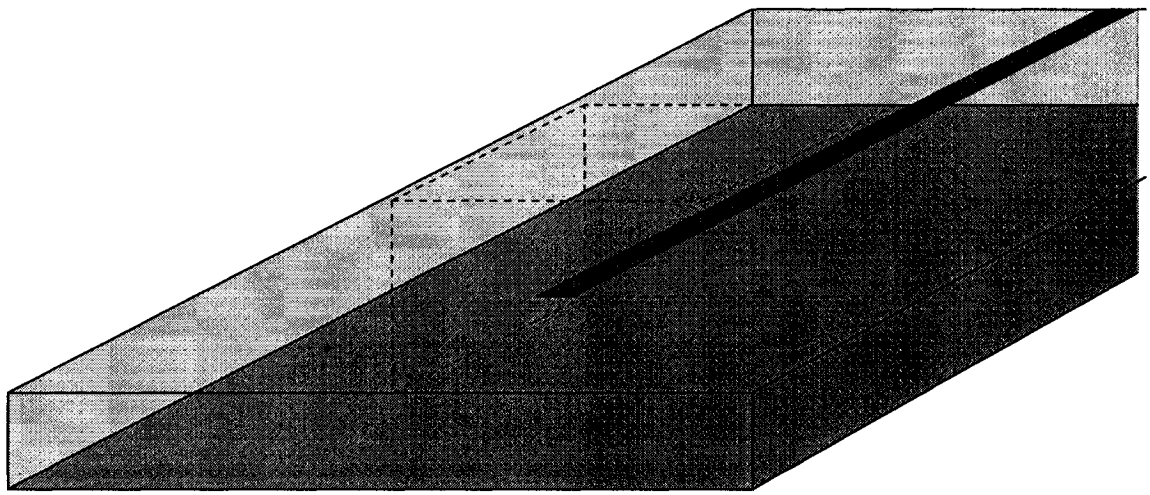

Figure 3.17: Three Dimensional View of Floating PML. The microstrip line ends in the Floating PML, which has been shown with a dotted line.

3.10.3 A Simple Microstrip fed Slot Antenna

The microstrip slot antenna to be studied is shown in Figure 3.18. This problem is particularly problematic for termination of the microstrip line because the impedance match is very narrow, leading to a large reflected pulse with long duration and interaction with the PML. In this example a Floating PML was used to obtain results that were similar to the published results for the antenna pattern [38]. In the published results, the microstrip line is terminated in a lumped element instead of a Floating PML.

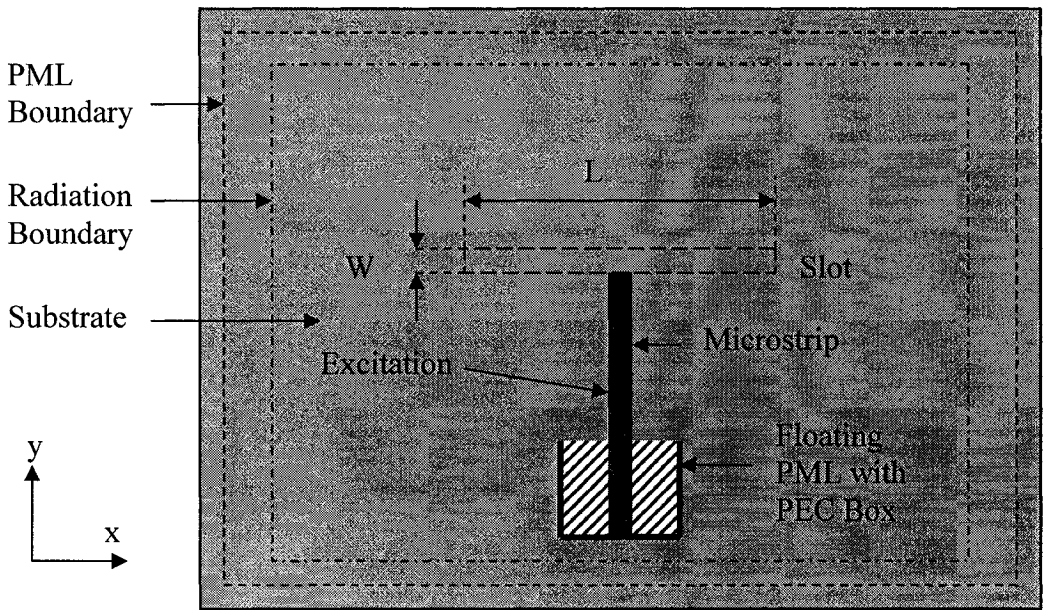

Figure 3.18: Microstrip fed Slot with L = 7.52 mm, W = 0.4 mm. The microstrip line is terminated in a floating PML with a PEC Box open in the +y direction only. The substrate has a dielectric constant of 3.38 and has a thickness of 0.813 mm. The microstrip line has a width of 1.88 mm and terminates at the edge of the slot. [38]

The Floating PML parameters for this problem are given below:

$$\sigma = \sigma^* = 8$$

$$\kappa_e = \kappa_h = 1.1 \qquad (3.30)$$

$$a_e = a_h = 0.05$$

$$M = MA = 1$$

The dimension of the solution space is 50 by 200 by 60, in the x, y and z directions, respectively. The discretization is similar to [38], where dx = 0.31374 mm, dy = 0.1 mm, and dz = 0.20325. In Figure 3.19, the return loss is shown, where the null is at 13 GHz.

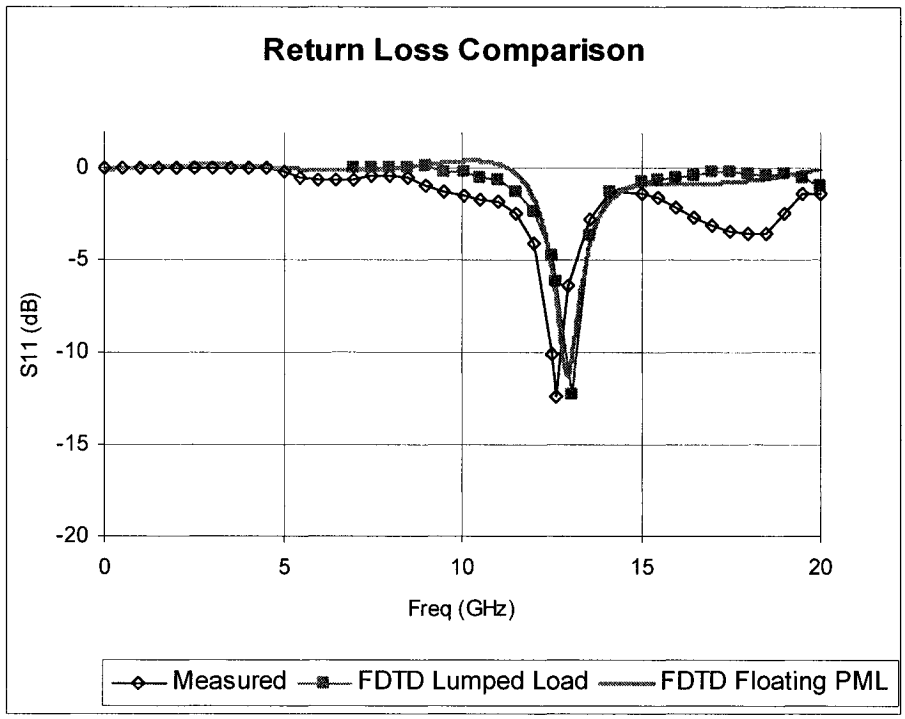

Figure 3.19: Simulated Return Loss for same slot antenna from the same run. See [38] for measured and FDTD Lumped Load data.

The Antenna pattern plotted at 13.0 GHz is given in Figure 3.20. It is shown that the antenna pattern matches the measured data in [38] reasonably well, including the nulls in the antenna pattern as shown in Figure 3.20.

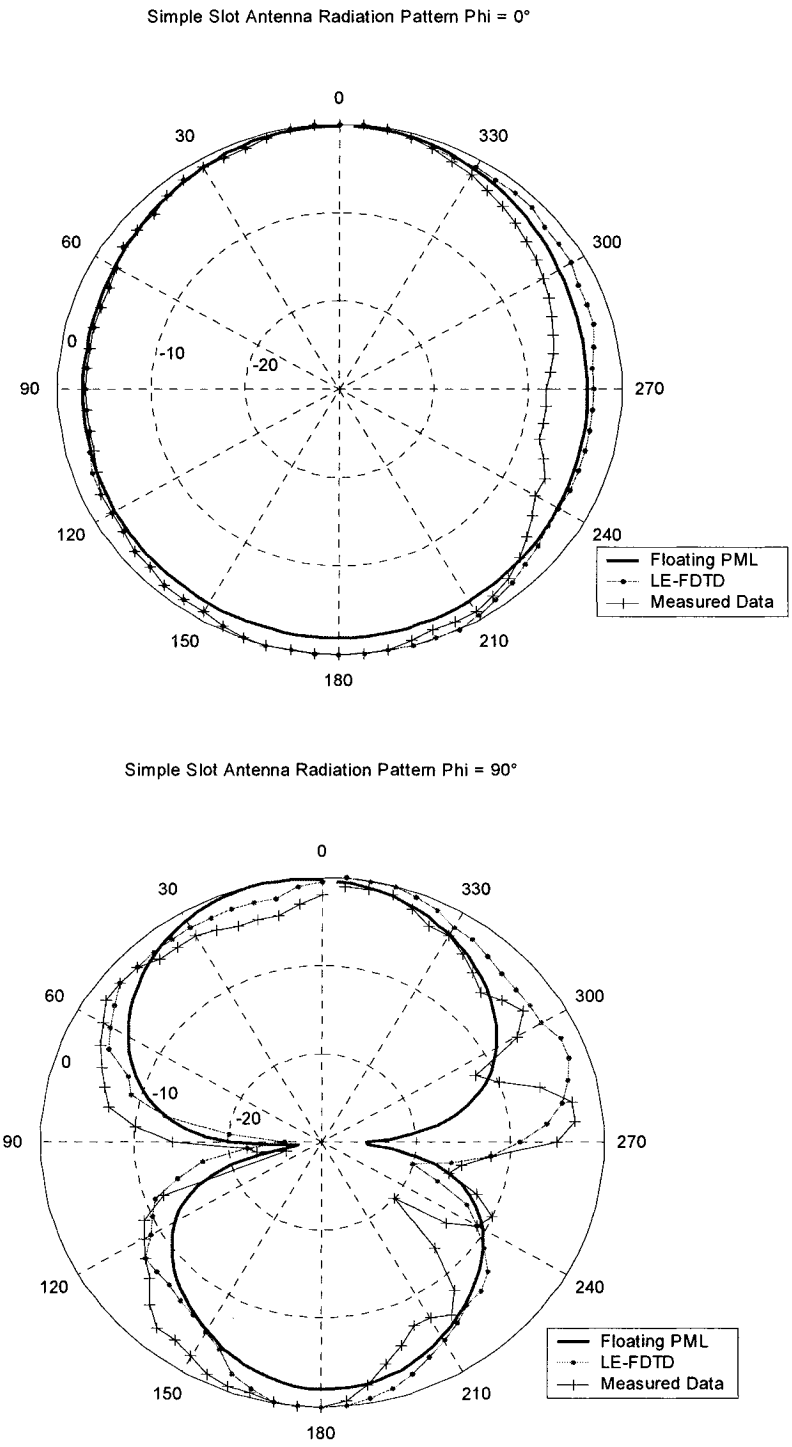

Figure 3.20: Measured [38], LE-FDTD Simulated [38], and Floating PML simulated antenna patterns at 13 GHz for simple Slot Antenna along Phi = 0° (X-Z Plane) and Phi = 90° (Y-Z Plane).

3.11 Summary

Careful implementation of boundary conditions in the developed software for this work is rewarded with consistent accurate results in simulations as shown in the previous sections. It should be noted that some literature uses different conventions than the ones used in this chapter, such as in Sullivan [34], or in software found in popular FDTD websites, such as www.fdtd.org.

The new method of removing κ components from the main FDTD difference equations simplifies programming, decreasing storage requirement / reducing complexity within the main programming space. A possible disadvantage with this method is that there may be an increase in rounding errors due to the additional sum and addition within the PML region, however, no negative effects were found while running simulations.

A new technique for terminating microstrip lines has been discussed, where a Floating CPML has been implemented and tested successfully. The Floating PML provided an easy solution to a simple problem, where existing formulations have been re-used in a novel fashion. This method, however, is still very new and has not yet been tested with a wide variety of structures.

In this chapter, we have only touched the surface of what can be done to optimize and improve the FDTD code. The FDTD code has been successfully verified with simple examples.

Chapter 4: Applications of the FDTD Method to Dual and Broadband Antennas

4.1 Introduction

In this chapter, the CPML FDTD method is used to analyze three dual and broadband antennas. A new dual band antenna is described in Section 4.2, followed by the Hybrid Resonator [28] antenna and the Dual Ring antenna with T-Shaped microstrip feed line [42].

4.2 Dual Band Dual Slot Stripline Omni-Directional Antenna

Recent research work has employed the use of slots in the ground plane of a microstrip structure to achieve broadband operation [24]. Microstrip structures, however, are not vertically symmetrical; therefore rarely produce symmetrical antenna patterns when slots in the ground plane are introduced. A stripline structure with dual slots, however, is vertically symmetrical, therefore inherently produces a symmetrical antenna pattern.

In-house FDTD [36] software is used to analyze the results, using the Convolutional Perfectly Matched Layer (CPML) as first published by Roden and Gedney [16], and described in Appendix A3.

4.2.1 Antenna Geometry

The goal for this design is to produce a uniform antenna pattern similar to that of a half wavelength dipole. The slot in the microstrip ground plane has been studied by Pozar [45]. In this design, a stripline structure instead of microstrip structure is used to ensure symmetry on both the top and bottom of the structure.

The stripline structure consists of two metallic plates separated by dielectric, where the trace (stripline) is placed inside the dielectric as shown in Figure 4.1. The stripline ends between two identical slots which radiate at both 2.45 GHz and 5.8 GHz. Both of these frequency bands were chosen because they are ISM bands which are used for Wireless LAN operation.

The substrate consists of two RT/Duroid 5880 sheets each with 0.062" thickness, or 1.575 mm thick. The dielectric constant is 2.2. The dual slots allow the antenna to radiate on both sides of the structure equally. The dimensions of the slots are both 39 mm by 14 mm, or close to half of a wavelength. The stripline is calculated for 50 Ohms using closed form expressions, and is 2.6 mm wide, and the stub length is 4.3 mm. The mini dipole is 1 mm wide and 5.2 mm long, or between a quarter and an eighth of a wavelength in the dielectric.

For tuning, the slots are adjusted first for their length to resonate at 2.45 GHz, then for their width to resonate at 5.8 GHz. The stub and mini Dipole are then used to tune the resonance at 2.45 GHz and 5.8 GHz and to balance the antenna pattern.

4.2.2 The FDTD Method and In-House software validation

The FDTD software used for this study is based on the full wave time-domain solution of Maxwell's equations similar to that of the work by Sheen et al [36]. After appropriate boundary conditions are set, the structure is excited in the time domain at the input port, and the reflected wave is analyzed using Fourier transformation methods. The CPML is an improved absorbing boundary condition that is memory efficient and allows the analysis of resonant structures.

The stripline is excited on both sides of the trace, as shown in Figure 4.2. The pulse travels in both directions, where on one side the pulse is absorbed by the PML and the pulse continues to travel on the other side.

To validate the in-house FDTD software, the structure was simulated using Ansoft Designer, a Method of Moments software package [43]. The results matched reasonably well, as can be seen in Figure 4.3. The resonant frequencies of 2.45 GHz and 5.8 GHz can clearly be seen in the results. The in-house software, however, predicted a resonant frequency of 2.41 GHz instead of 2.45 GHz, an error of less than 2%.

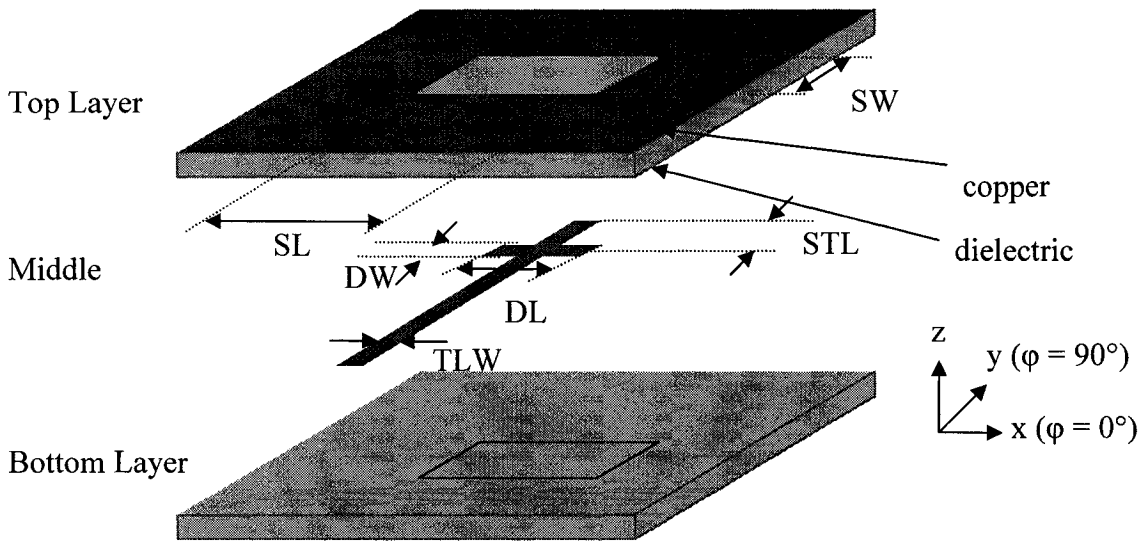

Figure 4.1: Three dimensional view of stripline antenna using double slots. The top layer is a mirror image of the bottom layer. Final dimensions are Slot Width (SW) = 14.0 mm, Slot Length (SL) = 39.0 mm, Stub Length (STL) = 4.3 mm, Dipole Length (DL)= 5.2 mm, Dipole Width (DW) = 1.0 mm, Stripline Width (TLW) = 2.6 mm. In the simulation, an infinite ground plane is assumed. Each dielectric layer is 1.575 mm thick and has a dielectric constant of 2.2.

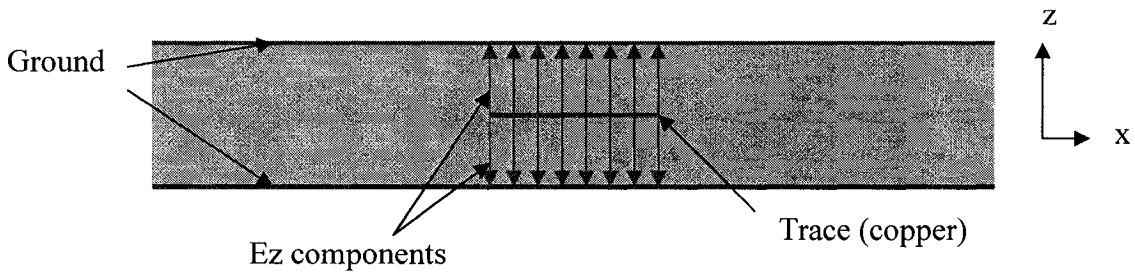

Figure 4.2: Excitation of stripline transmission line

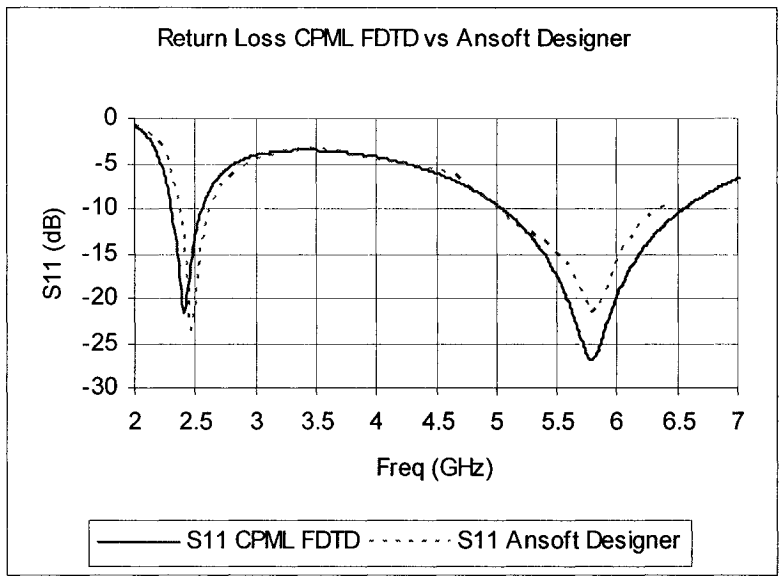

Figure 4.3: Comparison of Return Loss from 2 GHz to 6.5 GHz for CPML FDTD and Ansoft Designer

Dimension	**Discretization size, mm**
Δx	0.325
Δy	0.250
Δz	0.315

Table 4.1: Discretization of solution space

The discretization for this simulation is given in Table 4.1. Table 4.2 outlines the exact dimensions used for the FDTD simulation. Note that the stub length is 0.05 mm different in the FDTD simulation as compared to Ansoft Designer.

Dimension	Size (cells)	Physical Size (mm)	Description
W	8	2.6	Width of transmission line
SL	17	4.25	Stub length
WT	56	14	Width of slot
LT	60	19.5	Half of length of slot
h1	5	1.575	Height of substrate
D1	16	5.2	Length of dipole
Dw	4	1.0	Width of dipole

Table 4.2: Dimensions of problem in discrete coordinate sizes.

4.2.3 Parametric Study: Slot Length And Width Variation

The effects of varying the slot length and width on return loss (S11) are shown in Figures 4.4 to 4.7. In Figure 4.4, it is shown that an increase in the slot length decreases the resonant frequencies of the slot at both 5.8 GHz and 2.45 GHz. Figures 4.5 and 4.6 show a finer scale for various dimensions so that this effect is more easily viewed.

Figure 4.7 shows that changes in the slot width change the resonant frequency at 5.8 GHz, but do not affect the resonant frequency at 2.45 GHz significantly. This allows for tuning of the second resonant frequency after the first resonant frequency is tuned by varying slot length.

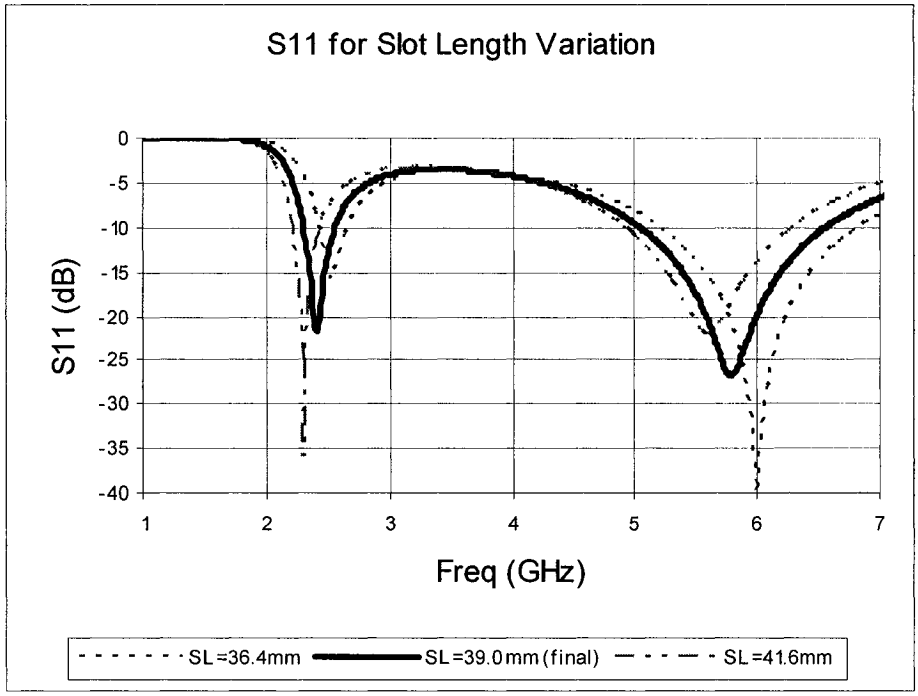

Figure 4.4: Effect of Slot Length (SL) Variation from 1 to 7 GHz.

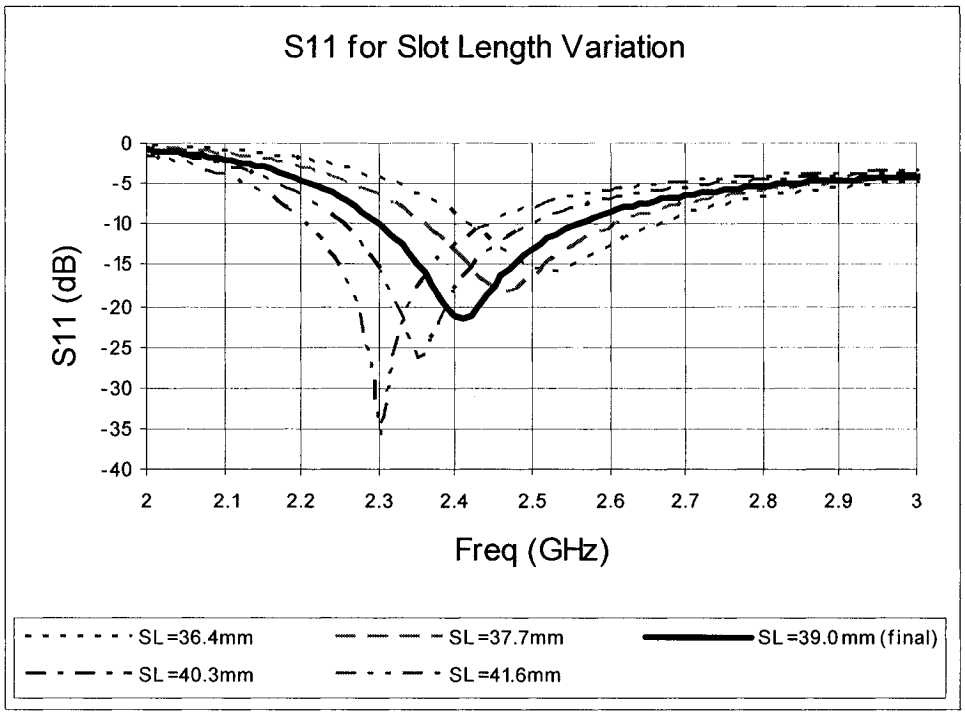

Figure 4.5: Effect of Slot Length (SL) Variation from 2 to 3 GHz.

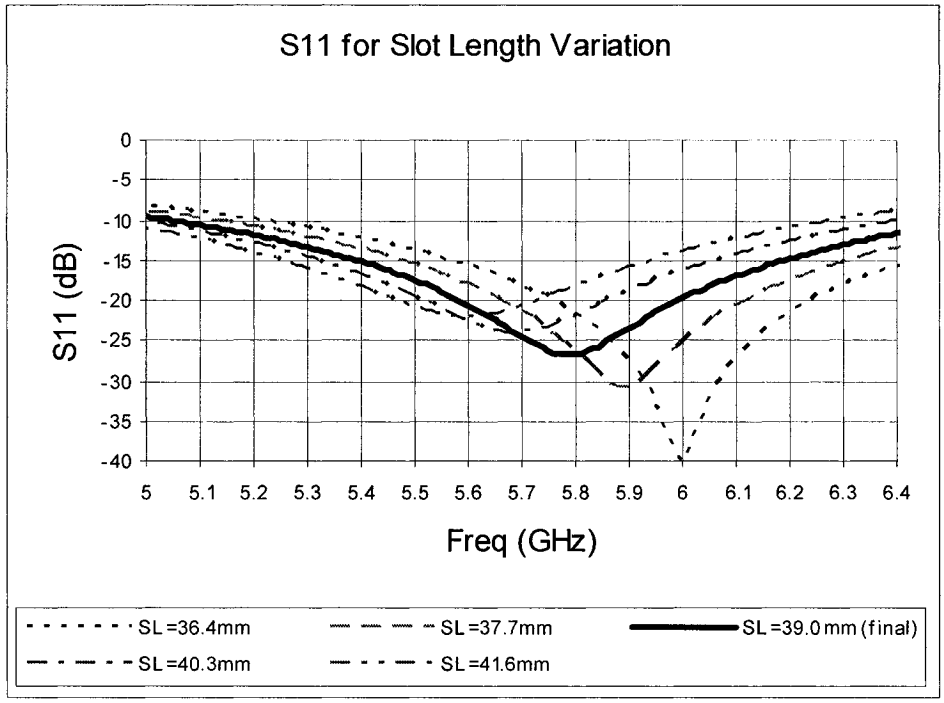

Figure 4.6: Effect of Slot Length (SL) Variation from 5 to 6.4 GHz.

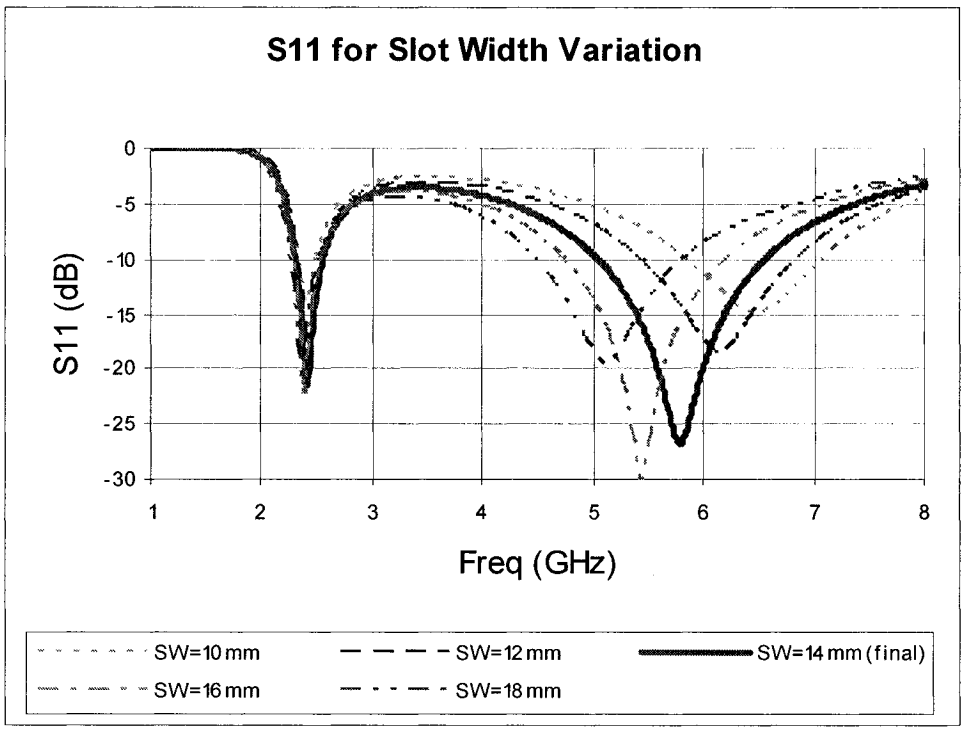

Figure 4.7: Effect of Slot Width (SW) Variation from 1 to 8 GHz.

In Figures 4.4 to 4.7, the return loss shows a 10 dB bandwidth extending from 5 GHz to approximately 6.4 GHz, or 25% bandwidth. At 2.45 GHz, the 10 dB bandwidth extends from 2.35 to 2.6 GHz, or approximately 10%.

4.2.4 Antenna Patterns

To investigate the radiation pattern characteristics of the proposed structure, the Floating PML is used as discussed in Section 3.10. Figures (4.8) and (4.9) show the omni-directional antenna patterns at 2.45 and 5.8 GHz, respectively. The peak gain achieved at 2.45 GHz and 5.8 GHz are 2.1 dBi and 3.1 dBi, respectively.

It is shown that the slots radiate as a horizontal dipole and are virtually symmetrical. The stripline structure with symmetrical slots therefore is capable of generating symmetrical antenna patterns.

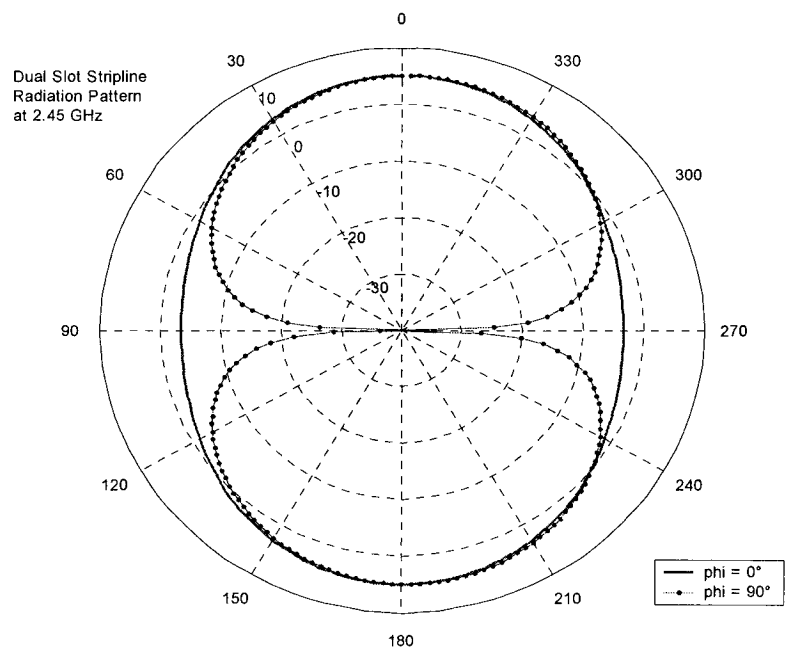

Figure 4.8:Antenna Pattern at 2.45 GHz. Peak Gain is 5.1 dBi

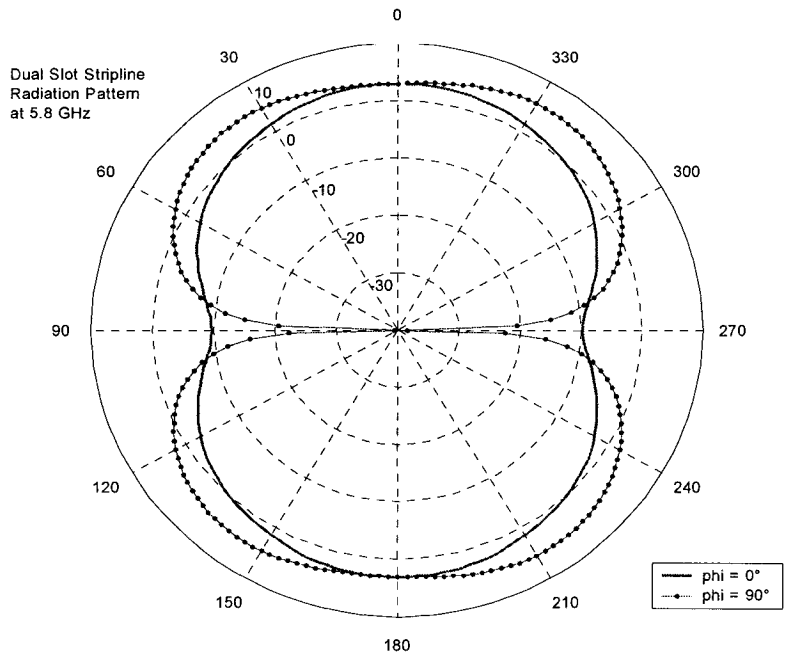

Figure 4.9: Antenna Pattern at 5.8 GHz. Peak Gain is 5.6 dBi.

The stripline antenna with dual slots provides an almost symmetric antenna pattern. The design studied in this paper showed a reasonable 10 dB bandwidth of 25% at 5.8 GHz and of 10% at 2.45 GHz. Varying the slot length varied the resonant frequencies at 2.45 and 5.8 GHz, while varying the slot width varied the resonant frequency primarily at 5.8 GHz.

The FDTD software provided reasonable results for return loss compared with commercial software. It has also proven useful in performing batch runs, where runs with different dimensions can be executed sequentially.

A stripline structure was used to substitute for a microstrip structure where a symmetrical pattern was needed and overall thickness of the structure was not critical. For further study, this type of structure may be applied to other microstrip slot structures.

4.3 Hybrid (Dielectric) Resonator Antenna

The CPML is able to handle structures that have a highly resonant nature, such as the Dielectric Resonator Antenna (DRA). One such dual band structure is the Hybrid Resonator Antenna as studied by Rao, Denidni, and Sebak [28]. This structure has resonant frequencies at 1.9 GHz, the cellular PCS band, and at 2.45 GHz, the ISM band. A slightly modified structure is shown below in Figure 4.10, where there is no metallic disc at the top of the dielectric disc, and a microstrip is used for feeding the DRA instead of a slot.

The dimensions are h1 = 0.813 mm where the substrate has e_r1 = 3.38, W = 1.9 mm, t1 = 4 mm, h2 = 10.5 mm where the dielectric disc has e_r2 = 35.5, R = 15.0 mm, L = 29.0 mm. The microstrip is excited in the same way as for Sheen's microstrip patch in the Section 3.8.

Refering to Figure 4.10, the discretization of the solution space using dimensions described above is as shown in Table 4.3 and Table 4.4.

Dimension	**Discretization size, mm**
Δx	0.188244
Δy	0.188244
Δz	0.1626

Table 4.3: Discretization of solution space

Dimension	Size (cells)	Physical Size (mm)	Description
L	154	29	Length of T section
W	10	1.88244	Width of TL and T section
R	80	15	Radius of disc
h2	65	10.5	Height of disc
T	21	4	Offset of top of t-section from center
h1	6	0.813	Height of substrate

Table 4.4: Dimensions of problem in discrete coordinate sizes.

The results in Figure 4.11 show that the resonant frequencies are almost identical between HFSS [46], a commercial software package, and the CPML FDTD simulation.

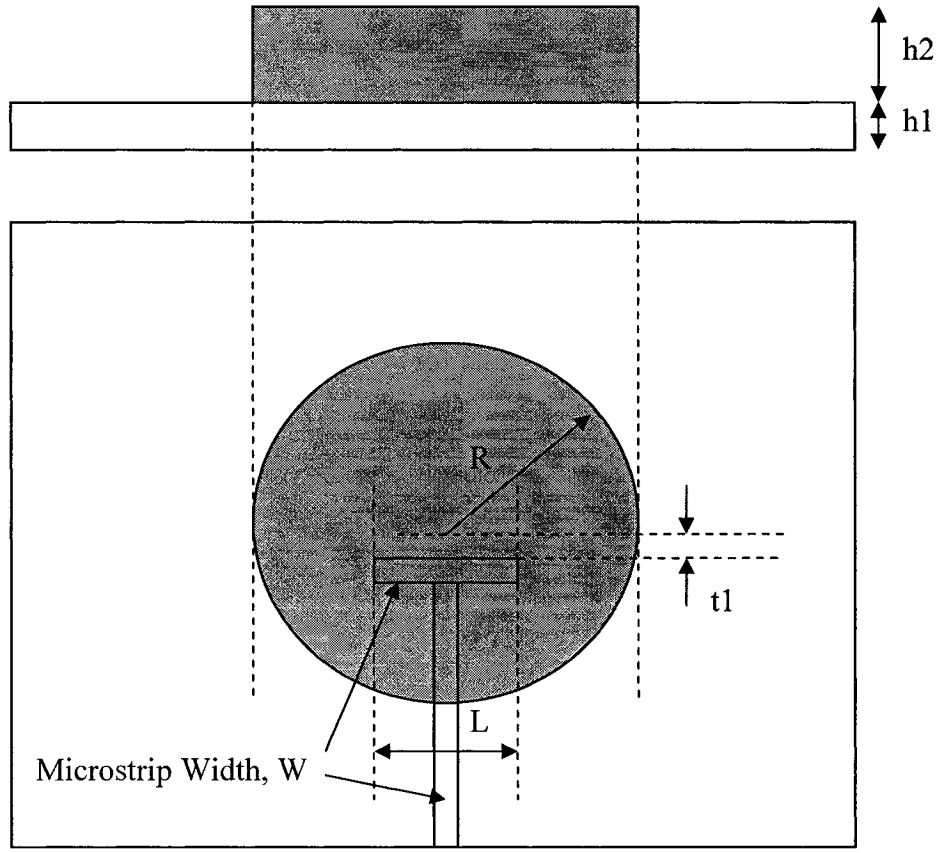

Figure 4.10: Hybrid Resonator Antenna as studied by Rao, Denidni, and Sebak [28]. Dimensions are h1 = 0.813 mm where the substrate has e_r1 = 3.38, W = 1.9 mm, t1 = 4 mm, h2 = 10.5 mm where the dielectric disc has e_r2 = 35.5, R = 15.0 mm, L = 29.0 mm.

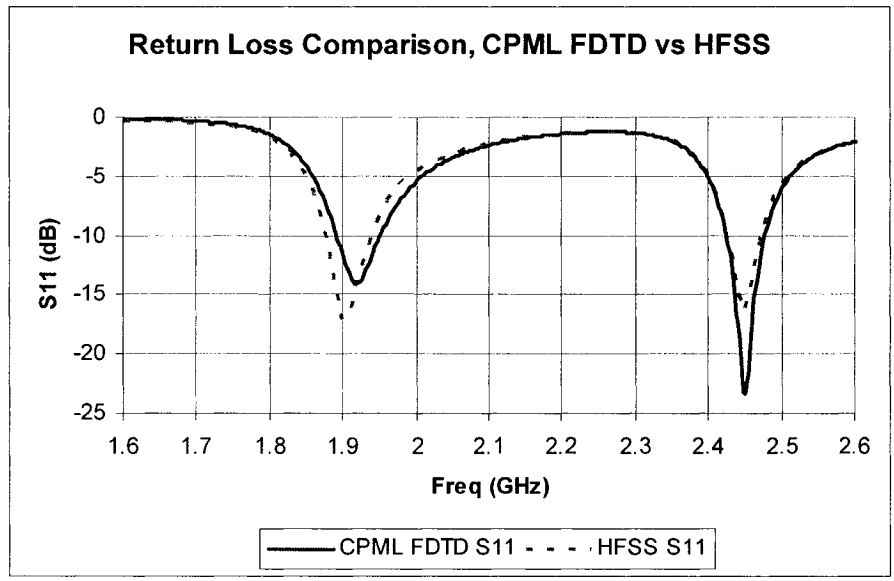

Figure 4.11: Comparison of CPML FDTD vs HFSS for Hybrid Resonator Antenna [28]

4.4 Dual Ring Slot Antenna with T-Shaped Microstrip Feed Line

Denidni, Rao, and Sebak have studied a broadband dual ring slot antenna using the Method of Moments, where two rings are cut into the ground plane of a one-sided dielectric substrate [42]. Attenuation in the late time is important for this simulation because the ring structure is highly resonant. In fact, a simple split-field PML as explained in Appendix A3 may yield incorrect data in the late time, causing the FDTD results to become corrupt and inaccurate.

4.4.1 Problem Setup

The microstrip circuit was modeled as an infinitesimally thin metal strip on top of a dielectric layer with permittivity 2.2 and no loss. The substrate was placed in the x-y plane in the middle of the computational region. The ring slots were "cut" in the ground plane, which is also infinitesimally thin.

The source was generated by exciting an electric field under the microstrip line adjacent to the PML. One side of the propagating wave was dissipated in the PML, while the other traveled along the transmission line. The S11 parameter was computed by monitoring the z-directed electric field one cell under the microstrip line, eight cells from the source.

The simulation was run for 5000 time steps for the coarse grid and 10000 points for the fine grid, where 0.9 times the Courant limit was used. The input was taken as the first few points (330 for the coarse grid or 460 for the fine grid), and the output was taken as the rest of the points.

The DFT was then performed by taking the DFT of the input and the DFT of the output, then dividing the output by the input. The results are presented in logarithmic form. The DFT was computed with custom software which outputs 1000 frequency points between 0 and 20 GHz.

The grid step sizes are given in Tables 4.5 and 4.6 below:

Dimension	**Discretization size, mm**
Δx	0.5
Δy	0.5
Δz	0.3925

Table 4.5: Coarse Discretization of solution space, time step 7.88625 x 10^{-13}s, grid size 100 x 140 x 60

Dimension	**Discretization size, mm**
Δx	0.25
Δy	0.25
Δz	0.19625

Table 4.6: Fine Discretization of solution space, time step 3.94313 x 10^{-13}s, grid size 180 x 240 x 70

The dimensions for coarse runs are given in Table 4.7, while the dimensions for fine runs in cells units are given in Table 4.8:

Dimension	Size (cells)	Physical Size (mm)	Description
R1	14	7	Ring 1 radius
R2	22	11	Ring 2 radius
D1	4	2	Center of ring 1, d1 from center
D2	13	6.5	Distance from center to start of T section
Lt	24	12	Length of T section
Wt	4	2	Width of T section
t1	2	1	Thickness of ring 1
t2	2	1	Thickness of ring 2
Ls			Length of transmission line (defined by size of problem space)
Ws	10	5	Width of transmission line
Tsub	4	1.57	Substrate thickness

Table 4.7: Coarse Dimensions of problem in discrete coordinate sizes.

Dimension	**Size (cells)**	**Physical Size (mm)**	**Description**
R1	28	7	Ring 1 radius
R2	44	11	Ring 2 radius
D1	8	2	Center of ring 1, d1 from center
D2	26	6.5	Distance from center to start of T section
Lt	48	12	Length of T section
Wt	8	2	Width of T section
t1	4	1	Thickness of ring 1
t2	4	1	Thickness of ring 2
Ls			Length of transmission line (defined by size of problem space)
Ws	20	5	Width of transmission line
Tsub	8	1.57	Substrate thickness

Table 4.8: Fine Dimensions of problem in discrete coordinate sizes.

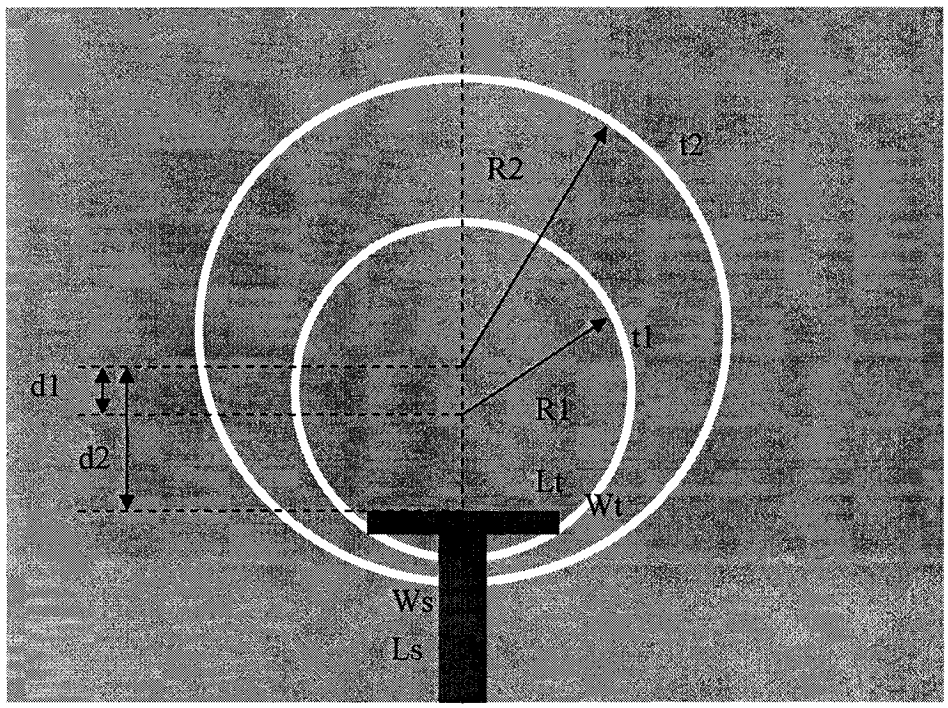

Figure 4.12: Layout of dual ring slots with T-shaped microstrip feed line. [42]

In Figure 4.12, Lt and Wt are the length and width of the T-shaped part of the feed line, respectively. Ls and Ws are the length and width of the feedline, respectively. The width of the slots are t1 for ring 1, and t2 for ring 2. The radius for ring 1 is R1, measured from its center to the inner portion of the ring. Similarly, the radius for ring 2 is R2, measured from its center to the inner portion of the ring. d1 and d1 mark the distances from the top of the T-shape to the centers of rings 1 and 2, respectively.

4.4.2 Results

To verify for convergence, the simulation was run with two different grid settings: coarse and fine. The results are very similar as can be seen in Figure 4.13 below.

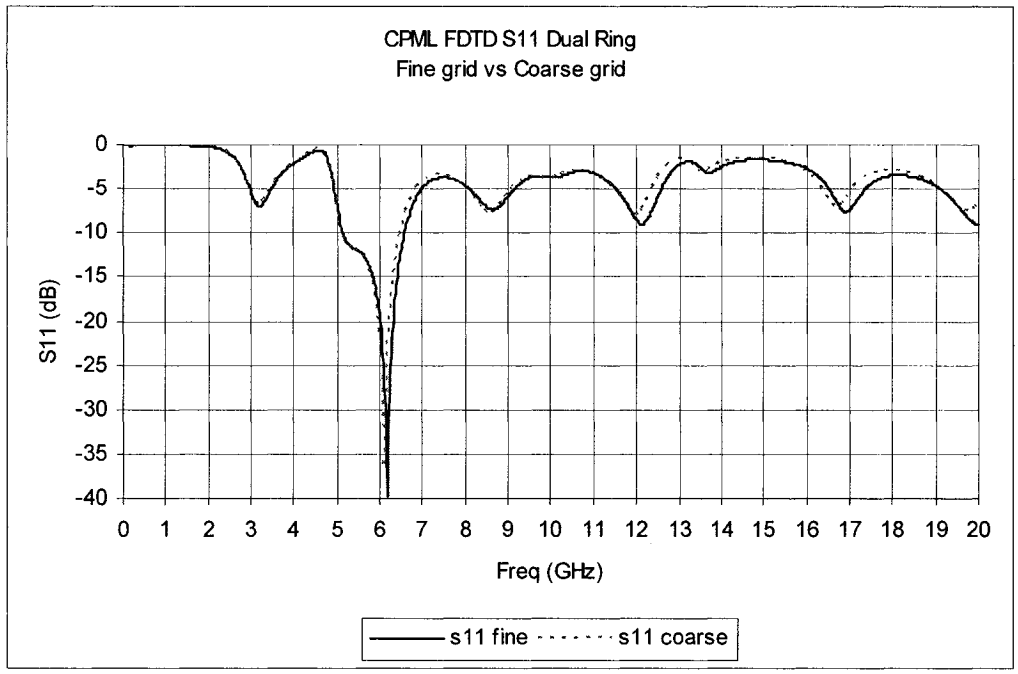

Figure 4.13: Dual Ring Slot fed by T-Shaped microstrip feed line: Comparison of fine grid vs coarse grid to test for convergence.

Next, the structure was simulated using Ansoft's HFSS and HP's ADS Momentum software. All results appear to have similar results for the 5dB and 10dB points (within 2 to 3%), however, again the depth of the resonance frequencies is different. The resonance frequencies are 6.1, 6.25, 6.16 GHz, for HFSS, ADS, and the FDTD simulation, respectively. In this simulation the null is actually deeper than ADS or HFSS. The comparison is show in Figure 4.14 below:

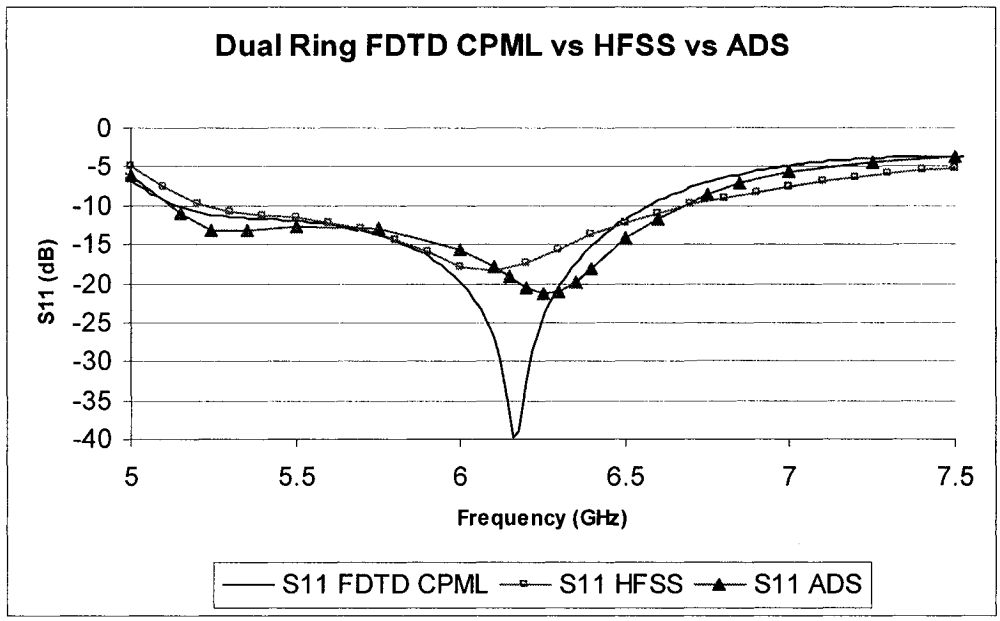

Figure 4.14: Dual Ring Slot fed by T-Shaped microstrip feed line: FDTD with CPML vs HFSS vs ADS.

In figure 4.15, the simulation is shown from 3 to 7.5 GHz, where ADS was run from 3 to 7.5 GHz.

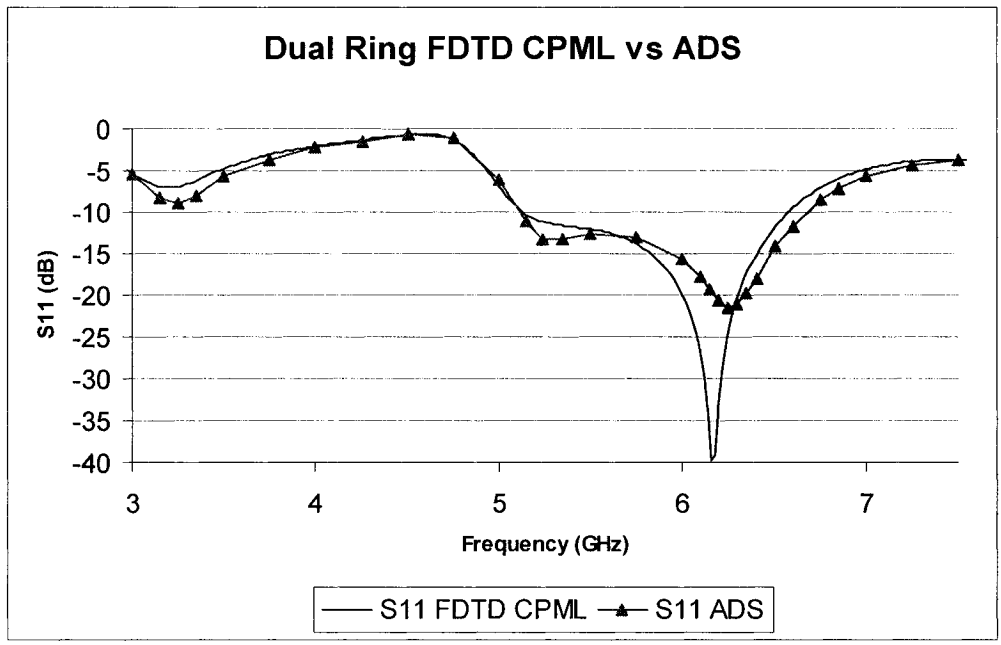

Figure 4.15: Dual Ring Slot fed by T-Shaped microstrip feed line: FDTD with CPML vs ADS.

As can be seen by the simulations, the results are very similar for the three methods (HFSS: FEM, ADS: Method of Moments, and FDTD with CPML). The run time for each simulation is also, coincidentally, very similar. The HFSS simulation took approximately one hour (8 passes, adaptive mesh), while the ADS simulation was about 45 minutes (3 to 7.5 GHz, adaptive sweep) running on the Concordia University research server. The FDTD simulation took about 1 hour for the coarse grid, and 3 to 4 hours for the fine grid (where fine and coarse grids has similar results) running on a 1.7 GHz Centrino laptop. The FDTD simulation has the advantage that a very wide bandwidth (0 to 20 GHz) was computed all at once.

4.5 Summary

The FDTD implementation using the CPML is a highly effective means of simulating antennas. A stripline structure with dual slots was investigated with the goal of creating a dual band, symmetrical omni-directional antenna. The results compared well with those based on commercial software. One dual-band configuration provided a reasonable 10 dB bandwidth of 25% at 5.8 GHz and 10% at 2.45 GHz. The effect of different design parameters on the resonant frequencies and bandwidth was discussed.

The Hybrid Resonator Antenna provided a very good match to commercial software for the return loss. It was shown that structures with high dielectric constants (35.5) and long interactions with the PML can be modeled correctly.

The simulation for return loss of the Dual Ring Slot with T-Shaped microstrip feed line sufficiently matched ADS and HFSS, however, did not match experimental data

or simulation data in [42] as closely. The differences appear to be due to interpretation of the geometrical structure and its implementation since the CPML FDTD simulation matched ADS and HFSS more closely except for the depth of the nulls. It is cautioned that the resonant frequencies appear slightly lower than the frequencies in real simulations. There is an expected difference in frequency due to dispersion as can be expected with FDTD, however, the error appears to be slightly more than what was expected, but still within 1 to 3%. In addition, the thickness of the ring is very small compared to the overall structure. Because this FDTD approach uses a regular mesh, the number of cells that represent the air gap within the ring is small (4 cells), therefore leading to staircasing and quantization errors.

Chapter 5: Conclusions and Future Work

5.1 Conclusions

In this thesis, the FDTD method using the CPML as a robust computational tool is used to simulate several structures that have high dielectric constants and long term interactions with PML walls. Different antenna structures have been simulated and S11 parameters match well when compared with commercial software results.

In chapter 2, a literature review has discussed some of what is currently being researched with the FDTD method, however, it was found that this method is still in a state of rapid evolution. Different methods of designing wideband antennas relevant to this thesis have been discussed in Section 2.2, and some limitations to their uses have been discussed as well.

In chapter 3, a new method of removing κ components from the main FDTD difference equations has shown that it is possible to simplify the programming, decrease storage requirement / reduce complexity within the main programming space by simply re-arranging the CPML equations. In addition, we briefly discussed what can be done to optimize the running speed of FDTD code using an object-oriented approach. We then introduced the Floating PML, a novel use of the existing CPML formulation that allows for termination of microstrip lines within the solution space.

A stripline structure with dual slots was investigated with the goal of creating a dual band, symmetrical omni-directional antenna. The results compared well with those based on commercial software. One dual-band configuration provided a reasonable 10

dB bandwidth of 25% at 5.8 GHz and 10% at 2.45 GHz. The effect of different design parameters on the resonant frequencies and bandwidth was discussed.

The Hybrid Resonator Antenna also provided a very good match to commercial software for the return loss. It was shown that structures with high dielectric constants (35.5) and long interactions with the PML can be modeled correctly.

The simulation of the Dual Ring Slot with T-Shaped microstrip feed line sufficiently matched ADS and HFSS, where the error for the resonant frequency appears to be slightly more than what was expected, but still within 1 to 3%. In addition, the thickness of the ring is very small compared to the overall structure and because this FDTD approach uses a regular mesh, the number of cells that represent the air gap within the ring is small (4 cells), therefore leading to staircasing and quantization errors.

Careful implementation of boundary conditions in this thesis has been rewarded with consistent results in simulations. A new dual band dual slot stripline antenna has been introduced in Chapter 4, and more structures from literature have been implemented in FDTD.

5.2 Future Work

5.2.1 Topics for further study in FDTD

The FDTD method is in a constant state of evolution and it is clear that some areas can be improved. The rectangular staircasing approximation, for example, may require very fine resolutions for certain structures that would require considerable resources. Conformal FDTD methods today use many different schemes to solve this

problem, however, work in this area continues and improved methods continue to be published.

The solutions that exist for combating dispersion may be improved as well. One recent method discussed, the NA method [8], can correct anisotropy at one frequency range only, while another method discussed, the PSTD method [10], is subject to Gibb's phenomenon [1]. Currently, research continues with the goal of achieving a solution for correcting anisotropy and dispersion for the whole solution space at all frequencies.

5.2.2 Topics for Further Study with Dual and Wideband Antennas

New antenna designs will always be required. New wireless electronic devices are constructed at an alarming rate, where each new device will require a new antenna. Additionally, crowding of current available bandwidth requires the design of new devices at higher frequency bands, requiring the design of antennas at different frequencies and with wideband results.

The stripline structure studied in this thesis was successfully used to provide a symmetrical pattern where a microstrip structure did not provide a perfectly symmetric pattern. Different slot shapes can be studied in the future, where wide band instead of dual band is the design goal. It is possible, as well, to study stripline structures where only one side has a slot. Stripline structures have the advantange that slots in the structure are the only radiating sources, so that a stub tuning may be performed outside the radiating source, unlike microstrip structures.

Dielectric antenna structures also have potential for very wide bandwidths. The CPML FDTD method is robust enough to simulate dielectric structures that have a very

long interaction with the walls. In the future, this method can be used to design and optimize new miniature dielectric antenna structures.

Finally, slot antennas have great potentials for dual and wideband structures, as shown in the Literature Review in Chapter 2 and with the new dual band dual slot antenna in Chapter 4. The co-planar waveguide fed design has been used in literature for very wideband design.

References

[1] A. Taflove, Susan C. Hagness, *Computational Electrodynamics The Finite-Difference Time-Domain Method, Third Edition.* Artech House, 2005.

[2] C. A. Balanis, *Advanced Electromagnetics.* John Wiley & Sons, 1989.

[3] Yee, K.S., "Numerical solution of initial boundary value problems involving Maxwell's equations in isotropic media." *IEEE Trans. Antennas and Propagation*, Vol. 14, pages 302-307, 1966.

[4] G. D. Smith, *Numerical Solution of Partial Differential Equations.* Oxford, U.K.: Oxford Univ. Press, 1965.

[5] Takefumi Namiki. "A New FDTD Algorithm Based on Alternating-Direction Implicit Method" *IEEE Transactions On Microwave Theory And Techniques*, Vol. 47, No. 10, page 2003, October 1999.

[6] Zheng, Fenghua; Zhizhang Chen; Jiazong Zhang. "A Finite-Difference Time-Domain Method Without the Courant Stability Conditions", *IEEE Microwave And Guided Wave Letters*, Vol. 9, No. 11, page 441, November 1999.

[7] Sun, G.; Trueman, C.W.; "Unconditionally-stable FDTD method based on Crank-Nicolson scheme for solving three-dimensional Maxwell equations" *Electronics Letters* Volume 40, Issue 10, pages 589 – 590, 13 May 2004.

[8] Guilin Sun; Trueman, C.W., "Suppression of numerical anisotropy and dispersion with optimized finite-difference time-domain methods," *IEEE Transactions on Antennas and Propagation*, Vol. 53, Issue 12, pages 4121 – 4128, Dec. 2005.

[9] G. Sun, "Development and Evaluation of Novel Finite-Difference Time-Domain Methods for Solving Maxwell's Equations," Ph.D. dissertation, Concordia Univ., Montreal, Canada, Nov. 2004.

[10] Zhao, Gang; Zeng, Yan Qing; Liu, Qing H. "The 3-D Multidomain Pseudospectral Time-Domain Method for Wideband Simulation" *IEEE Microwave And Wireless Components Letters*, Vol. 13, No. 5, pages 184-186, May 2003.

[11] Zhao, Gang; Liu, Q.H., "The unconditionally stable pseudospectral time-domain (PSTD) method" *Microwave and Wireless Components Letters*, IEEE, Volume 13, Issue 11, pages 475 – 477, Nov. 2003.

[12] Holland, R., and J. Williams, "Total-field versus scattered-field finite-difference," *IEEE Trans. Nuclear Science*, Vol.30, pages 4583-4587, 1983.

[13] Berenger, J.P., "A perfectly matched layer for the absorption of electromagnetic waves," *J. Computational Physics*, Vol. 114, pages 185-200, 1994.

[14] Gedney, S. D., "An anisotropic PML absorbing media for FDTD simulation of fields in lossy dispersive media," *Electromagnetics*, Vol. 16, pp. 399-415, 1996.

[15] Berenger, J.P., "Numerical reflection of evanescent waves from perfectly matched layers," *Proc. IEEE Antennas Propagat. Soc. Intl. Symp.*, Vol. 114, pages 185-200, 1994.

[16] Roden, J.A., and S.D. Gedney, "Convolutional PML (CPML): An efficient FDTD implementation of the CFS-PML for arbitrary media," *Microwave Optical Tech. Lett.*, Vol. 27, pages 334-339, 2000.

[17] Holland, R., "Finite-difference solution of Maxwell's equations in generalized nonorthogonal coordinates," *IEEE Trans. Nuclear Science*, Vol. 30, pages 4589-4591, 1983.

[18] Nehrbass, J.W., R. Lee, "Optimal finite-difference sub-gridding techniques applied to the Helmholtz equation," *IEEE Trans. Microwave Theory Tech.*, Vol. 48., pages 976-984, 2000.

[19] White, M.J., Z. Yun, and M.F. Iskander, "A new 3D FDTD multigrid technique with dielectric traverse capabilities," *IEEE Trans Microwave Theory Tech.*, Vol. 49, pages 422-430, 2001.

[20] Jiang, B.N., *The Least Squares Finite Element Method*, Berlin: Springer-Verlag, 1998.

[21] Bossavit, A., "Whitney forms: A class of finite elements for three-dimensional computations in electromagnetism," *IEEE Proc.*, Vol. 135, pages 493-500, 1988.

[22] Riley, D. J., C.D. Turner, "VOLMAX: A solid-model based, transient volumetric Maxwell solver using hybrid grids," *IEEE Trans. Antennas Propagat. Mag.*, Vol. 39, pages 20-33, 1997.

[23] http://www.semcad.com Semcad-X software, Schmid & Partner Engineering AG, Zeughausstrasse 43, 8004 Zurich, Switzerland. Accessed on 1 March, 2006.

[24] Chair, R.; A. A. Kishk; K. F. Lee. "Ultrawide-band Coplanar Waveguide-Fed Rectangular Slot Antenna", *IEEE Antennas And Wireless Propagation Letters*, Vol. 3, Issue 1, pages 227-229, 2004.

[25] Buerkle, A.; Sarabandi, K.; Mosallaei, H.; "A novel approach to enhance the bandwidth of miniaturized dielectric resonator antennas" *IEEE 2004 Antennas and Propagation Society International Symposium.* Volume 2, pages 1359 – 1362, 20-25 June 2004.

[26] Chen, Shih-Yuan;Powen Hsu, "Broad-Band Radial Slot Antenna Fed by Coplanar Waveguide for Dual-Frequency Operation", *IEEE Transactions On Antennas And Propagation*, Vol. 53, No. 11, pages 3448 – 3452, November 2005.

[27] Yeo, J.; Mittra, R.; "Design of a wideband antenna package with a compact spatial notch filter for wireless applications," *IEEE 2002 Antennas and Propagation Society International Symposium*, pages 492 – 495, 16-21 June 2002.

[28] Qinjiang Rao, Tayeb A. Denidni, Abdel R. Sebak, "A Hybrid Resonator Antenna Suitable for Wireless Communication Applications at 1.9 and 2.45 GHz," *IEEE Antennas And Wireless Propagation Letters*, Vol. 4, p. 341, 2005.

[29] Tong , Kin-Fai; Kwai-Man Luk; Kai-Fong Lee; Richard Q. Lee. "A Broad-Band U-Slot Rectangular Patch Antenna on a Microwave Substrate" *IEEE Transactions On Antennas And Propagation*, Vol. 48, No. 6, pages 954 – 960, June 2000.

[30] Chiu, Chi Yuk; Kam Man Shum; Chi Hou Chan; Kwai Man Luk. "Bandwidth Enhancement Technique for Quarter-Wave Patch Antennas," *IEEE Antennas and Wireless Propagation Letters*, Vol. 2, pages 130 – 132, 2003.

[31] Tiehong, Tian; Zhou Zheng; "A novel multiband antenna: fractal antenna," *International Conference on Communication Technology Proceedings 2003 (ICCT 2003)*. Volume 2, pages 1907 – 1910, 9-11 April 2003.

[32] Lule, E.; Babij, T.; "Koch island fractal ultra wideband dipole antenna" *IEEE Antennas and Propagation Society International Symposium*, Volume 3, pages 2516 – 2519, 20-25 June 2004.

[33] Behdad, N.; Sarabandi, K.; "A compact ultra-wideband antenna for time- and frequency-domain applications" *2005 IEEE Antennas and Propagation Society International Symposium*, vol. 2B, pages 552 – 555, 3-8 July 2005.

[34] D. M. Sullivan, *Electromagnetic Simulation Using the FDTD Method.* IEEE Press, New York: 2000.

[35] Kunz, Karl S., R. J. Luebbers. *The Finite Difference Time Domain Method for Electromagnetics*. CRC Press, Boca Raton, 1993.

[36] D. M. Sheen, S. M. Ali, M. D. Abouzahra, J. A. Kong, "Application of the three-dimensional finite-difference time-domain method to the analysis of planar microstrip circuits", *IEEE Trans. Microwave Theory Tech.*, Vol. 38, No. 7, pages 849–857, July 1990.

[37] C. A. Balanis, *Antenna Theory: Analysis and Design, Second Edition.* John Wiley & Sons, 1982.

[38] Cryan, M.; Helbing, S.; Alimenti, F.; Mezzanotte, P.; Roselli, L.; Sorrentino, R.; "Analysis and design of quasi-optical multipliers using lumped element (LE)-FDTD method" *IEEE Antennas and Propagation Society International Symposium*, Volume 1. Pages 100 -103, 11-16 July 1999.

[39] Luebbers, R.J.; Langdon, H.S., "A simple feed model that reduces time steps needed for FDTD antenna and microstrip calculations" *IEEE Transactions on Antennas and Propagation*, Volume 44, Issue 7, pages 1000 – 1005, July 1996.

[40] Schuster, J.W.; Luebbers, R.J.; Livernois, T.G., "Application of the recursive convolution technique to modeling lumped circuit elements in FDTD simulations," *IEEE Antennas and Propagation Society International Symposium.*

Volume 4, Page(s):1792 – 1795, 21-26 June 1998.

[41] Piket-May, M.; Taflove, A.; Baron, J., "FD-TD modeling of digital signal propagation in 3-D circuits with passive and active loads" *IEEE Transactions on Microwave Theory and Techniques*, Volume 42, Issue 8, pages 1514 – 1523, Aug. 1994.

[42] T. Denidni, Q. Rao, and A. Sebak, "T-Shaped microstrip feeding technique for a dual annular slot antenna", *J. Electromag. Waves & Applic.*, Vol. 19, pages 605-614, 2005.

[43] Ansoft Designer, Version 2.1.0, Ansoft Corporation, Pittsburg, PA, Build Dec 1, 2004.

[44] Advanced Design System ver. 2003A.300, Agilent Technologies. Palo Alto, CA. Apr 9, 2003.

[45] D. M. Pozar, "A reciprocity method of analysis for printed slot and slot-coupled microstrip antennas," *IEEE Trans. Antennas Propag.*, vol. AP-34, pages 1439–1446, Nov. 1986.

[46] Ansoft HFSS, Version 9.2.1, Ansoft Corporation, Pittsburg, PA, Build May 7, 2004.

[47] Burden, Richard L., J.D. Faires. *Numerical Analysis: Fifth Edition.* Boston. PWS Publishing Company, 1993.

[48] Luebbers, R. J., F. Hunsberger, "FDTD for Nth-order dispersive media," *IEEE Trans. on Antennas Prop.*, Vol. 40, pages 1297-1301, 1992.

[49] Oppenheim, Alan V., Ronald W. Schafer, John R. Buck. *Discrete-Time Signal Processing, Second Edition.* Prentice Hall, NJ, 1989.

Appendix A1: Approximation of Derivatives

Consider Taylor's Theorem [4] [47],

$$u(x+h) = u(x) + hu'(x) + \frac{1}{2}h^2u''(x) + \frac{1}{6}h^3u'''(x) + \ldots \quad \text{(A1.1)}$$

$$u(x-h) = u(x) - hu'(x) + \frac{1}{2}h^2u''(x) - \frac{1}{6}h^3u'''(x) + \ldots \quad \text{(A1.2)}$$

Adding these (A1.1) to (A1.2) gives the following equation

$$u(x+h) + u(x-h) = 2u(x) + h^2u''(x) + O(h^4) \quad \text{(A1.3)}$$

where $O(h^4)$ is used to describe the error term if subsequent terms are ignored. Notice that the error is controlled by h^4 and higher order terms. If h is considered to be our "delta" term, (A1.3) can be arranged so that the second order derivative u'' can be approximated by

$$u''(x) = \frac{1}{h^2}\{u(x+h) - 2u(x) + u(x-h)\} \quad \text{(A1.4)}$$

Alternatively, Equations (A1.1) and (A1.2) can be subtracted to yield

$$u(x+h) - u(x-h) = 2hu'(x) + O(h^3) \quad \text{(A1.5)}$$

Equation (A1.5) is rearranged to obtain the central difference approximation to the first order derivative,

$$u'(x) \approx \frac{1}{2h}\{u(x+h) - u(x-h)\} \quad \text{(A1.6)}$$

This equation can be added back to (A1.5) to obtain the forward difference approximation to the first order derivative,

$$u'(x) \approx \frac{1}{h}\{u(x+h) - u(x)\} \tag{A1.7}$$

Similarly, the reverse difference equation is given as

$$u'(x) \approx \frac{1}{h}\{u(x) - u(x-h)\} \tag{A1.8}$$

Equations (A1.6) to (A1.8) form the basis of the theory needed for approximating derivatives in FDTD.

Appendix A2: FDTD Method: Formulation

In this appendix we discuss the development of FDTD on a mathematical level. After this, the PML absorbing boundary condition is discussed with an emphasis on the Berenger PML [15], followed by the Convolutional PML (CPML) as introduced by Roden and Gedney [14].

A2.1 Maxwell's Equations

The FDTD method is essentially a discretization of Maxwell's equations. Maxwell's equations can be written in time domain differential form for a source-free region as [1]

Faraday's Law:

$$\frac{\partial \overline{B}}{\partial t} = -\nabla \times \overline{E} - \overline{M} \tag{A2.1}$$

Ampere's Law

$$\frac{\partial \overline{D}}{\partial t} = \nabla \times \overline{H} - \overline{J} \tag{A2.2}$$

For linear, isotropic, non-dispersive media, the constitutive relationships and sources can be written as

$$\begin{aligned} \overline{D} &= \varepsilon \overline{E} \\ \overline{B} &= \mu \overline{H} \\ \overline{J} &= \overline{J}_{source} + \sigma \overline{E} \\ \overline{M} &= \overline{M}_{source} + \sigma \overline{H} \end{aligned} \tag{A2.3}$$

Equations (A2.3) can be substituted into (A2.1) and (A2.2). Faraday's Law and Ampere's Law can then be split into vector components to then become [1]

$$\frac{\partial E_x}{\partial t} = \frac{1}{\mu}\left[\frac{\partial H_z}{\partial y} - \frac{\partial H_y}{\partial z} - \left(M_{source\,x} + \sigma * H_x\right)\right] \tag{A2.4}$$

$$\frac{\partial E_y}{\partial t} = \frac{1}{\mu}\left[\frac{\partial H_x}{\partial z} - \frac{\partial H_z}{\partial x} - \left(M_{source\,y} + \sigma * H_y\right)\right] \tag{A2.5}$$

$$\frac{\partial E_z}{\partial t} = \frac{1}{\mu}\left[\frac{\partial H_y}{\partial x} - \frac{\partial H_x}{\partial y} - \left(M_{source\,z} + \sigma * H_z\right)\right] \tag{A2.6}$$

$$\frac{\partial H_x}{\partial t} = \frac{1}{\mu}\left[\frac{\partial E_y}{\partial z} - \frac{\partial E_z}{\partial y} - \left(J_{source\,x} + \sigma * E_x\right)\right] \tag{A2.7}$$

$$\frac{\partial H_y}{\partial t} = \frac{1}{\mu}\left[\frac{\partial E_z}{\partial x} - \frac{\partial E_x}{\partial z} - \left(J_{source\,y} + \sigma * E_y\right)\right] \tag{A2.8}$$

$$\frac{\partial H_z}{\partial t} = \frac{1}{\mu}\left[\frac{\partial E_x}{\partial y} - \frac{\partial E_y}{\partial x} - \left(J_{source\,z} + \sigma * E_z\right)\right] \tag{A2.9}$$

A2.2 FDTD and the Yee Algorithm

FDTD is based upon a 1st order discretization of the derivatives in equations (A2.4) to (A2.9) and explained in more detail in Appendix A1. To most easily understand the notation, it is best to describe the Yee cell and the standard Yee notation here, where the subscript defines the coordinate of the vector in the Yee space, and the superscript defines the time step.

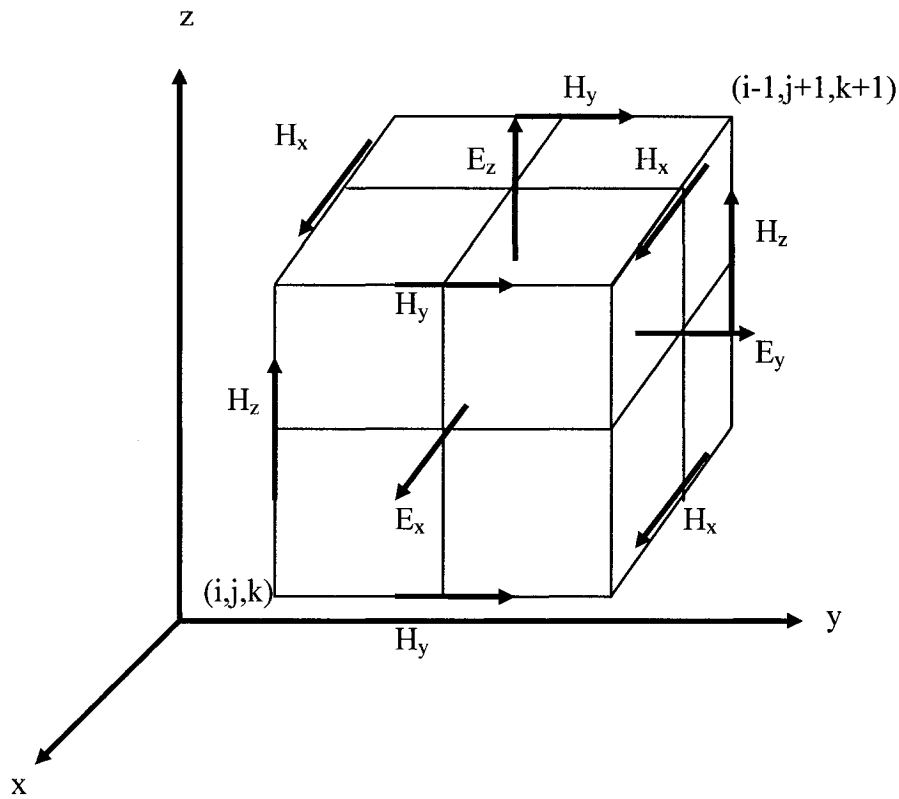

Figure A2.1: The Yee Cell [14]. The lower left corner is marked as coordinate (i,j,k), while the upper right is marked as (i-1, j+1, k+1). The center faces of the cell are at half steps.

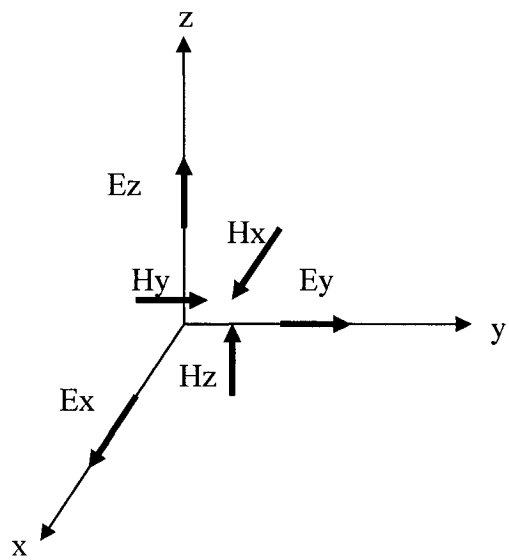

Figure 3.2: Location of vectors for the (i,j,k) cell. [34]

A semi-implicit approximation is used [1] which approximates the future value of the field based on the past value. In Yee notation, this is

$$E_x\Big|^{n}_{i,j+1/2,j+1/2} = \frac{E_x\Big|^{n+1/2}_{i,j+1/2,k+1/2} + E_x\Big|^{n-1/2}_{i,j+1/2,k+1/2}}{2} \tag{A2.10}$$

Using a first order approximation, also in Yee notation, Equation (A2.4) can be written as [1]

$$\frac{E_x\Big|^{n+1/2}_{i,j+1/2,k+1/2} - E_x\Big|^{n-1/2}_{i,j+1/2,k+1/2}}{\Delta t} = \frac{1}{\varepsilon_{i,j+1/2,k+1/2}}\left(\frac{H_z\Big|^{n}_{i,j+1,k+1/2} - H_z\Big|^{n}_{i,j,k+1/2}}{\Delta y} - \frac{H_y\Big|^{n}_{i,j+1/2,k+1} - H_y\Big|^{n}_{i,j+1/2,k}}{\Delta z} - J_{source\,x}\Big|^{n+1/2}_{i,j+1/2,k+1/2} - \sigma_{i,j+1/2,k+1/2} E_x\Big|^{n}_{i,j+1/2,k+1/2}\right) \tag{A2.11}$$

Re-arranging terms and substituting (A2.10) into (A2.11), we obtain our desired explicit time-marching equations, as in [1]. The equations can be simplified as follows, where the Δ terms have not been absorbed into the coefficients,

$$C_a\big|_{i+1/2,j,k} = \left(1 - \frac{\sigma_{i+1/2,j,k}\Delta t}{2\varepsilon_{i+1/2,j,k}}\right) \Bigg/ \left(1 + \frac{\sigma_{i+1/2,j,k}\Delta t}{2\varepsilon_{i+1/2,j,k}}\right) \tag{A2.12}$$

$$C_b\big|_{i+1/2,j,k} = \left(\frac{\Delta t}{\varepsilon_{i+1/2,j,k}}\right) \Bigg/ \left(1 + \frac{\sigma_{i+1/2,j,k}\Delta t}{2\varepsilon_{i+1/2,j,k}}\right) \tag{A2.13}$$

$$D_a\big|_{i,j+1/2,k+1/2} = \left(1 - \frac{\sigma^*_{i,j+1/2,k+1/2}\,\Delta t}{2\mu_{i,j+1/2,k+1/2}}\right) \Bigg/ \left(1 + \frac{\sigma^*_{i,j+1/2,k+1/2}\,\Delta t}{2\mu_{i,j+1/2,k+1/2}}\right) \tag{A2.14}$$

$$D_b\big|_{i,j+1/2,k+1/2} = \left(\frac{\Delta t}{\mu_{i,j+1/2,k+1/2}}\right) \Bigg/ \left(1 + \frac{\sigma^*_{i,j+1/2,k+1/2}\,\Delta t}{2\mu_{i,j+1/2,k+1/2}}\right) \tag{A2.15}$$

The final equations can be written (without source terms),

$$\begin{aligned} E_x\big|^{n+1/2}_{i+1/2,j,k} &= C_{ax}\big|_{i+1/2,j,k}\, Ex\big|^{n-1/2}_{i+1/2,j,k} \\ &+ C_{bx}\big|_{i+1/2,j,k} \left(\frac{H_z\big|^n_{i+1/2,j+1/2,k} - H_z\big|^n_{i+1/2,j-1/2,k}}{\Delta y} - \frac{H_y\big|^n_{i+1/2,j,k+1/2} - H_y\big|^n_{i+1/2,j,k-1/2}}{\Delta z} \right) \end{aligned} \tag{A2.16}$$

$$E_y\Big|_{i,j+1/2,k}^{n+1/2} = C_{ay}\Big|_{i,j+1/2,k} E_y\Big|_{i,j+1/2,k}^{n-1/2} + C_{by}\Big|_{i,j+1/2,k}\left(\begin{array}{l}\dfrac{H_x\Big|_{i,j+1/2,k+1/2}^{n} - H_x\Big|_{i,j+1/2,k-1/2}^{n}}{\Delta z} \\ -\dfrac{H_z\Big|_{i+1/2,j+1/2,k}^{n} - H_z\Big|_{i-1/2,j+1/2,k}^{n}}{\Delta x}\end{array}\right) \tag{A2.17}$$

$$E_z\Big|_{i,j,k+1/2}^{n+1/2} = C_{az}\Big|_{i,j,k+1/2} E_z\Big|_{i,j,k+1/2}^{n-1/2} + C_{bz}\Big|_{i,j,k+1/2}\left(\begin{array}{l}\dfrac{H_y\Big|_{i+1/2,j,k+1/2}^{n} - H_y\Big|_{i-1/2,j,k+1/2}^{n}}{\Delta x} \\ -\dfrac{H_x\Big|_{i,j+1/2,k+1/2}^{n} - H_x\Big|_{i,j-1/2,k+1/2}^{n}}{\Delta y}\end{array}\right) \tag{A2.18}$$

$$H_x\Big|_{i,j+1/2,k+1/2}^{n+1} = D_{ax}\Big|_{i,j+1/2,k+1/2} H_x\Big|_{i,j+1/2,k+1/2}^{n} + D_{bx}\Big|_{i,j+1/2,k+1/2}\left(\begin{array}{l}\dfrac{E_y\Big|_{i,j+1/2,k+1}^{n+1/2} - E_y\Big|_{i,j+1/2,k}^{n+1/2}}{\Delta z} \\ -\dfrac{E_z\Big|_{i,j+1,k+1/2}^{n+1/2} - E_z\Big|_{i,j,k+1/2}^{n+1/2}}{\Delta y}\end{array}\right) \tag{A2.19}$$

$$H_y\Big|_{i+1/2,j,k+1/2}^{n+1} = D_{ay}\Big|_{i+1/2,j,k+1/2} H_y\Big|_{i+1/2,j,k+1/2}^{n} + D_{by}\Big|_{i+1/2,j,k+1/2}\left(\begin{array}{l}\dfrac{E_z\Big|_{i+1,j,k+1/2}^{n+1/2} - E_z\Big|_{i,j,k+1/2}^{n+1/2}}{\Delta x} \\ -\dfrac{E_x\Big|_{i+1/2,j,k+1}^{n+1/2} - E_x\Big|_{i+1/2,j,k}^{n+1/2}}{\Delta z}\end{array}\right) \tag{A2.20}$$

$$H_z\Big|_{i+1/2,j+1/2,k}^{n+1} = D_{az}\Big|_{i+1/2,j+1/2,k} H_z\Big|_{i+1/2,j+1/2,k}^{n}$$
$$+ D_{bz}\Big|_{i+1/2,j+1/2,k}\left(\begin{array}{c}\dfrac{E_x\Big|_{i+1/2,j+1,k}^{n+1/2} - E_x\Big|_{i+1/2,j,k}^{n+1/2}}{\Delta y} \\ -\dfrac{E_y\Big|_{i+1,j+1/2,k}^{n+1/2} - E_y\Big|_{i,j+1/2,k}^{n+1/2}}{\Delta x}\end{array}\right) \qquad \text{(A2.21)}$$

Appendix A3: The Perfectly Matched Layer

Ever since the development of FDTD the concept of the ABC (Absorbing Boundary Condition) has been a consideration for the termination of the solution space [1]. This termination is required because the FDTD method, as described in Appendix A2, makes use of a closed solution space.

Analytical absorbing boundary conditions exist which can provide excellent termination of the solution space, however, the most general termination for arbitrary media in an FDTD solution space is the PML [1].

The first absorbing layers could absorb only normally incident waves at single frequencies, and so had very limited applications. Berenger's PML [13], published in 1994, was able to absorb waves with arbitrary incidence and frequency.

One recent development in the field of PMLs for FDTD is the development of the CPML, or Convolutional PML as first published by Roden and Gedney [1]. This PML is more able to attenuate highly evanescent waves with late-time, low-frequency interactions with the PML.

A3.1 A Matched Boundary Layer for Normal Incidence

The first matched layer was published by Holland and Williams in 1983 [1] [12]. It was able to absorb waves that were normally incident to the layer, but not at an oblique incidence. A brief discussion of its theory follows below.

Consider the reflection coefficient of a plane wave on a lossy medium

$$\Gamma = \frac{\eta_1 - \eta_2}{\eta_1 + \eta_2} \tag{A3.1}$$

where

$$\eta_1 = \sqrt{\frac{\mu_1}{\varepsilon_1}} \tag{A3.2}$$

and

$$\eta_2 = \sqrt{\frac{\mu_2(1+\sigma^*/j\omega\mu_2)}{\varepsilon_2(1+\sigma/j\omega\varepsilon_2)}} \tag{A3.24}$$

where

σ is the electric conductivity and σ^* is the magnetic conductivity.

If the lossy medium and the non-lossy medium have identical permeabilities,

$$\begin{aligned} \varepsilon_1 &= \varepsilon_2 \\ \mu_1 &= \mu_2 \end{aligned} \tag{A3.3}$$

And we further enforce the condition

$$\begin{aligned} 1+\sigma^*/j\omega\mu_2 &= 1+\sigma/j\omega\varepsilon_2 \\ \sigma^* &= \sigma\frac{\mu_2}{\varepsilon_2} = \sigma\frac{\mu_1}{\varepsilon_1} = \sigma\eta_1^{\,2} \end{aligned} \tag{A3.26}$$

Then

$$\eta_1 = \eta_2$$
$$\Gamma = 0 \tag{A3.4}$$

And the boundary between the two medium is reflectionless, even though the second boundary is lossy.

A3.2 Berenger's PML

Berenger's groundbreaking idea was to create a non-physical medium that could absorb waves of normal and oblique incidence [13]. Each of the six field components are split into two, forming the split-field formulation. Hx, for example, is split into Hxy and Hxz. This field splitting allows for splitting of the conductivity components, as well. Instead of a single σ, there is now σ_x, σ_y, σ_z. With the control of separate conductivity components, it is now possible to specify attenuation of waves in *individual* directions. If, for example, $\sigma_x = \sigma_y = 0$, but σ_z is not zero, the PML will absorb waves traveling in only the z-direction, not the x or y direction [1]. A wave traveling in an oblique direction will therefore experience attenuation in the z-direction for a PML in the xy plane, while its tangential components are not attenuated.

The resulting Ampere and Faraday's Laws are shown below:

$$\left(\varepsilon\frac{\partial}{\partial t}+\sigma_y\right)E_{xy} = \frac{\partial}{\partial y}\left(H_{zx}+H_{zy}\right) \tag{A3.5}$$

$$\left(\varepsilon\frac{\partial}{\partial t}+\sigma_z\right)E_{xz} = -\frac{\partial}{\partial z}\left(H_{yx}+H_{yz}\right) \tag{A3.6}$$

$$\left(\varepsilon\frac{\partial}{\partial t}+\sigma_z\right)E_{yz}=\frac{\partial}{\partial z}\left(H_{xy}+H_{xz}\right) \tag{A3.7}$$

$$\left(\varepsilon\frac{\partial}{\partial t}+\sigma_x\right)E_{yx}=-\frac{\partial}{\partial x}\left(H_{zx}+H_{zy}\right) \tag{A3.8}$$

$$\left(\varepsilon\frac{\partial}{\partial t}+\sigma_x\right)E_{zx}=\frac{\partial}{\partial x}\left(H_{yx}+H_{yz}\right) \tag{A3.9}$$

$$\left(\varepsilon\frac{\partial}{\partial t}+\sigma_y\right)E_{zy}=-\frac{\partial}{\partial y}\left(H_{xy}+H_{xz}\right) \tag{A3.10}$$

$$\left(\mu\frac{\partial}{\partial t}+\sigma^*_y\right)H_{xy}=-\frac{\partial}{\partial y}\left(E_{zx}+E_{zy}\right) \tag{A3.11}$$

$$\left(\mu\frac{\partial}{\partial t}+\sigma^*_z\right)H_{xz}=\frac{\partial}{\partial z}\left(E_{yx}+E_{yz}\right) \tag{A3.12}$$

$$\left(\mu\frac{\partial}{\partial t}+\sigma^*_z\right)H_{yz}=-\frac{\partial}{\partial z}\left(E_{xy}+E_{xz}\right) \tag{A3.13}$$

$$\left(\mu\frac{\partial}{\partial t}+\sigma^*_x\right)H_{yx}=\frac{\partial}{\partial x}\left(E_{zx}+E_{zy}\right) \tag{A3.14}$$

$$\left(\mu\frac{\partial}{\partial t}+\sigma^*_x\right)H_{zx}=-\frac{\partial}{\partial x}\left(E_{yx}+E_{yz}\right) \tag{A3.15}$$

$$\left(\mu\frac{\partial}{\partial t}+\sigma^*_y\right)H_{zy}=\frac{\partial}{\partial y}\left(E_{xy}+E_{xz}\right) \tag{A3.16}$$

The reflection coefficient in phasor form for equations (A3.5) to (A3.16) for a plane wave crossing from medium 1 to medium 2 is shown in (A3.17) [1], where the s terms are described in more detail in the next section.

$$\Gamma = \frac{\left(\frac{\beta_{1x}}{\omega\varepsilon_1} - \frac{\beta_{2x}}{\omega\varepsilon_2}\sqrt{\frac{s_x^*}{s_x}} \right)}{\left(\frac{\beta_{1x}}{\omega\varepsilon_1} + \frac{\beta_{2x}}{\omega\varepsilon_2}\sqrt{\frac{s_x^*}{s_x}} \right)}$$

where (A3.17)

$$s_x = \left(1 + \frac{\sigma_x}{j\omega\varepsilon_2}\right)$$

$$s_x^* = \left(1 + \frac{\sigma_x^*}{j\omega\mu_2}\right)$$

For a reflectionless matching condition, the conditions met for normal plane wave incidence must be met for individual components. Assume, for example, that $\varepsilon_1 = \varepsilon_2$, $\mu_1 = \mu_2$, or $k_1 = k_2$ and $\beta_1 = \beta_2$ [1]. Also assume that $\sigma_x / \varepsilon_1 = \sigma_x^* / \mu_1$, which is the same condition as for the normal plane wave, except for the x component. Substituting this into equation (A3.17) above, the reflection coefficient can then be shown to be 0 for a plane wave of any angle of incidence [1].

A3.3 Stretched Coordinate Formulation

Berenger's Split field formulation can be written in a more compact form as introduced by Chew and Weedon [1].

If we define each tensor component as (where in the previous section, $\kappa = 1$),

$$
\begin{aligned}
s_x &= \kappa_x + \frac{\sigma_x}{j\omega\varepsilon} \\
s_y &= \kappa_y + \frac{\sigma_y}{j\omega\varepsilon} \\
s_z &= \kappa_z + \frac{\sigma_z}{j\omega\varepsilon}
\end{aligned}
\tag{A3.18}
$$

then we can write the first two equations (A3.5) and (A3.6) of Berenger's PML in phasor domain as [1]

$$
\begin{aligned}
j\omega\varepsilon s_y \breve{E}_{xy} &= \frac{\partial}{\partial y}\left(\breve{H}_{zx} + \breve{H}_{zy}\right) \\
j\omega\varepsilon s_z \breve{E}_{xz} &= \frac{\partial}{\partial y}\left(\breve{H}_{yx} + \breve{H}_{yz}\right)
\end{aligned}
\tag{A3.19}
$$

If we add the above two equations (A3.19) and use the fact that Ex = Exy + Exz, Hz = Hzx + Hzy, and Hy = Hyx + Hyz then

$$
j\omega\varepsilon \breve{E}_x = \frac{1}{s_y}\frac{\partial}{\partial y}\breve{H}_z - \frac{1}{s_z}\frac{\partial}{\partial z}\breve{H}_y \tag{A3.20}
$$

The other equations for phasors Ey, Ez, Hx, Hy and Hz may be derived similarly as in [1].

Alternatively, to derive the same set of equations, we may define the partial derivatives in the stretched coordinate space,

$$\begin{aligned}\frac{\partial}{\partial \tilde{x}} &= \frac{1}{s_x}\frac{\partial}{\partial x} \\ \frac{\partial}{\partial \tilde{y}} &= \frac{1}{s_y}\frac{\partial}{\partial y} \\ \frac{\partial}{\partial \tilde{z}} &= \frac{1}{s_z}\frac{\partial}{\partial z}\end{aligned} \tag{A3.21}$$

Then the del operator in the mapped space becomes

$$\tilde{\nabla} = \hat{x}\frac{\partial}{\partial \tilde{x}} + \hat{y}\frac{\partial}{\partial \tilde{y}} + \hat{z}\frac{\partial}{\partial \tilde{z}} = \hat{x}\frac{1}{s_x}\frac{\partial}{\partial \tilde{x}} + \hat{y}\frac{1}{s_y}\frac{\partial}{\partial \tilde{y}} + \hat{z}\frac{1}{s_z}\frac{\partial}{\partial \tilde{z}} \tag{A3.22}$$

resulting in the same equation as (A3.20).

Using (A3.20) and the accompanying equations for the other phasors in the time domain, the stretched coordinate formulation of the PML can be expressed as

$$\begin{aligned}\frac{\partial \mathbf{D}}{\partial t} = \hat{x}&\left(\bar{s}_y * \frac{\partial}{\partial y}H_z - \bar{s}_z * \frac{\partial}{\partial z}H_y\right) + \hat{y}\left(\bar{s}_z * \frac{\partial}{\partial z}H_x - \bar{s}_x * \frac{\partial}{\partial x}H_z\right) \\ &+ \hat{z}\left(\bar{s}_x * \frac{\partial}{\partial x}H_y - \bar{s}_y * \frac{\partial}{\partial y}H_x\right)\end{aligned} \tag{A3.23}$$

$$\begin{aligned}-\frac{\partial \mathbf{B}}{\partial t} = \hat{x}&\left(\bar{s}_y * \frac{\partial}{\partial y}E_z - \bar{s}_z * \frac{\partial}{\partial z}E_y\right) + \hat{y}\left(\bar{s}_z * \frac{\partial}{\partial z}E_x - \bar{s}_x * \frac{\partial}{\partial x}E_z\right) \\ &+ \hat{z}\left(\bar{s}_x * \frac{\partial}{\partial x}E_y - \bar{s}_y * \frac{\partial}{\partial y}E_x\right)\end{aligned} \tag{A3.24}$$

Where

$$\bar{s}_w = F^{-1}\left(\frac{1}{s_w}\right) \tag{A3.25}$$

and w is x, y, or z.

A3.4 The Complex Frequency-Shifted Tensor

Berenger found that slowly varying waves or waves at low frequencies may have large reflections from his PML [15]. To reduce late-time, or low-frequency, reflections from the PML, a Complex Frequency-Shifted (CFS) tensor can be used [16] [1]. The non-CFS tensor coefficient used produces a singularity at DC, or f = 0, where the second term in equation (A3.26) below approaches infinity.

$$s_w = \kappa_w + \frac{\sigma_w}{j\omega\varepsilon} \tag{A3.26}$$

If the coefficient is modified as follows (CFS), this problem can be avoided [16] [1],

$$s_w = \kappa_w + \frac{\sigma_w}{a_w + j\omega\varepsilon} \tag{A3.27}$$

When scaling the PML, the value for a_w is largest at the front of the PML (opposite to sigma and K), as discussed in [1]. In (A3.26) and (A3.27) w is coordinate x, y, or z.

A3.5 The Convolutional PML (CPML)

The UPML has been implemented as the default PML in many commercial software packages today [1]. The UPML was introduced by Gedney in 1996 [14]. The CPML is an improvement on the UPML since

1. The classic tensor coefficient used in the UPML or classic Berenger PML can cause late-time / low-frequency reflections, where the CPML uses CFS tensors to overcome this problem. [16]

2. The FDTD update equations are not modified by the PML implementation in this thesis, thus maintaining the simplicity of the Yee algorithm. In fact, the PML is implemented by simply adding values to the E and H fields after they have been computed as per the Yee algorithm. In addition, unlike the UPML, there is no E/D or H/B dependence, which simplifies the modeling of different materials [1].
3. The CPML requires only two variables for the E field in the PML, and two for the H field, requiring a total of only four variables per cell in each PML wall. Other PML implementations such as the UPML require three or more variables per E or H field and require storage within the *entire* computational domain. The CPML is thus very memory efficient, allowing for very fine grid sizes. [16]
4. The CPML is faster than the UPML, since the PML calculations take place only within the PML [1].

The derivation of the CPML follows the PML derivation except with CFS coefficients, where

$$\begin{aligned}\bar{s}_w &= F^{-1}\left(\frac{1}{s_w}\right) \\ &= F^{-1}\left(\frac{1}{\kappa_w + \dfrac{\sigma_w}{a_x + j\omega\varepsilon}}\right) = \frac{\delta(t)}{\kappa_w} - \frac{\sigma_w}{\varepsilon_o \kappa_w^{\,2}} \exp\left[-\left(\frac{\sigma_w}{\varepsilon_o \kappa_w} + \frac{a_w}{\varepsilon_o}\right)t\right] u(t) \\ &= \frac{\delta(t)}{\kappa_w} + \zeta_w(t) \end{aligned} \tag{A3.28}$$

where

$$\zeta_w(t) = -\frac{\sigma_w}{\varepsilon_o \kappa_w^{\,2}} \exp\left[-\left(\frac{\sigma_w}{\varepsilon_o \kappa_w} + \frac{a_w}{\varepsilon_o}\right)t\right] u(t)$$

Using the CFS coefficients and definition from (A3.28), Equations (A3.23) and (A3.24) become

$$\begin{aligned}\frac{\partial \mathbf{D}}{\partial t} = &\hat{x}\left(\frac{1}{\kappa_y}\frac{\partial}{\partial y}H_z - \frac{1}{\kappa_z}\frac{\partial}{\partial z}H_y + \zeta_y * \frac{\partial}{\partial y}H_z - \zeta_z * \frac{\partial}{\partial z}H_y\right) \\ &+ \hat{y}\left(\frac{1}{\kappa_z}\frac{\partial}{\partial z}H_x - \frac{1}{\kappa_x}\frac{\partial}{\partial x}H_z + \zeta_z * \frac{\partial}{\partial z}H_x - \zeta_x * \frac{\partial}{\partial x}H_z\right) \\ &+ \hat{z}\left(\frac{1}{\kappa_x}\frac{\partial}{\partial x}H_y - \frac{1}{\kappa_y}\frac{\partial}{\partial y}H_x + \zeta_x * \frac{\partial}{\partial x}H_y - \zeta_y * \frac{\partial}{\partial y}H_x\right)\end{aligned} \tag{A3.29}$$

$$\begin{aligned}-\frac{\partial \mathbf{B}}{\partial t} = &\hat{x}\left(\frac{1}{\kappa_y}\frac{\partial}{\partial y}E_z - \frac{1}{\kappa_z}\frac{\partial}{\partial z}E_y + \zeta_y * \frac{\partial}{\partial y}E_z - \zeta_z * \frac{\partial}{\partial z}E_y\right) \\ &+ \hat{y}\left(\frac{1}{\kappa_z}\frac{\partial}{\partial z}E_x - \frac{1}{\kappa_x}\frac{\partial}{\partial x}E_z + \zeta_z * \frac{\partial}{\partial z}E_x - \zeta_x * \frac{\partial}{\partial x}E_z\right) \\ &+ \hat{z}\left(\frac{1}{\kappa_x}\frac{\partial}{\partial x}E_y - \frac{1}{\kappa_y}\frac{\partial}{\partial y}E_x + \zeta_x * \frac{\partial}{\partial x}E_y - \zeta_y * \frac{\partial}{\partial y}E_x\right)\end{aligned} \tag{A3.30}$$

The convolutional terms in equations (A3.29) and (A3.30) would take a prohibitive length of time, so a recursive-convolution technique is used to replace these convolutions, as reported by Luebbers and Hunsberger [48] and applied to the CPML by Roden and Gedney [14] as described in the following.

A new variable $Z_w(m)$ is first derived as the discrete impulse response of ζ_w, defined in equation (A3.28)

$$Z_w(m) = \int_{m\Delta t}^{(m+1)\Delta t} \zeta_w(\tau)d\tau = -\frac{\sigma_w}{\varepsilon_o \kappa_w^{\,2}} \int_{m\Delta t}^{(m+1)\Delta t} \exp\left[-\left(\frac{\sigma_w}{\varepsilon_o \kappa_w} + \frac{a_w}{\varepsilon_o}\right)\tau\right] d\tau$$

$$= c_w \exp\left[-\left(\frac{\sigma_w}{\varepsilon_o \kappa_w} + \frac{a_w}{\varepsilon_o}\right) m\Delta t\right] \tag{A3.31}$$

where

$$c_w = \frac{\sigma_w}{\sigma_w \kappa_w + \kappa_w^{\,2} a_w}\left[\exp\left[-\left(\frac{\sigma_w}{\varepsilon_o \kappa_w} + \frac{a_w}{\varepsilon_o}\right)\Delta t\right] - 1\right]$$

A second new variable $\psi_{w,v}$ is introduced to represent the convolution

$$\psi_{w,v}(n) = \zeta_w(t) * \frac{\partial}{\partial w} H_v(t)\Big|_{t=n\Delta t}$$

$$\approx \sum_{m=0}^{n-1} Z_w(m) \frac{\partial}{\partial w} H_v(n-m) \tag{A3.32}$$

This can be simplified as in [1],

$$\psi_{w,v}(n) = b_w \psi_{w,v}(n-1) + c_w \frac{\partial}{\partial w} H_v(n)$$

where (A3.33)

$$b_w = \exp\left[-\left(\frac{\sigma_w}{\varepsilon_o \kappa_w} + \frac{a_w}{\varepsilon_o}\right)\Delta t\right]$$

Equation (A3.33) can be substituted into (A3.29), where w and v are replaced by the appropriate x, y, or z coordinates and approximated with the appropriate finite differences.

The explicit updates are very similar to equations (A2.16) to (A2.21) except for the addition of the ψ CPML components, and the κ factors. The equations are given as

$$E_x\Big|_{i+1/2,j,k}^{n+1/2} = C_{ax}\Big|_{i+1/2,j,k} Ex\Big|_{i+1/2,j,k}^{n-1/2} + C_{bx}\Big|_{i+1/2,j,k}\left(\begin{array}{l}\dfrac{H_z\Big|_{i+1/2,j+1/2,k}^{n} - H_z\Big|_{i+1/2,j-1/2,k}^{n}}{\kappa_{yj}\Delta y} \\ -\dfrac{H_y\Big|_{i+1/2,j,k+1/2}^{n} - H_y\Big|_{i+1/2,j,k-1/2}^{n}}{\kappa_{zk}\Delta z} \\ +\psi_{Ex,y}\Big|_{i+1/2,j,k}^{n} - \psi_{Ex,z}\Big|_{i+1/2,j,k}^{n}\end{array}\right) \tag{A3.34}$$

$$E_y\Big|_{i,j+1/2,k}^{n+1/2} = C_{ay}\Big|_{i,j+1/2,k} E_y\Big|_{i,j+1/2,k}^{n-1/2} + C_{by}\Big|_{i,j+1/2,k}\left(\begin{array}{l}\dfrac{H_x\Big|_{i,j+1/2,k+1/2}^{n} - H_x\Big|_{i,j+1/2,k-1/2}^{n}}{\kappa_{zk}\Delta z} \\ -\dfrac{H_z\Big|_{i+1/2,j+1/2,k}^{n} - H_z\Big|_{i-1/2,j+1/2,k}^{n}}{\kappa_{xi}\Delta x} \\ +\psi_{Ey,z}\Big|_{i,j+1/2,k}^{n} - \psi_{Ey,x}\Big|_{i,j+1/2,k}^{n}\end{array}\right) \tag{A3.35}$$

$$E_z\Big|_{i,j,k+1/2}^{n+1/2} = C_{az}\Big|_{i,j,k+1/2} E_z\Big|_{i,j,k+1/2}^{n-1/2} + C_{bz}\Big|_{i,j,k+1/2}\left(\begin{array}{l}\dfrac{H_y\Big|_{i+1/2,j,k+1/2}^{n} - H_y\Big|_{i-1/2,j,k+1/2}^{n}}{\kappa_{xi}\Delta x} \\ -\dfrac{H_x\Big|_{i,j+1/2,k+1/2}^{n} - H_x\Big|_{i,j-1/2,k+1/2}^{n}}{\kappa_{yj}\Delta y} \\ +\psi_{Ez,x}\Big|_{i,j,k+1/2}^{n} - \psi_{Ez,y}\Big|_{i,j,k+1/2}^{n}\end{array}\right) \tag{A3.36}$$

$$H_x\Big|_{i,j+1/2,k+1/2}^{n+1} = D_{ax}\Big|_{i,j+1/2,k+1/2} H_x\Big|_{i,j+1/2,k+1/2}^{n}$$
$$+ D_{bx}\Big|_{i,j+1/2,k+1/2} \left(\begin{array}{l} \dfrac{E_y\Big|_{i,j+1/2,k+1}^{n+1/2} - E_y\Big|_{i,j+1/2,k}^{n+1/2}}{\kappa_{z\,k+1/2}\Delta z} \\ -\dfrac{E_z\Big|_{i,j+1,k+1/2}^{n+1/2} - E_z\Big|_{i,j,k+1/2}^{n+1/2}}{\kappa_{y\,j+1/2}\Delta y} \\ +\psi_{Hx,z}\Big|_{i,j+1/2,k+1/2}^{n+1/2} - \psi_{Hz,y}\Big|_{i,j+1/2,k+1/2}^{n+1/2} \end{array} \right) \quad \text{(A3.37)}$$

$$H_y\Big|_{i+1/2,j,k+1/2}^{n+1} = D_{ay}\Big|_{i+1/2,j,k+1/2} H_y\Big|_{i+1/2,j,k+1/2}^{n}$$
$$+ D_{by}\Big|_{i+1/2,j,k+1/2} \left(\begin{array}{l} \dfrac{E_z\Big|_{i+1,j,k+1/2}^{n+1/2} - E_z\Big|_{i,j,k+1/2}^{n+1/2}}{\kappa_{x\,i+1/2}\Delta x} \\ -\dfrac{E_x\Big|_{i+1/2,j,k+1}^{n+1/2} - E_x\Big|_{i+1/2,j,k}^{n+1/2}}{\kappa_{z\,k+1/2}\Delta z} \\ +\psi_{Hy,x}\Big|_{i+1/2,j,k+1/2}^{n+1/2} - \psi_{Hy,z}\Big|_{i+1/2,j,k+1/2}^{n+1/2} \end{array} \right) \quad \text{(A3.38)}$$

$$H_z\Big|_{i+1/2,j+1/2,k}^{n+1} = D_{az}\Big|_{i+1/2,j+1/2,k} H_z\Big|_{i+1/2,j+1/2,k}^{n}$$
$$+ D_{bz}\Big|_{i+1/2,j+1/2,k} \left(\begin{array}{l} \dfrac{E_x\Big|_{i+1/2,j+1,k}^{n+1/2} - E_x\Big|_{i+1/2,j,k}^{n+1/2}}{\kappa_{y\,j+1/2}\Delta y} \\ -\dfrac{E_y\Big|_{i+1,j+1/2,k}^{n+1/2} - E_y\Big|_{i,j+1/2,k}^{n+1/2}}{\kappa_{x\,i+1/2}\Delta x} \\ +\psi_{Hz,y}\Big|_{i+1/2,j+1/2,k}^{n+1/2} - \psi_{Hz,x}\Big|_{i+1/2,j+1/2,k}^{n+1/2} \end{array} \right) \quad \text{(A3.39)}$$

The Coefficients Ca, Cb, Da, Db are given in equation (A2.12) to (A2.15).

The CPML coefficients ψ are approximated in a similar way and can be calculated in a time-marching manner as follows in Equations (A3.40) to (A3.51).

For Ex,

$$\psi_{Ex,y}\Big|_{i+1/2,j,k}^{n} = b_{yj}\psi_{Ex,y}\Big|_{i+1/2,j,k}^{n-1} + c_{yj}\left(\frac{H_z\Big|_{i+1/2,j+1/2,k}^{n} - H_z\Big|_{i+1/2,j-1/2,k}^{n}}{\Delta y}\right) \tag{A3.40}$$

$$\psi_{Ex,z}\Big|_{i+1/2,j,k}^{n} = b_{zk}\psi_{Ex,z}\Big|_{i+1/2,j,k}^{n-1} + c_{zk}\left(\frac{H_y\Big|_{i+1/2,j,k+1/2}^{n} - H_y\Big|_{i+1/2,j,k-1/2}^{n}}{\Delta z}\right) \tag{A3.41}$$

For Ey,

$$\psi_{Ey,z}\Big|_{i,j+1/2,k}^{n} = b_{zk}\psi_{Ey,z}\Big|_{i,j+1/2,k}^{n-1} + c_{zk}\left(\frac{H_x\Big|_{i,j+1/2,k+1/2}^{n} - H_x\Big|_{i,j+1/2,k-1/2}^{n}}{\Delta z}\right) \tag{A3.42}$$

$$\psi_{Ey,x}\Big|_{i,j+1/2,k}^{n} = b_{xi}\psi_{Ey,x}\Big|_{i,j+1/2,k}^{n-1} + c_{xi}\left(\frac{H_z\Big|_{i+1/2,j+1/2,k}^{n} - H_z\Big|_{i-1/2,j+1/2,k}^{n}}{\Delta x}\right) \tag{A3.43}$$

For Ez,

$$\psi_{Ez,x}\Big|_{i,j,k+1/2}^{n} = b_{xi}\psi_{Ez,x}\Big|_{i,j,k+1/2}^{n-1} + c_{xi}\left(\frac{H_y\Big|_{i+1/2,j,k+1/2}^{n} - H_y\Big|_{i-1/2,j,k+1/2}^{n}}{\Delta x}\right) \tag{A3.44}$$

$$\psi_{Ez,y}\Big|_{i,j,k+1/2}^{n} = b_{yj}\psi_{Ez,y}\Big|_{i,j,k+1/2}^{n-1} + c_{yj}\left(\frac{H_x\Big|_{i,j+1/2,k+1/2}^{n} - H_x\Big|_{i,j-1/2,k+1/2}^{n}}{\Delta y}\right) \tag{A3.45}$$

For Hx,

$$\psi_{Hx,y}\Big|_{i,j+1/2,k+1/2}^{n+1/2} = b_{yj+1/2}\psi_{Hx,y}\Big|_{i,j+1/2,k+1/2}^{n-1/2} + c_{yj+1/2}\left(\frac{E_z\Big|_{i,j+1,k+1/2}^{n+1/2} - E_z\Big|_{i,j,k+1/2}^{n+1/2}}{\Delta y}\right) \tag{A3.46}$$

$$\psi_{Hx,z}\Big|_{i,j+1/2,k+1/2}^{n+1/2} = b_{z\,k+1/2}\,\psi_{Hx,z}\Big|_{i,j+1/2,k+1/2}^{n-1/2} + c_{z\,k+1/2}\left(\frac{E_z\Big|_{i,j+1/2,k+1}^{n+1/2} - E_z\Big|_{i,j+1/2,k}^{n+1/2}}{\Delta z}\right) \tag{A3.47}$$

For Hy,

$$\psi_{Hy,x}\Big|_{i+1/2,j,k+1/2}^{n+1/2} = b_{x\,i+1/2}\,\psi_{Hy,x}\Big|_{i+1/2,j,k+1/2}^{n-1/2} + c_{x\,i+1/2}\left(\frac{E_z\Big|_{i+1,j,k+1/2}^{n+1/2} - E_z\Big|_{i,j,k+1/2}^{n+1/2}}{\Delta x}\right) \tag{A3.48}$$

$$\psi_{Hy,z}\Big|_{i+1/2,j,k+1/2}^{n+1/2} = b_{z\,k+1/2}\,\psi_{Hy,z}\Big|_{i+1/2,j,k+1/2}^{n-1/2} + c_{z\,k+1/2}\left(\frac{E_x\Big|_{i+1/2,j,k+1}^{n+1/2} - E_x\Big|_{i+1/2,j,k}^{n+1/2}}{\Delta z}\right) \tag{A3.49}$$

For Hz,

$$\psi_{Hz,y}\Big|_{i+1/2,j+1/2,k}^{n+1/2} = b_{y\,j+1/2}\,\psi_{Hz,y}\Big|_{i+1/2,j+1/2,k}^{n-1/2} + c_{y\,j+1/2}\left(\frac{E_x\Big|_{i+1/2,j+1,k}^{n+1/2} - E_x\Big|_{i+1/2,j,k}^{n+1/2}}{\Delta y}\right) \tag{A3.50}$$

$$\psi_{Hz,x}\Big|_{i+1/2,j+1/2,k}^{n+1/2} = b_{x\,i+1/2}\,\psi_{Hz,x}\Big|_{i+1/2,j+1/2,k}^{n-1/2} + c_{x\,i+1/2}\left(\frac{E_y\Big|_{i+1,j+1/2,k}^{n+1/2} - E_y\Big|_{i,j+1/2,k}^{n+1/2}}{\Delta x}\right) \tag{A3.51}$$

where b, c are defined in equations (A3.33) and (A3.31)

This completes the formulation for the CPML. Note that the coefficients ψ need only be calculated within the PML, not within the main solution space. The parameter κ is equal to 1 everywhere except within the PML.

Appendix A4: The Discrete Fourier Transform

The FDTD method is by nature a time domain method. The results for reflection coefficient are usually required in the frequency domain, therefore a time to frequency domain conversion is necessary. The Discrete Fourier Transform (DFT) is used for this purpose, as documented in the text by Oppenheim and Schafer [49].

Consider the discrete sequence x[n], where x[n] is equal to 0 outside the range

$$0 \leq n \leq N\text{-}1 \tag{A4.1}$$

The Analysis equation is given as

$$X[k] = \sum_{n=0}^{N-1} x[n] W_N^{kn}$$
$$\textit{where} \tag{A4.2}$$
$$W_N^{kn} = e^{-j(2\pi/N)}$$

In equation (A4.2), the integer values for k represent discrete frequencies in the frequency domain. In FDTD, the stability limit, as discussed in Appendix A2, requires that the time step is very small. The corresponding values for k then does not require that we calculate k for N samples, but the number may be significantly less.

In fact, the radian frequency corresponding to the continuous frequency is 2π, which corresponds to the k=N frequency point. This radian frequency corresponds to a continuous frequency of $1 / \Delta t$, where Δt is the time step used in the simulation. Consider a typical simulation where the time step is 10×10^{-13} s. The corresponding continuous time frequency is 1000 GHz! Obviously, we do not need the frequency response at this frequency. If we compute values up to 10 GHz, we only to compute $1 / 100^{th}$ of the total

discrete Fourier transform, which can be performed in a matter of seconds on a modern computer.

Because of this advantage, another problem exists. Suppose we are interested in the same 10 GHz as discussed above and the FDTD simulation creates 1000 points in the time domain. Here, N = 1000, and there are 1000 corresponding values for X[k]. We need only the first 1 / 100^{th} of the 1000 points, however, so this leaves us with only 10 points between 0 and 10 GHz, which makes for a very ragged graph.

Consider now equation (A4.1). Since we assume values are zero outside the known data points, we may "pad" zeros at the end of our data set so that the corresponding value of N is sufficiently high for a good resolution in the frequency band of interest. This is referred to as "zero-padding" in digital processing terminology.

It is also important to note that we are assuming that the values are zero outside the known data. If the simulation is truncated early, the effect on the DFT is the same as applying a rectangular window in the time domain, which results in ripples in the frequency response in the frequency domain. To circumvent this issue, there have been approximation methods that have been developed, such as the Prony algorithm, the Pade approximation, or other methods [1].